FINITE ELEMENT SIMULATION OF CHIP SEGMENTATION IN MACHINING A Ti 6Al-4V ALLOY

By

KAREEM SYED

Bachelor of Engineering

Osmania University

Hyderabad, India

June, 2001

Submitted to the Faculty of the
Graduate College of the
Oklahoma State University
in partial fulfillment of
the requirements for
the Degree of
MASTER OF SCIENCE
December, 2004

FINITE ELEMENT SIMULATION OF CHIP
SEGMENTATION IN MACHINING A
Ti 6Al-4V ALLOY

Thesis approved:

Dr. Ranga Komanduri

Thesis Adviser

Dr. Hong Bing Lu

Dr. Samit Roy

Dr. Gordon Emslie

Dean of the Graduate College

ACKNOWLEDGEMENT

I wish to express my sincere thanks to my advisor, Dr.Ranga Komanduri, for his intelligent supervision, constructive guidance, financial support, inspiration and motivation. His wise advices made it possible for me to quickly grow not only technically but also in all aspects during the course of my M.S study. I truly appreciate the encouragement and technical guidance from my committee members: Dr. Samit Roy and Dr. Hongbing Lu. I would also like to thank Dr. Bo Wang for his guidance in deriving the equations for Recht's catastrophic shear failure criterion.

This project has been funded by a grant from the division of Design, Manufacturing and Industrial Innovation (DMII) of the National Science Foundation (NSF). I would like to thank Dr. George Hazelrigg for his interest and support of this work.

I would like to thank Chief Technical Officer Dr. Troy Marusich of Third Wave Systems, Inc. and Support Engineers Mr. Christopher Brand and Mr. Deepak Agarwal for their technical support in using AdvantEdge™ software.

I wish to express my sincere gratitude to Mr. Dhananjay Joshi and Mr. Parag Konde for their contribution in discussing, deriving and implementing the equations of Recht's catastrophic shear failure criterion into the user subroutine code (UMAT). I would also like to extend my gratitude to all other members of our research group for their support and friendship.

I would like to thank the Department of Mechanical and Aerospace Engineering for providing me with the opportunity to pursue M.S at Oklahoma State University.

I am ever thankful to my parents who were always a constant source of my inspiration and encouragement at all times. Finally, I would like to extend my gratitude to my brother and sisters for their inspiration and love.

TABLE OF CONTENTS

Chapter Page

1. Introduction……...…….....1

1.1 State Of Art: Finite Element Simulation of the Cutting Process……...1
1.2 Historical Developments…….....3
1.3 Principles of Metal Cutting……....5
1.4 Principles of Finite Element Modeling……..6
1.5 Metallurgical Aspects of Titanium alloys……..7
1.6 Machinability aspects of Ti 6Al-4V…….10
1.7 Mechanism of Shear-Localized Chip Formation in Ti 6Al-4V……..11
1.8 Thesis Outline……...13

2. Literature Review……..…….....16

2.1 Numerical Study of Shear-Localized Chip Formation……..16
2.2 Shear-Localized Chip Formation in Ti 6Al-4V: Experiments...25
2.3 Shear-Localized Chip Formation in Ti 6Al-4V-FEM Simulations…….36

3. Finite Element Formulation of Metal Cutting 47

3.1 Introduction……..…….....47
3.2 Finite Element Formulation ……..48
3.3 Friction formulation along tool-chip interface …… 57
3.4 Formulation of Contact Conditions ……..58
3.5 Adaptive remeshing ……..59
3.6 Chip formation……...61

4. Problem Statement…….....63

5. Shear-Localized Chip Formation in Ti 6Al-4V machining……..65

5.1 Shear-Localized Chip in Ti 6Al-4V ……...65
5.2 Mechanism of Shear-Localized Chip formation.…… ……66
5.3 Criterion for Thermo Plastic Shear Instability……68

5.4 Metallurgical Aspects of Shear-Localized Chip Formation…..70

6. FEM Simulation of Chip Segmentation in Ti 6Al-4V ……..72

6.1 Introduction……..……....72
6.2 Material Constitutive Model ……...73
6.3 Formulation of Recht's Catastrophic Shear Failure Criterion 75
6.4 Stress Update Algorithm …….80

7. Results and Discussions……..…….....84

7.1 Process Model and Material Properties……... 84
7.2 Simulation Approach and Cutting Conditions……..88
7.3 Observations of Chip Formation Process…….90
7.4 Temperature and Equivalent Plastic Strain distribution in the chip……94
7.5 Effects of Cutting Speed and Feed rate……....97
7.6 Effects of Rake angle……..111
7.7 Effects of Coefficient of friction…….116
7.8 Validation of Simulation Results…….119
7.9 Discussion……...126

8. Conclusions and Future Work ……..128

8.1 Conclusions……..128
8.2 Future Work..……...131

References.....……...133

LIST OF TABLES

Table No. Page No.

7.1 Physical properties of Ti 6Al-4V…..……..86

7.2 Johnson-Cook material properties for Ti 6Al-4V……...87

7.3 Cutting conditions used for FEM simulations……....89

7.4 Tool dimensions used in FEM simulations……....90

7.5 Adaptive mesh options input to the FEM software……90

7.6 Finite element simulation results and experimental data of cutting and thrust force with percent deviation……..120

7.7 Finite element results and experimental data for cutting force with percent deviation……122

LIST OF FIGURES

Figure No. Page

1.1 Orthogonal metal cutting model …….....6

1.2 Microstructure of Ti 6Al-4V alloy showing primary α-phase and transformed β-grains……....9

2.1 Stress-strain diagram for a combination of strain hardening, thermal softening and failure softening……. 22

2.2 Adiabatic shear-localized chip in a Ti 6Al-4V alloy, obtained by orthogonal cutting at the velocity 1.2 m/s……... 28

2.3 Chip morphology as a function of cutting speed and feed in the orthogonal cutting of a Ti 6Al-4V alloy…….. 29

2.4 Shear-Localized chip formed in machining a Ti 6Al-4V alloy at cutting speeds of 60 and 120 m/min using feed rate of 0.127 mm/rev……..... 31

2.5 Roughness of workpiece material (Ti 6Al-4V) as a function of cutting length at different cutting speeds…….. 32

2.6 Voids and cracks in an adiabatic shear band of a Ti 6Al-4V alloy specimen deformed at 700°C and 2000 s^{-1} strain rate……...33

2.7 Temperature dependence of flow stress in a Ti 6Al-4V alloy at very low strain rates of 10^{-3} s^{-1} ……34

2.8 Pseudo-temperature variation with drill depth showing a linear increase ……...35

2.9 Serrated chips obtained in machining a Ti 6Al-4V alloy at cutting speeds (a) 80 m/min and (b) 140 m/min…….. 36

2.10 Chip formation process showing shear localization in finite element simulation of a Ti 6Al-4V alloy at cutting speed of 5 m/s and feed 0.3 mm using -8° rake angle tool……... 37

2.11 Tool-workpiece mesh system used in finite element simulation of orthogonal metal cutting a Ti 6Al-4V alloy…….. 39
2.12 Serrated chip formation with cutting length in finite element simulation of machining a Ti 6Al-4V alloy at cutting speed 30 m/min, feed 0.25 mm and 20° rake angle……... 39
2.13 Serrated chip formed in finite element simulation of orthogonal metal cutting of a Ti 6Al-4V alloy at cutting speed 30 m/min, feed 0.25 mm and 20° rake angle…….. 40
2.14 Initial geometry and workpiece-tool mesh used in finite element simulation of orthogonal metal cutting of a Ti 6Al-4V alloy……41
2.15 Segmented chip formation process in finite element simulation of orthogonal metal cutting of a Ti 6Al-4V alloy at 10 m/s cutting speed and 0.5 mm feed using a -3° rake angle tool ……. 42
2.16 Segmented chip formation process in finite element simulation of orthogonal metal cutting of a Ti 6Al-4V alloy at 50 m/s cutting speed and 0.04 mm cutting depth using a 10° rake angle tool …….43
2.17 Equivalent plastic strain distribution in serrated chip simulated at cutting speeds of 1.2, 120 and 600 m/min in a Ti 6Al-4V alloy……...45
3.1 Contacting surfaces in a mesh showing (a) predictor configuration and (b) kinematically compatible configuration…….. 59
3.2 Six-nodes and three quadrature points shown in a typical six-noded triangular element used in finite element mesh of workpiece and tool……60
3.3 Element shape in a finite element mesh (a) before adaptive remeshing and (b) after adaptive remeshing……..60
5.1 Description of shear-localized chip formed due to adiabatic shear localization……...67
5.2 X-ray diffraction spectra for chip and uncut material in a Ti6Al4V alloy….. 71
6.1 Model used for determination of temperature gradient with strain

in catastrophic shear zone…….. 77

6.2 Variation of Recht's criterion value (R) with temperature for Ti 6Al-4V alloy at different strain rates and strain of 3…….....79

6.3 Variation of Recht's criterion value (R) with temperature for Ti 6Al-4V alloy at different strain rates and strain of 4…….....80

7.1 Workpiece-tool system used for FEM simulations showing initial mesh….. 86

7.2 True stress-strain curves of Ti 6Al-4V alloy based on Johnson-Cook material model in the temperature range of 20^0 to 1600^0 C at high strain rate of 1x 10^4 s^{-1}…….. 87

7.3 The variation of True stress as a function of temperature for Ti 6Al-4V in the different strain range of 0.005 to 4.0 at high strain rate of 1x 10^4 s^{-1} 88

7.4 Various stages of shear-localized chip formation in machining simulation of Ti 6Al-4V conducted at 30 m/min cutting speed and 0.5 mm depth of cut for -15° rake angle showing equivalent plastic strain localization in narrow shear bands……..93

7.5 Temperature distribution in shear-localized chip formation obtained from FEM simulation of machining Ti 6Al-4V at 30 m/min cutting speed and 0.5 depth of cut for -15° rake angle …….……...95

7.6 Equivalent plastic strain distribution in the shear-localized chip formation from FEM simulation of machining Ti 6Al-4V at a cutting speed of 30m/min and a depth of cut of 0.5 mm for a -15° rake angle…….96

7.7 Temperature and equivalent plastic strain contour plots in shear-localized chips formed in machining simulations of Ti 6Al-4V for a depth of cut of 0.25 mm at different cutting speeds varying from 10 to100 m/min using 0° rake angle tool…….100

7.8 Temperature and equivalent plastic strain contour plots in shear-localized chips formed in machining simulations of Ti 6Al-4V for a depth of cut of 0.5 mm at different cutting speeds varying

from 10 to100 m/min using 0° rake angle tool……104

7.9 Effect of cutting speed on (a) the shear zone temperature and (b) the rake face temperature for FEM simulations of Ti 6Al-4V at cutting speeds from 10 to 100 m/min for two different depths of cut of 0.25 and 0.5 mm……...104

7.10 Effect of cutting speed on (a) equivalent plastic strain and (b) plastic strain rate for FEM simulations of Ti 6Al-4V at cutting speeds varying from 10 to 100 m/min for two different depths of cut of 0.25 and 0.5mm……..…..105

7.11 Cutting and thrust force plots with time for finite element simulations of Ti 6Al-4V for a cutting speed of 30 m/min and depth of cut of 0.5 mm using different rake angles of -15°, 0°, 15°, 30° and 45°…….107

7.12 Temperature and equivalent plastic strain contour plots in the chip formed in machining simulation of Ti 6Al-4V for a depth of cut of 0.25 mm and a cutting speed of 5 m/min using a 0° rake angle tool……..108

7.13 Temperature and equivalent plastic strain contour plots in the chip formed in machining simulation of Ti 6Al-4V for a depth of cut of 0.5 mm and a cutting speed of 5 m/min using a 0° rake angle tool……109

7.14 Effect of cutting speed on (a) average cutting force and (b) average thrust force for FEM simulations of Ti 6Al-4V at cutting speeds from 10 to 100 m/min for two different depths of cut of 0.25 and 0.5 mm, respectively……110

7.15 Effect of cutting speed on (a) average power consumption and (b) number of segments for FEM simulations of Ti 6Al-4V at cutting speeds from 10 to 100 m/min for two different depths of cut of 0.25 and 0.5 mm, respectively…….111

7.16 Temperature and equivalent plastic strain contour plots in chip

segmentation in machining simulations of Ti 6Al-4V for a depth of cut of 0.5 mm at a cutting speed of 30 m/min using different rake angles of -15°, 0°, 15°, 30° and 45……...114

7.17 Effect of rake angle on (a) shear zone and rake face temperatures (b) equivalent plastic strain in the shear zone (c) plastic strain rate and (d) cutting forces for FEM simulations of Ti 6Al-4V at cutting speed 30 m/min and depth of cut of 0.5 mm……. 115

7.18 Temperature and equivalent plastic strain contour plots in chip segmentation in machining simulations of Ti 6Al-4V for a depth of cut of 0.5 mm and cutting speed of 30 m/min using different friction coefficients (0.3, 0.5, 0.7, 0.9)……....118

7.19 Effect of friction coefficient on (a) shear zone temperature and (b) rake face temperature for FEM simulations of Ti 6Al-4V at a cutting speed of 30 m/min and depth of cut of 0.5 mm……118

7.20 Effect of friction coefficient on (a) equivalent plastic strain and (b) average cutting forces for FEM simulations of Ti6Al4V at a cutting speed 30 m/min and a depth of cut of 0.5 mm……..118

7.21 FEM and experimental results of cutting and thrust force compared for feed rates 0.02, 0.05, 0.075, 0.1mm/rev……. 121

7.22 Results of cutting forces obtained from FEM simulations compared with experimental data for feed rates 0.127 and 0.35mm/rev…...122

7.23 Results of chip comparison from FEM simulations and experimental data for 180m/min cutting speed and feed rates of 0.04, 0.06, 0.08, and 0.1mm/rev……..124

7.24 Results of chip morphology from FEM simulation conducted at 1.2 m/s and 0.5mm/rev feed rate compared with that of experimental data.125

CHAPTER 1

INTRODUCTION

1.1 State of Art: Finite Element Simulation of the Cutting Process

Improvements in manufacturing technologies require better modeling and simulation of metal cutting processes. Theoretical and experimental investigations of metal cutting have been extensively carried out using various techniques. On the other hand, complicated mechanisms usually associated in metal cutting, such as interfacial friction, heat generated due to friction, large strains in the cutting region and high strain rates, have somewhat limited the theoretical modeling of chip formation. So, many researches are focusing on computer modeling and simulation of metal cutting process to solve many complicated problems arising in the development of new technologies. One of the state-of-art efforts in manufacturing engineering is the finite element simulation of the metal cutting process. These simulations would greatly enhance our understanding of the metal cutting process and in reducing the number of trial and error experiments, which is used traditionally for tool design, process selection, machinability evaluation, chip formation and chip breakage investigations. According to a comprehensive survey conducted by the CIRP Working Group on Modeling of Machining Operations during 1996-1997 [1], among the 55 major research groups active in modeling, 43% were active in empirical modeling, 32% in analytical modeling, and 18% in numerical modeling in

which finite element modeling techniques are used as the dominant tool. More attention to the finite element method has been paid in the past decade in respect to its capability of numerical modeling of different types of metal cutting problems. Advantage of finite element method is the entire process can be simulated using a computer.

Compared to empirical and analytical methods, finite element methods used in the analysis of chip formation have advantages in several respects, namely,

(1) Material properties can be handled as a function of strain, strain rate, and temperature.

(2) Interaction between the chip and the tool can be modeled as sticking and sliding.

(3) Non-linear geometric boundaries, such as the free surface of the chip can be represented and used.

(4) In addition to the global variables such as, the cutting force, thrust force and chip geometry, local variables, such as stresses, temperature distributions, etc., can also be obtained.

Finite element method has been used to simulate machining operations since the early 1970s [45]. With the development of faster processors and larger memory, model limitations and computational difficulty have been overcome to a large extent. In addition, more commercial FE codes are being developed for cutting simulations, including ABAQUS , AdvantEdge , DEFORM 2D , LS DYNA , FORGE 2D , MARC , FLUENT and ALGOR . Significant progress has been made in this field such as:

(1) Lagrangian approach is used to simulate the cutting process including incipient chip formation.

(2) Segmented chip formation is modeled to simulate high-speed machining.

(3) 3D simulation is performed to analyze oblique cutting.

(4) A diversity of cutting tools and workmaterials is used in the simulation of cutting process.

1.2 Historical Developments

The earliest finite element chip formation studies simulated the loading of tool against a pre-formed chip avoiding the problems of modeling large flows [46]. Small strain elastic-plastic analysis demonstrated the development of plastic yielding along the primary shear plane as the tool was displaced against the chip. This work had a number of limitations, making it only of historical interest. The limitations of this initial work were removed by Shirakashi and Usui [3], who developed an iterative way of changing the shape of the pre-formed chip until the generated plastic flow was consistent with the assumed shape. They also included realistic chip/tool friction conditions and material flow stress variations with strain, strain rate and temperature measured from high strain rate Hopkinson bar tests. The procedure of loading a tool against an already formed chip greatly reduced computing capacity requirements. The justification of the method was that it gave good agreement with experiments but it did not follow the actual path by which a chip should be formed.

Rigid–plastic modeling however, does not require the actual loading path to be followed. Iwata *et al.* [4] developed steady state rigid-plastic modeling (within a eulerian

framework) adjusting an initially assumed flow field to bring it into agreement with the computed field. They included friction, work hardening, and a chip fracture criterion. Experiments at low cutting speeds supported their predictions. The mid-1980s saw the first non-steady chip formation analyses, following the development of a chip from first contact of a cutting edge with the workpiece as in machining. Updated Lagrangian elastic-plastic analysis was used, and different chip/ work separation criteria at the cutting edge were developed. Strenkowski and Carol [5] used a strain-based separation criterion. At that time, neither a realistic friction model nor coupling of elastic-plastic to thermal analysis was included.

The 1990s have seen the development of non-steady state analysis, from transient to discontinuous chip formation, the first three-dimensional analyses, and the introduction of adaptive meshing techniques particularly to cope with the flow around the cutting edge of a tool. A simple form of remeshing at the cutting edge, instead of the geometrical crack, was introduced to accommodate the separation of chip from the work. Both rigid-plastic and elastic-plastic adaptive remeshing softwares have been developed and are being applied for chip formation simulations [14, 15]. Marusich and Oritz [14] developed a two-dimensional finite element code for the simulation of orthogonal cutting that includes sophisticated adaptive remeshing, thermal effects, a criterion for brittle fracture and tool stiffness. They seem to be more effective than Arbitrary Lagrangian-Eulerian (ALE) methods in which the mesh is neither fixed in space nor in the workpiece. Thus, the 1970s to the 1990s has seen the development and testing of finite element techniques for chip formation processes and during this period, many researchers have concentrated

more on the development of the new methods in the finite element simulations of metal cutting [2].

1.3 Principles of Metal Cutting

Metal cutting is classified as the secondary process by which material is removed to transform a raw material to a part with certain shape, size, dimensional tolerance and surface finish. The theory of machining is concerned with the various features of the cutting process including the forces, strain and strain rates, temperatures, and wear of cutting tools. All metal cutting operations, such as turning, drilling, boring, milling, grinding, reaming and other metal removal processes produce chips in a similar fashion. Therefore, analysis of chip formation can give better understanding to the mechanics of machining processes. Metal cutting involves concentrated shear along a rather distinct shear plane. As metal approaches the shear plane, it does not deform until the shear plane is reached. It then undergoes a substantial amount of simple shear as it crosses the thin shear zone. There is essentially no further plastic flow as the chip proceeds up the face of the tool. The tool is a single point tool that is characterized by the rake angle α and the clearance angle θ as shown in Fig. 1.1. When the rake face of the tool is in the clockwise position from the workpiece then the rake angle is considered positive and if it is counter clockwise then it is considered negative [6]. A small clearance angle is generally used to keep the tool from damaging the finished surface of the workpiece. The rake face of the tool is the surface over which the chip flows and has a contact length l_c, which is the chip-tool contact interaction. The prescribed velocity V, known as the cutting speed is in the feed direction.

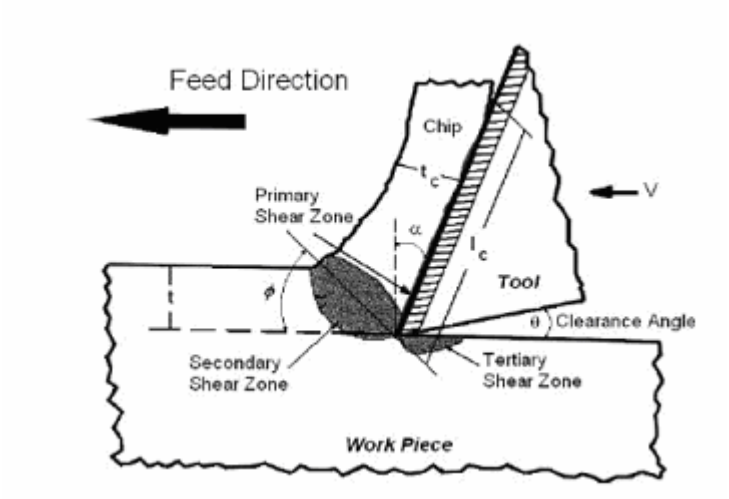

Fig. 1.1 Orthogonal metal cutting model [6]

The localized straining in the workpiece enforced by the tool causes plastic deformation of the undeformed chip *t*, which proceeds to become deformed chip thickness t_c. Large forces are generated during the cutting process. The cutting force F_c acts in the direction of cutting velocity and the thrust force F_t acts normal to the cutting velocity in the direction perpendicular to workpiece. A knowledge of the basic force relationships and the associated geometry occurring in the cutting process of metal cutting is a necessity if the solution of engineering problems arising in that field is to be handled by FEM simulations.

1.4 Principles of Finite Element Modeling

Finite element analysis is an approximate numerical analysis tool to study the behavior of a continuum or a system to an external influence, such as stress, heat and pressure. This involves generation of a mathematical formulation of the physical process followed by a numerical solution of the mathematics model. Basic concept of finite element method involves division of a given domain into a set of simple sub-domains, called, finite elements accompanied with polynomial approximations of solution over

each element in terms of nodal values and applying the calculated finite solutions to the whole geometry to solve the problem. The advantage of finite element method is, it provides approximate solutions to complex problems that are difficult to solve analytically. Finite element analysis involves three stages of activity, namely, pre-processing, processing and post-processing. Pre-processing involves the preparation of data, such as nodal coordinates, connectivity, boundary conditions, and loading and material information. The processing stage involves stiffness generation, stiffness modification, and solution of equations, resulting in the evaluation of nodal variables. Other derived quantities, such as gradients or stresses may be evaluated at this stage. The post-processing stage deals with the presentation of results. Typically, the deformed configuration, mode shapes, temperature and stress distribution are compared and displayed at this stage. A complete finite element analysis is a logical interaction of these three stages.

1.5 Metallurgical Aspects of Titanium alloys

Titanium alloys have been extensively studied over the past few decades due to their important technological applications. Their high strength, low density, corrosion resistance, good formability, weldability, and good metallurgical stability prompted the use of these alloys in a wide variety of applications ranging from aircraft engine and structural components to biomedical implants. Among titanium alloys, Ti 6Al-4V accounts for the largest share of the present market and hence studied in depth. Ti 6Al-4V is currently used in a wide range of low and high temperature applications, such as blades and other components for turbines in aircraft engine applications, steam turbine blades,

marine components, structural forgings and biomedical implants [7]. Despite the increased usage and production of titanium alloys, they are expensive when compared to many other metals because of the complexity of the extraction process, difficulty of melting, and problems associated with fabrication and machining. In order to improve processing as well as to lay ground to new titanium alloys, it is important to understand the deformation mechanisms and microstructural evolutions associated with these deformations. Titanium alloys are usually divided into four main groups according to their basic metallurgical characteristics: α-alloys, near α-alloys, α-β alloys, and β-alloys [8].

α-alloys: This group contains α stabilizers, sometimes in combination with neutral elements, and hence have an α-phase microstructure. One such single-phase α-alloy, Ti-5Al-2.5Sn, is still available commercially and is the only one of its type to survive besides commercially pure titanium. The alloy has excellent tensile properties and creep stability at room temperature and elevated temperatures upto 300°C. α-alloys are used chiefly for corrosion resistance and cryogenic applications.

Near α-alloys: These alloys are highly α-stabilized and contain only limited quantities of β-stabilizing elements. They are characterized by a microstructure consisting of α-phase containing only small quantities of β-phase. Ti-8Al-1Mo-IV and Ti-6Al-5Zr-0.5Mo-0.25Si are examples of near α-alloys. They behave more like α-alloys and are capable of operating at greater temperatures of between 400°C and 520°C.

α-β alloys: This group of alloys contains additions of α- and β-stabilizers and possess microstructures consisting of mixtures of α- and β-phases. Ti 6Al-4V and Ti-4Al-2Sn-4Mo-0.5Si are its most common alloys. They can be heat-treated to high strength

levels and hence are used chiefly for high strength applications at elevated temperatures of between 350°C and 400°C.

β-alloys: These alloys contain significant quantities of *β*-stabilizers and are characterized by high hardenability, improved forgeability, and cold formability as well as high density. Basically, these alloys offer an ambient temperature strength equivalent to that of *α*-*β* alloys but their elevated temperature properties are inferior to those of the *α*-*β* alloys.

Ti 6Al-4V, an alloy introduced in 1954, comes as close to being a general-purpose grade as possible in titanium. In fact, it is considered as the workhorse of titanium alloys and is available in all product forms. In Ti 6Al-4V, both *α*- and *β*-phases are Al solid solutions in Ti.

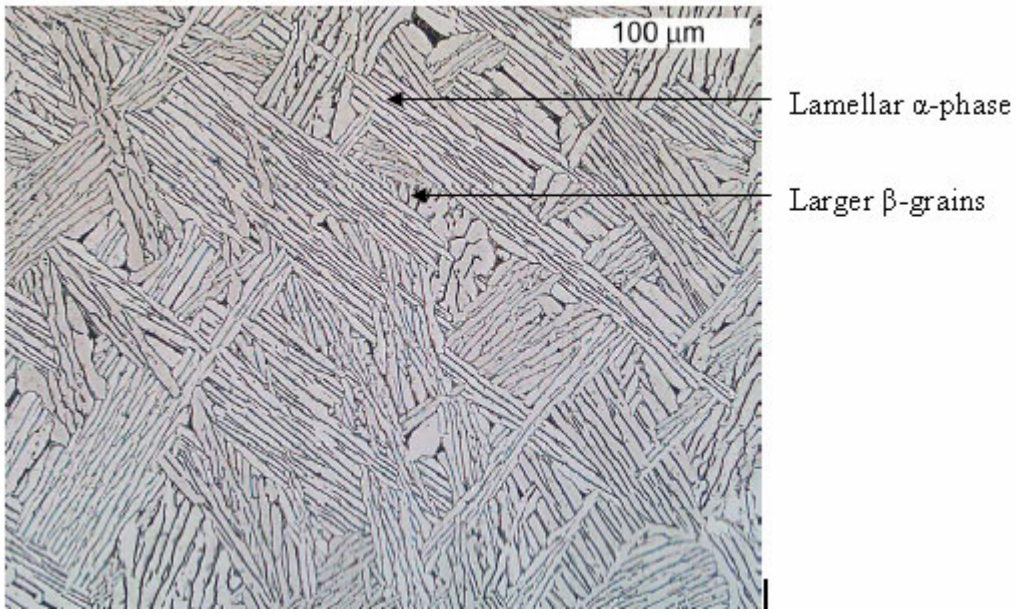

Fig 1.2 Microstructure of Ti 6Al-4V alloy showing primary *α*-phase and transformed *β*- grains [44]

Various impurity atoms, such as O, C, N, and H are usually present. *β*-phase may be stabilized at room temperature by adding *β*-stabilizing elements such as V, Fe and Mn. At room temperature, stabilized *β*-phase contains more V than nominal 4%. Above

527°C, α transforms to β-phase, while above 980°C the whole microstructure is composed of equiaxed β grains. The flow stress of this alloy is strongly dependent on temperature and deformation rate [10]. At temperatures above 527°C, the flow stress decreases sharply with temperature while the strain rate sensitivity increases. The flow mechanisms and kinetics are different in these two phases. This renders to a large number of deformation mechanisms responsible for the macroscopic behavior of the alloy. Their identification is important for understanding the mechanical response of this alloy.

1.6 Machinability aspects of Ti 6Al-4V

Machinability is defined as the ease or the difficulty with which a material can be machined under a given set of cutting conditions including cutting speed, feed, and depth of cut. It is mainly assessed during the cutting operation by measuring component forces, chip morphology, surface finish generated and tool life. The machinability of Ti 6Al-4V and other titanium alloys has not kept pace with advances in manufacturing processes due to their several inherent properties [7, 8]:

1) Its high chemical reactivity with almost all tool materials results in rapid wear of the tool at high cutting speeds. Also the tendency to weld to the cutting tool during machining increases leading to chipping and premature failure.
2) Its low thermal conductivity increases the temperature at the tool/workpiece interface, which affects the tool-life adversely.
3) Its high melting temperature and high temperature strength further impairs its machinability.

4) Besides high cutting temperatures, high mechanical pressure and high dynamic loads in machining of titanium alloys result in rapid tool wear.

5) Its low modulus of elasticity can cause slender workpieces to deflect more than comparable pieces of steel. This can create problems of chatter, tool contact and holding tolerances.

Despite the increased usage and production of this alloy, it is expensive when compared to many other metals and alloys because of the complexity of the extraction process, difficulty of melting and problems during machining and fabrication. Serious vibrations are often encountered during machining that impose limit on the material removal rate, and consequently, productivity. Also this alloy is spectacular to machine because of sparks generated at high speeds. Most tool materials used for machining this alloy wear rapidly even at moderate cutting speeds. Titanium alloys are generally difficult to machine at cutting speeds over 30 m/min with HSS steel tools and over 60 m/min with cemented tungsten carbide tools. Other types of tool materials, including ceramic, diamond and cubic boron nitride are highly reactive with titanium alloys and consequently not used in the machining of these alloys.

These problems can be minimized by employing very rigid machines, using proper cutting tools and set-ups, using low cutting speeds, maintaining high feed rates, minimizing cutting pressures, providing copious coolant flow and designing special tools or non-conventional cutting methods.

1.7 Mechanism of Shear-Localized Chip Formation in Ti 6Al-4V

Titanium and other aerospace structural alloys are extremely difficult to machine at high cutting speeds due to limitations associated with its several inherent properties. It

has been observed that in metal cutting the thermo-mechanical behavior at the workpiece/tool interface significantly influences the chip morphology, which in turn affects the tool life. In order to increase tool life and productivity in machining these alloys it is necessary to study the mechanism of chip formation and its effect on machinability and tool life. Depending on the type of workmaterial, its metallurgical conditions and the cutting conditions used, three types of chip formation are commonly encountered in metal cutting process. They are the continuous chip, shear-localized chip and discontinuous chip. Traditionally most of the investigations on metal cutting have focused on the continuous chip formation because continuous chip is an ideal chip for analysis as it is relatively stable and many conditions can be simplified. However, long continuous chips are not preferred in machining because, in practice they interfere with the process and may cause unpredictable damage on machined surface and tool. Shear-localized chips are found in the case of most difficult-to-machine materials with poor thermal properties. This type of chip on the other hand is easier to break and considered as a relatively ideal chip to dispose off when the machining process is automated.

In the case of machining Titanium alloys, chip is segmented and the strain in it is not uniformly distributed but is confined mainly to narrow bands between the segments. Whereas in continuous chip formation, the deformation is largely uniform. The sequence of events leading to segmented chip formation when machining Ti 6Al-4V was described by Komanduri and Von Turkovich [11] based on a detailed study of video sequence of low speed machining experiments conducted inside the scanning electron microscope, high speed movie films of the chip formation process at higher speeds and the micrographs of midsections of the chips. The mechanism of chip formation when

machining Ti 6Al-4V was found to be different from the continuous chip formation [26]. There are two stages involved in this process. One stage involves plastic instability and strain localization in a narrow band in the primary shear zone leading to catastrophic shear failure along the shear surface. The other stage involves gradual build-up of segment with negligible deformation by the flattening of the wedge-shaped work material ahead of the advancing tool. Generally, adiabatic shearing caused by thermo-mechanical instability is held responsible for this process. This nature of instability, frequently referred to as adiabatic shear, was originally expressed by Recht [12] as one in which the rate of thermal softening exceeds the rate of strain hardening i.e., the slope of the shear stress-shear strain curve becomes zero. Also, alternative theories have been formulated based on damage models and crack formation processes which is probably applicable at low speeds. Finite element simulations of machining a Ti 6Al-4V alloy, allows study of chip formation and the mechanism of chip segmentation in detail. Such simulations have shown that it is indeed possible to form strongly segmented chips by the described process without the necessity of crack formation.

1.8 Thesis outline

A brief description of each chapter in this study is given in the following:

Chapter 1 gives a brief introduction of finite element simulation of the cutting process, its historical developments and principles, metallurgical aspects and machinability issues of Ti 6Al-4V alloy and mechanism of shear-localized chip formation in Ti 6Al-4V.

Chapter 2 presents literature review on numerical analysis of chip segmentation, experimental work on Ti 6Al-4V alloy and finite element simulations of shear-localized chip formation in machining a Ti 6Al-4V alloy.

Chapter 3 contains finite element formulations of metal cutting mechanics, friction along the tool-chip interface, contact conditions, adaptive remeshing and chip formation.

Chapter 4 gives a brief description of machinability issues of Ti 6Al-4V alloy and outlines the rationale and motivation behind this work along with the objectives and research approach.

Chapter 5 deals with the mechanism of shear-localized chip formation and explains the criterion used in this study to simulate it. This chapter also illustrates the metallurgical aspects of Ti 6Al-4V alloy that influence this type of chip formation in machining.

Chapter 6 gives a description of material model used to represent deformation behavior of Ti 6Al-4V alloy under high strains, strain rates, and temperatures. This chapter also derives the equations of Recht's catastrophic shear failure criterion and stress update algorithm used in the user-defined subroutine code (UMAT).

Chapter7 presents the physical properties of Ti 6Al-4V alloy, parameters of Johnson-Cook material model, simulation approach and cutting conditions used. This chapter also provides chip formation process, temperature and plastic strain distribution in the chip, and comparison of finite element simulations with experimental results reported in the literature. Finally, it discusses the effect of cutting speed, feed rate, rake

angles and coefficient of friction on cutting forces, temperatures, strains and chip segmentation.

Chapter 8 draws conclusions on the work done in this study and presents proposed scope for future work.

CHAPTER 2

LITERATURE REVIEW

2.1 Numerical Study of Shear-Localized Chip Formation

Over the past ten years or so, numerical study of the machining processes has been the subject of intense research in which various aspects of shear-localized chip formation, discontinuous chip formation and algorithms for element separation have been addressed. Various criteria for Shear-localized chip formation, such as effective strain criterion, maximum principal stress criterion, maximum shear stress criterion, catastrophic shear failure criterion and so on have been utilized by many researchers for the chip formation process using FEM.

According to Xie *et al.* [13], most shear-localized chips are formed by flow (shear) localization during the chip deformation. Some bands of intense shear dividing the chip into segments occur in metal cutting process. Accordingly, this band is a very thin layer with extremely concentrated shear strains, which may cause chip to become easily separated and broken. They developed a mechanistic model to predict quantitatively the critical cutting conditions for a shear-localized chip formation. This was done by establishing a relationship between the flow localization parameter and related governing cutting conditions, i.e. cutting speed and feed rate. Flow localization parameter β is defined as

$$\beta = -\frac{\sqrt{3}}{m}\left[\frac{n}{\gamma} + \frac{0.9\left(\frac{\partial \tau}{\partial T}\right)}{\rho c\left(1+1.328\sqrt{\frac{K_1\gamma}{Vf}}\right)}\left(n+1-\frac{0.664\sqrt{\frac{K_1\gamma}{Vf}}}{1+1.328\sqrt{\frac{K_1\gamma}{Vf}}}\right)\right] \tag{2.1}$$

where m is strain rate sensitivity parameter, n is strain hardening exponent, K_1 is thermal diffusivity of work material, γ is shear strain and T is temperature. The governing cutting process parameters, cutting speed V and feed rate f are associated with possible onset of shear localization.

The flow localization parameter, β is used to rank the tendency for strain concentration within a material. A certain critical value of β must exceed to reach at the onset of strain localization. The above equation is used to predict the flow localization parameter, β, for given cutting conditions and material properties. The value of β increases as either the cutting speed V increases or the feed rate f increases. Usually, β at which shear banding is possible is determined experimentally and for Ti 6Al-4V the value is 4.41. The formation of shear-localized chip involves several material, mechanical, and thermophysical properties including density, specific heat, strain hardening exponent, thermal diffusivity, strain rate sensitivity and conductivity. Basically, as a cutting condition (Vf) reaches the critical value at which shear-localized chips are formed, the plastic deformation rate becomes high and tool-workpiece friction becomes more severe, increasing the rate of heat generation. The adiabatic or quasi-adiabatic condition may be reached due to high accumulation of heat. In this case, temperature can be very high locally in some places of the workpiece, resulting in further thermal softening. This further thermal softening reduces strain-hardening capacity so the

instability takes place in a narrow band of the chip. Thus, β may be used as material property to judge and predict shear localization.

Marusich *et al.* [14] implemented a fracture model that allows for arbitrary crack initiation and propagation in the regime of shear-localized chips. They presented a model of high-speed machining using a lagrangian code to simulate large unconstrained plastic flow with continuous adaptive meshing and remeshing as principal tools for sidestepping the difficulties associated with deformation induced element distortion. Accordingly, when slip induced transgranular cleavage is the dominant mechanism, fracture of mild steel can be described in terms of a critical stress criterion. The critical stress σ_f appears to be relatively independent of temperature and strain rate and can be inferred from toughness K_{IC} through the small scale yield relationship

$$\sigma_f = \frac{K_{IC}}{\sqrt{2\pi l}} \tag{2.2}$$

The critical distance l correlates with the spacing of the grain boundary carbides. Under mixed-mode conditions, such as expected in machining, the crack might kink or follow a curved path as it grows. To predict the crack trajectory under conditions of brittle fracture, they adopted maximum hoop stress criterion, according to which crack propagates along the angle θ from the crack face at which hoop stress $\sigma_{\theta\theta}$ attains a relative maximum. Combining maximum hoop stress along the angle θ $\max_{\theta} \sigma_{\theta\theta}$ and critical stress criterion, the criteria for mixed-mode crack growth is given by

$$\max_{\theta} \sigma_{\theta\theta}(l, \theta) = \sigma_f \tag{2.3}$$

The critical crack tip opening displacement (CTOD) criterion for mode I crack propagation can be recast as the attainment of critical value ε^p_f of the effective plastic strain at a distance l directly ahead of the crack tip. The criterion can be expressed as

$$\max_{\theta} \varepsilon^p(l, \theta) = \varepsilon^p{}_f \tag{2.4}$$

with the understanding that crack propagates at an angle θ for which the criterion is met.

The critical effective plastic strain can be estimated as

$$\varepsilon^p{}_f \approx 2.48e^{-1.5p/\sigma} \tag{2.5}$$

where $p = \sigma_{kk}/3$ is the hydrostatic pressure.

Ceretti *et al.* [15] implemented the Cockroft and Latham damage criterion for material fracture [16]. According to the numerical model, material fracture is simulated by deleting the mesh elements that have been subjected to high deformation and stress. Accordingly, the damage criterion is evaluated by the Equation 2.6:

$$C_i = \int_0^{\varepsilon_f} \bar{\sigma} \left(\frac{\sigma^*}{\bar{\sigma}} \right) d\bar{\varepsilon} \tag{2.6}$$

where C_i is the critical damage value given by uniaxial tensile test, ε_f the strain at the breaking condition, σ^* is the maximum stress. The criterion predicts the damage when the critical value C_i is exceeded. The damage is evaluated for each element of the workpiece. Element deletion occurs when damage value is reached. To simulate the shear-localized chip formation they used commercial software DEFORM2D and customized it with new algorithms incorporating the damage criterion.

Hashemi *et al.* [17] developed a fracture algorithm for simulating chip segmentation and separation during orthogonal cutting process. This criterion evaluates the principal stress at each node in each computational cycle. If the magnitude of principal stress exceeds a pre-determined value, which can be taken as material fracture strength, a crack is assumed to initiate and propagate along the direction normal to the stress vector.

Obikawa and Usui [18] proposed an effective strain based criterion in their FEM simulation of serrated chip formation in cutting Ti 6Al-4V. They postulated that when the effective plastic strain at specific node reaches the preset critical value, this node is then separated indicating crack initiation and propagation. According to them, in the machining of titanium alloys, serrated chips are produced due to ductile cracks propagating from the chip free surface. The following fracture criterion was applied for the crack initiation and propagation:

$$\bar{\varepsilon}^{p} > \varepsilon_c \tag{2.7}$$

where $\varepsilon_c = -\max\left[0.075 \ln\left(\frac{\dot{\bar{\varepsilon}}^{p}}{100}\right), 0\right] - \frac{\sigma_{ii}}{37.8} + 0.09 \exp\left(\frac{\theta + 273}{293}\right)$

where max [,] is a function giving the maximum value in the bracket. This criterion is based on equivalent plastic strain. This predetermined critical strain value ε_c is a function of strain, strain rate $\dot{\bar{\varepsilon}}^{p}$, hydrostatic pressure σ_{ii}, and temperature θ.

Rice [19] simulated shear-localized chip formation using critical shear strain criterion. They developed the failure criterion from the studies of mechanism of chip segmentation using photographs of segmented chips taken at various stages during machining. Accordingly, they proposed that chip transforms from continuous to segmental when nominal shear strain in the primary shear zone reaches critical value.

Iwata *et al.* [20] proposed the following stress-strain based criterion in their FEM analysis of orthogonal cutting as:

$$\int_0^{\varepsilon_f} (\bar{\varepsilon} + b_1\sigma_m + b_2)\, d\bar{\varepsilon} = b_3 \tag{2.8}$$

where the constants b_1, b_2 and b_3 are given as functions of metallurgical properties However, the authors claimed that obtaining these constants needs complicated experiments that requires high pressure.

Shivpuri *et al.* [21] implemented the deformation energy-based criterion proposed originally by Cockroft and Latham [16] to simulate shear-localized chip formation of Ti 6Al-4V using FEM. This criterion was based on critical damage value given by:

$$C_i = \int_0^{\varepsilon_f} \bar{\sigma}\left(\frac{\sigma^*}{\bar{\sigma}}\right) d\bar{\varepsilon} \tag{2.9}$$

The C_i value is a workpiece material constant and does not depend on the workmaterial or the tool material. The C_i value is a function of temperature and microstructure of the point of interest and can be expressed as $C_i = f$ (T, m), where m denotes the microstructure. When the temperature is below the β-transformation temperature, the microstructure is presented by $\alpha+\beta$, otherwise microstructure is β. The critical damage value is evaluated for each element of the workpiece. Element deletion occurs when damage value is reached. Thus the crack is initiated and propagated.

In the early 1970's Nakayama [22] found that saw-tooth chips were produced when highly cold worked (60 percent reduction) 40/60 (Zn/Cu) brass was turned under orthogonal conditions. Based on that he proposed a theory of saw-tooth chip formation. Accordingly, shear crack initiates at the free surface of the chip in the primary shear zone and runs from the surface downward along shear plane towards the tool tip. With further advance of the tool, the chip glides outward like a friction slider along the cracked surface until the next crack forms and a new cycle begins. A shear crack will initiate at the free surface of the chip where the crack arresting normal stress is zero and proceeds

downward along the shear plane toward the tool tip. Initially the crack will be continuous across the width of the chip but will become discontinuous as higher crack arresting normal stresses are encountered.

Owen and Vaz Jr. [23], applied computational techniques to investigate high-speed machining. They focused on the simulation of Ti 6Al-4V machining involving material failure due to adiabatic strain localization and addressed important issues, such as adaptive mesh refinement and material failure. According to them, material failure under adiabatic strain localization conditions results from the accumulation of large plastic deformation and microscopic damage. They employed a two-parameter model to describe material failure, i.e. a failure indicator (or fracture criterion), I, and an energy release factor, W_r. Accordingly, the former indicates failure onset and the latter defines the amount of energy released during the softening process as shown in the Fig. 2.1.

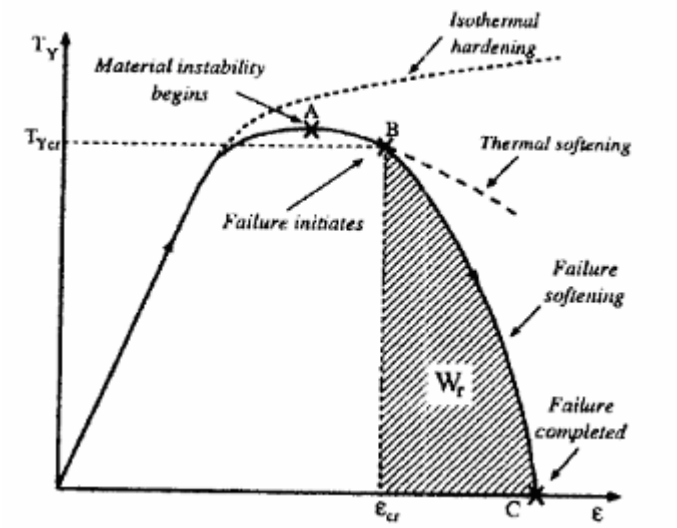

Fig. 2.1 Stress-strain diagram for a combination of strain hardening, thermal softening and failure softening [23]

The failure softening path, B-C, is governed by the softening modulus, E_t, as

$$E_t = \frac{\partial T_Y}{\partial \varepsilon} = -\frac{T^2{}_{Y,cr} h_e}{2W_r} \tag{2.10}$$

where h_e is the characteristic length of the particular element, T_Y is the true stress of the material at yield point and $T_{Y,cr}$ is the critical yield stress of the material where failure initiates. They adopted a material failure criterion based on the uncoupled integration of Lemaitre's ductile model. Lemaitre postulated that damage progression is governed by void growth represented by the damage evolution equation

$$\dot{D} = -\dot{\gamma}\frac{\partial \psi}{\partial Y} = \frac{\dot{\gamma}}{1-D}\left(\frac{-Y}{r}\right)^s \tag{2.11}$$

where $\dot{D}$ is the damage variable, r and s are damage parameters, Ψ is the dissipation potential and Y is the damage strain energy release rate. They also incorporated a stress update algorithm which is called as operator-split algorithm to which the computation of the fracture indicator and failure softening were added. The methodology consists of decomposing the problem into elastic and plastic components, in which the former assumes that deformation is entirely elastic whereas the latter solves a highly nonlinear system of equations comprising the constitutive relations, evolution laws and plastic consistency using the elastic predictor stage as the initial condition. In order to overcome the problem of severe element distortion when using lagrangian formulations in their simulations, they incorporated error estimator based on the principle that the adaptive procedure should not only capture the progression of the plastic deformation but also provide refined meshes at regions of possible material failure.

Samiatin and Rao [24] developed another model for shear-localization, which incorporates a simple heat transfer analysis, and material properties, such as the strain-hardening rate, the temperature dependence of flow stress, and the strain rate sensitivity of the flow stress to establish the tendency towards the localized flow. Using their

literature data, they found the non-uniform flow in metal cutting to be imminent when the ratio of the normalized flow-softening rate to the strain rate sensitivity is equal to or greater than 5.

Recht in 1964 [12] developed a classical model of catastrophic shear instability for shear localization in metals under dynamic plastic conditions. Accordingly, catastrophic shear will occur at a plastically deforming location within a material when the slope of the true stress-strain function becomes zero. He formulated a simple criterion for catastrophic slip in the primary shear zone based on the thermo-physical response of the work material under the conditions of cutting. The catastrophic slip can be written as:

$$0 \le \frac{\dfrac{\partial \tau}{\partial \varepsilon}}{-\dfrac{\partial \tau}{\partial \theta}\dfrac{d\theta}{d\varepsilon}} \le 1.0 \qquad (2.12)$$

where τ, ε and θ refer to the shear stress, shear strain, and temperature, respectively. Material will shear catastrophically when this ratio lies between zero and one; catastrophic shear will be imminent when the ratio equals to one.

Komanduri and Hou [25] developed a thermal model for the thermoplastic shear instability in the machining of a Ti6Al4V alloy. It is based on the analysis of the shear-localized chip formation process due to various heat sources (primary, preheating and image) in the shear band. They determined the temperature in the shear band analytically using the Jaeger's classical stationary- and moving heat source methods and used Recht's catastrophic shear instability model to determine the onset of shear localization. Accordingly, the shear stress in the shear band is calculated at the shear band temperature and compared with the shear strength of the bulk material at the preheating temperature. According to Recht, if the shear stress in the shear band is less than or equal to the shear

strength of the bulk material, then shear localization is imminent. The cutting speed at which this occurs is taken as the critical speed for the onset of shear localization. The effect of depth of cut on the critical speed is determined and found that lower the depth of cut, higher the critical speed for onset of shear localization. The cutting speed for the onset of the shear localization in the machining of Ti 6Al-4V was found to be extremely low, ~0.42 m/min for a depth of cut of 0.2 mm. A best-fit relationship between the critical cutting speed for shear localization and depth of cut was developed using the analytical data and is given by

$$V_{cri} = 0.082667 \times a_0^{-1.0054} \tag{2.13}$$

2.2 Shear-Localized Chip Formation in Ti 6Al-4V: Experiments

Numerous studies on the machining of titanium alloys (analysis of chip formation and cutting forces) have been carried out in a range of cutting velocities lower than 5 m/s, by Komanduri and von Turkovich [11], Komanduri [26], Narutaki and Murakoshi [47], Larbi [50], Bayoumi and Xie [39] and Diack [49]. In the work of Hoffmiester *et al.* [48] and Molinari *et al.* [28], larger velocities were considered in the range of 20 to 100 m/s. These studies illustrated several unique features associated with the machining of these alloys, including the following [26]:

(1) The role of poor thermal properties of titanium alloys which interact with the physical properties in controlling the nature of plastic deformation (i.e. strain localization) in the primary zone is illustrated.

(2) Periodic gross inhomogeneous deformation occurs in the primary zone.

(3) Instability in the chip formation process results in the segmented or cyclic chip.

(4) Oscillations in the cutting and thrust components of force cause chatter and the need to have a rigid tool-work-machine tool system.

(5) High tool-chip interface temperatures and high chemical reactivity of titanium in machining with almost any tool material are responsible for the rapid tool wear.

(6) The low modulus of elasticity which decreases rapidly, even at moderate temperatures, causes undue deflections of the workpiece, especially when machining slender parts, and inaccuracies in the finished part.

Chip formation studies were conducted at various machining speeds from an extremely low speed of 0.127 mm/min to a moderately high speed of 5.1 m/s. The low speed experiments were conducted inside a scanning electron microscope and the cutting process was recorded on a video tape. Chip formation studies at higher cutting speeds were conducted on a lathe with the aid of a Hi-Cam high-speed movie camera (camera speed up to 8000 frames/s) using the technique developed earlier by Komanduri and Brown [19]. The sequence of events leading to cyclic chip formation when machining titanium was described by Komanduri and von Turkovich [27] based on a detailed study of videotapes of low speed machining experiments inside the scanning electron microscope, high-speed movie films of the chip formation process at higher speeds and the micrographs of the mid section of the chips. Accordingly, they described two stages in the chip formation process. One stage involves plastic instability and strain localization in a narrow band in the primary shear zone leading to catastrophic shear failure along a shear surface. The other stage involves gradual build-up of the segment with negligible

deformation by the flattening of the wedge-shaped work material ahead of the advancing tool.

Molinari *et al.* [28] carried out experimental analysis of shear localization and chip segmentation in Ti 6Al-4V at cutting speeds in a range from 0.01 to 73 m/s. To cover a wide range of cutting speeds, two different devices were used. The low cutting speeds (0.01 to 1.0 m/s) were obtained with a universal high-speed testing machine. The second arrangement was constituted by an airgun setup for speeds from 1.0 to 73 m/s. Accordingly, to avoid fracture of the tools at high impact velocities, small depths of cut were used. All tests were carried out with carbide tools with a rake angle 0° and the tools were square shaped without chip-breaker. The collected chips were embedded into a resin and the lateral section polished and etched for observation in the optical microscope. The following conclusions were drawn from their experimental studies:

(1) Chip segmentation was observed to be related to adiabatic shear banding.

(2) Adiabatic shear bands are the manifestation of a thermomechanical instability resulting in the concentration of large shear deformations in narrow layers.

(3) For velocities lower than 1.2 m/s, chip serration is related to the development of deformed shear bands as shown in Fig. 2.2, which are the manifestation of thermo-mechanical instability. However, at low values of cutting velocities, the instability process is weak and the localization is not as sharp as for higher velocities.

(4) The patterning of adiabatic shear bands were observed experimentally by measurements of shear band width and chip segment width. Patterning is seen to be strongly dependent on cutting velocity V.

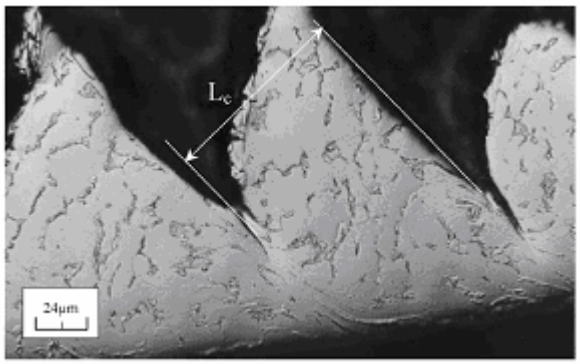

Fig. 2.2 Adiabatic shear-localized chip in a Ti 6Al-4V alloy obtained by orthogonal cutting at a cutting speed of 1.2 m/s [28]

Barry *et al.* [29] conducted orthogonal cutting tests to investigate the mechanism of chip formation and to assess the influences of such on acoustic emission (AE) for a Ti 6Al-4V alloy of 330HV with an uncoated P10/P20 carbide tool. Here, AE refers to the transient displacement of the surface of a body, of the order of 10^{-12} m, due to the propagation of high frequency elastic stress waves. The surface displacement is detected by the AE sensor and typically output as a proportional voltage. Accordingly, orthogonal cutting tests were undertaken using a Ti 6Al-4V alloy of 330 HV with uncoated P10/P20 carbide tool with a rake angle of -6° and a clearance angle of 12°. The workpiece used was in the form of a 25 mm diameter disc, 1.1mm in width and was held on a mandrel during cutting. The tests were performed on a Daewoo PUMA 4-3A CNC lathe under a constant surface speed control. Acoustic emission signals were captured with a Kistler wide band piezoelectric AE sensor and the signal amplified and conditioned using a Kistler Piezotron unit.

Fig. 2.3 shows the influence of cutting speed and feed on chip morphology in the orthogonal cutting of Ti 6Al-4V. They classified all chips obtained for different cutting conditions in the range 20-100 µm feed and 0.25-3 m/s cutting speed as either aperiodic saw-tooth or periodic saw tooth. Accordingly, it was seen that with low values of cutting

speed and undeformed chip thickness (e.g., 20 μm), aperiodic saw-tooth chips were produced. Increase in either or both of these parameters resulted in a transition from aperiodic to periodic saw-tooth chip formation. They observed occurrence of welding between chip and tool during machining and with degree of welding increasing with cutting speed.

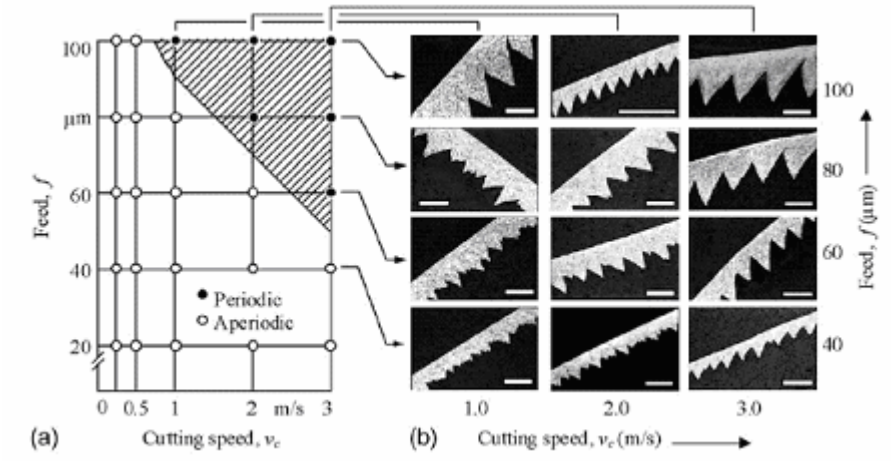

Fig. 2.3 Chip morphology as a function of cutting speed and feed in orthogonal cutting of a Ti 6Al-4V alloy [29]

In machining of Ti 6Al-4V, Barry *et al.* [29] observed that catastrophic failure occurs not only within the primary shear zone, but also within the weld formed between the chip and the tool rake face and the fracture of such welds appears to be the dominant source of acoustic emission in machining Ti 6Al-4V with cutting speeds greater than 0.5 m/s. This is precisely the mechanism proposed by Komanduri and von Turkovich [11] (See Fig.5.1 in chapter 5).

Xie and Bayoumi [13] conducted orthogonal cutting tests and various metallurgical analysis techniques were used to examine the chip formation process and the role of shear instability. Cutting speeds were varied from 0.5 to 8.0 m/s and the feed

rates from 0.03 to 0.5 mm/rev. The following are their conclusions from the experimental study:

(1) The results from metallurgical studies showed no diffusion-type phase transformation in the machined chips, while the X-ray diffraction tests identified some non-diffusional phase transformation from β-phase into α-phase during chip formation.

(2) Intensive shear takes place in a narrow zone rather than in a plane as is often assumed by some investigators in the analysis of orthogonal machining process.

(3) For each work material there exists a critical value (*Vf*) of chip load at which shear localized chips were observed. The cutting conditions also influence the shear banding in a way that the shear banding frequency increases with an increase in feed rate or a decrease in cutting speed.

Shivpuri *et al.* [21] conducted experiments on Ti 6Al-4V using a CNC turning center at cutting speeds of 60, 120 and 240 m/min, feed rates of 0.127 and 0.35 mm/rev and depth of cut of 2.54 mm. They collected the deformed chips for different cutting speeds and observed the chip morphology under a microscope. The cutting forces were measured with a Kistler dynamometer (Type 9121). A general carbide tool was used with a rake angle of 15° and a relief angle of 6°. They showed that (Fig. 2.4) as the cutting speed is increased, the chip fracture observed at lower cutting speeds gradually reduces, and the flow localization and strain between the serrated chip gradually increases resulting in changing chip morphology (discontinuous chip becoming continuous but serrated). They observed that the crack, which determines the serrated chip during cutting, always occurs in the primary shear zone on the tool tip side and at low cutting

speeds, the crack propagates to the tool tip because the temperature in the chip being formed is much lower than the β-transus temperature. Whereas at high cutting speeds, the crack propagates to the free surface as the temperature in the secondary shear zone at the tool face is much higher than that in the free surface. This temperature is above β-transus

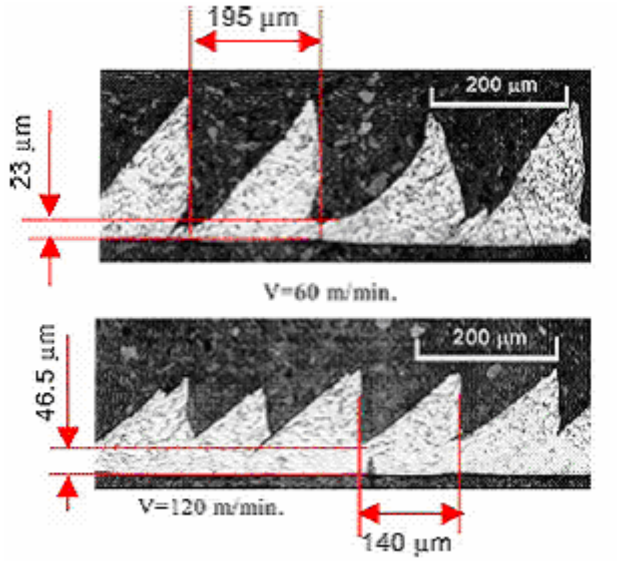

Fig. 2.4 Shear-localized chip formed in machining a Ti 6Al-4V alloy at cutting speeds of 60 and 120 m/min and feed rate of 0.127 mm/rev [21]

temperature and causes microstructural changes resulting in the rise of ductility in the shear zones. The chip just formed during cutting process connects to the workpiece forming the serrated chip morphology.

Ribeiro *et al.* [30] carried out turning tests on Ti 6Al-4V with conventional uncoated carbide tools for cutting speeds of 55, 70, 90 and 110 m/min, using 0.1 mm/rev feed rate and 0.5 mm depth of cut. The objective of this work was to optimize the cutting speed for best finish in the machining of titanium alloy. Fig. 2.5 shows the variation of roughness with the length of cut at different cutting speeds. They found 90 m/min to be the optimum cutting speed for best finish.

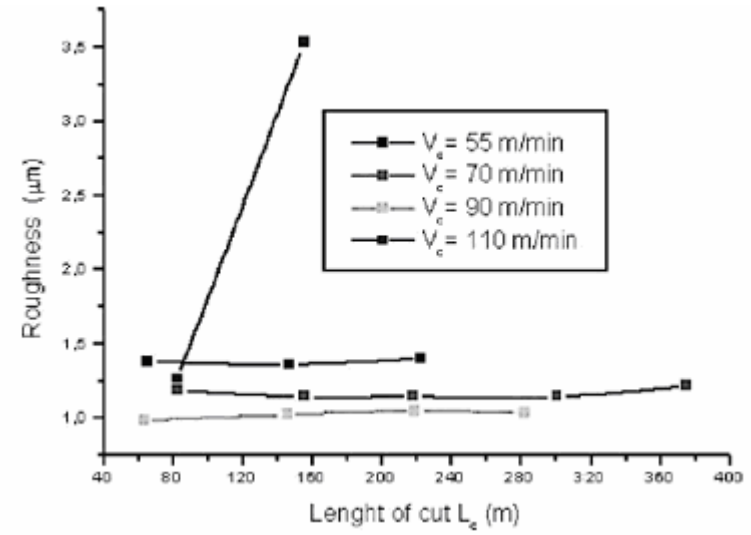

Fig. 2.5 Roughness of workpiece material (Ti 6Al-4V) as a function of cutting length at different cutting speeds [30]

Lee and Lin [31] investigated the high temperature deformation behavior of Ti 6Al-4V alloy by conducting mechanical tests using compression split Hopkinson bar under high strain rate of 2×10^3 s^{-1} and temperatures varying from 700-1100°C in the intervals of 100°C. Fracture features of the specimens after the mechanical tests were observed using optical and scanning electron microscopy. They showed that extensive localized shearing dominates the fracture behavior of this material and adiabatic shear bands run across the specimen. Another important observation made relating to the shear band is the formation and coalescence of voids in an adiabatic shear band, which might lead to variation in mechanical properties of the material. Fig. 2.6 shows a typical array of coalesced voids in a well-developed shear band. Initially, the voids are observed to be spherical, but when the diameters reach the thickness of the shear bands, the voids coalesce and their extension along the shear band results in elongated cavities and smooth-sided cracks.

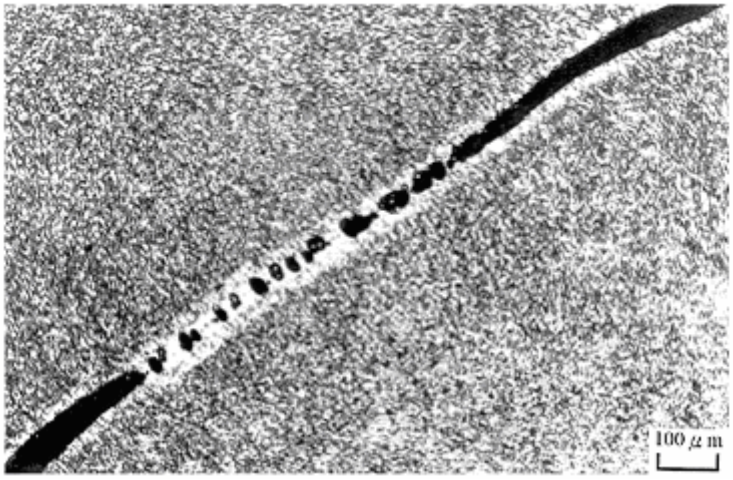

Fig. 2.6 Voids and cracks in an adiabatic shear band of a Ti6Al4V alloy specimen deformed at 700°C and 2×10^{3} s^{-1} strain rate [31]

In each specimen, a transformed adiabatic shear band appears in the microstructure, indicating that a catastrophic localized shear occurred during deformation. Failure analysis of the specimens indicated that adiabatic shear bands are the sites where the fracture of the material occurs, and that the thickness and microhardness of the adiabatic shear bands vary completely with temperature.

Picu *et al.* [10] investigated plastic deformation of Ti 6Al-4V alloy under low and moderate strain rates and at various temperatures. Mechanical testing was performed in the temperature range 650-1340 K and at strain rates from 10^{-3} to 10 s^{-1}. A discontinuity in the flow stress versus temperature curve was reported. Fig. 2.7 shows temperature dependence of the yield stress at low strain rates (10^{-3} s^{-1}) and comparison with the published results. The curve shows discontinuity at temperature $T\sim$ 800 K. At temperatures above 800 K, the flow stress sharply decreases with temperature. The discontinuity observed in the flow stress-temperature curve suggests that additional deformation mechanisms become active at that temperature and this leads to dramatic reduction in strain hardening. Texture has a significant effect on the flow stress at

temperatures below the discontinuity, while higher temperatures rapidly decrease the texture sensitivity. At temperatures in the 1100-1350 K range, phase transformation from α to β becomes the impetus behind the mechanical behavior. Also associated with this

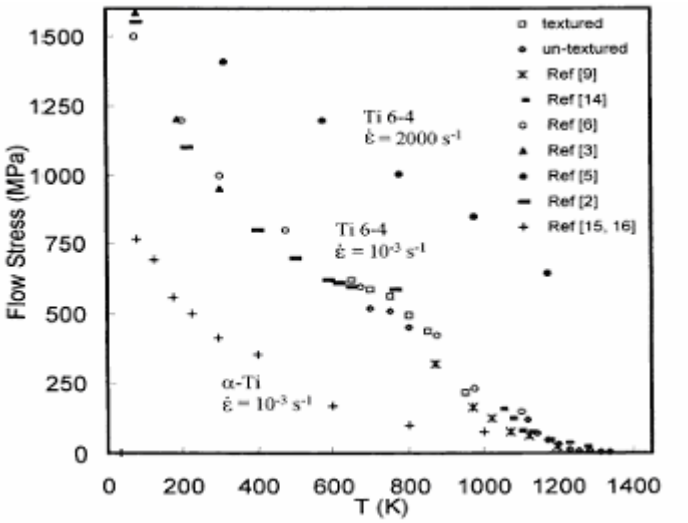

Fig. 2.7 Temperature dependence of flow stress in a Ti 6Al-4V alloy at very low strain rates of 10^{-3} s^{-1} [10]

transformation is a pronounced variation in the strain rate sensitivity (m), with the sensitivity being higher in the 100% β material.

Reissig *et al.* [32] investigated different machining processes, such as drilling, shot peening and electrochemical drilling. According to them, it is usually very difficult or often impossible to measure directly the surface temperatures introduced by machining processes, such as deep hole drilling. Therefore, they presented a post-mortem-method which allows the determination of maximum temperatures during machining by measuring the local vanadium concentration in a Ti 6Al-4V alloy. They proposed a method to determine a local pseudo temperature to determine in regions at a distance as small as 50 nm from the surface. In a Ti 6Al-4V alloy, vanadium is used as a β-stabilizer and highest vanadium concentration is found in the β-phase. By using the method they

proposed, in drilling maximum pseudo temperature occurs at the end of the drilled hole and is very close to the β-transus temperature of Ti 6Al-4V alloy. Initially the temperature was about 490 K and increased linearly by 5 K/mm between the start of the drill hole and the end. They accounted for this increase to be due to insufficient coolant

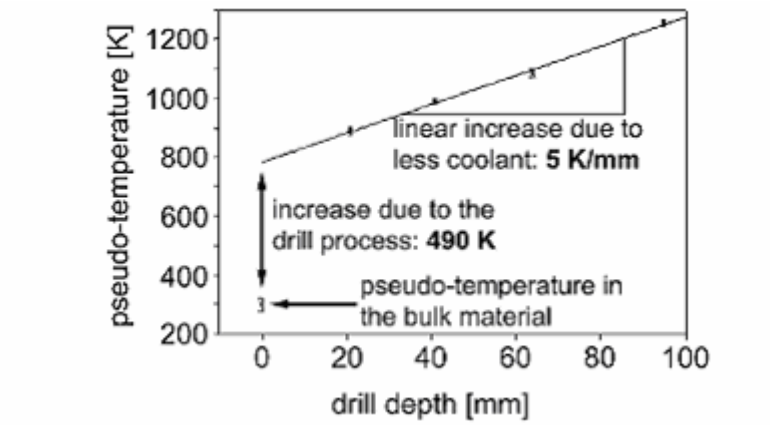

Fig. 2.8 Pseudo-temperature variation with drill depth showing a linear increase [32]

supply. The pseudo-temperature measurements in shot peening showed that the maximum value was 1106 K in a surface region of about 50 nm thickness and the electro chemical drilling showed no significant increase in pseudo temperature.

Lacalle *et al.* [33] conducted milling tests on Ti 6Al-4V alloy to study the tool influence of the tool geometry and coating as well as the influence of cutting conditions on the productivity of the milling process. They used cutting speeds between 11 and 14 m/min, feed between 0.04 and 0.15 mm/tooth, helix angles of 30°, 45°, 60°, number of teeth of 3, 4, 6 and uncoated cemented carbide milling cutters as cutting tools. Based on their studies they reached the following conclusions:

1) Cutting speed has a crucial role in the tool roughening. Serrated chips are found for all the cutting speeds. Fig.2.9 shows serrated chips for 80 m/min and 140 m/min.

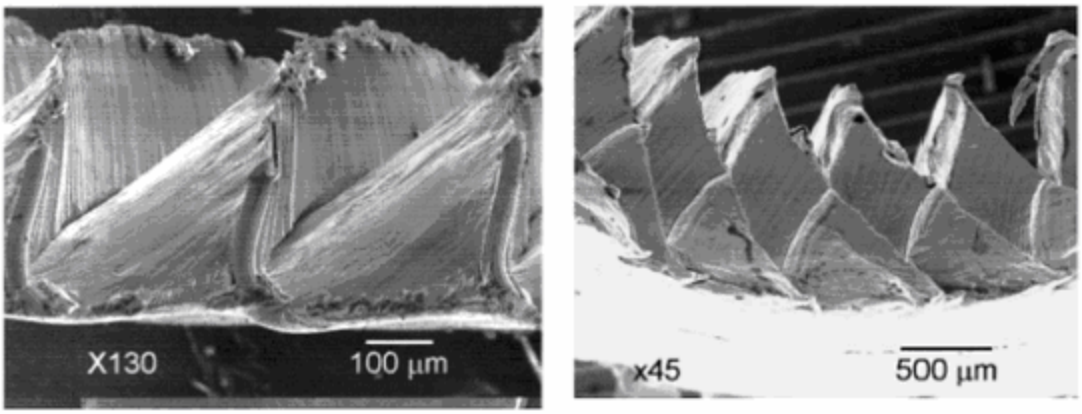

(a) (b)

Fig. 2.9 Serrated chips obtained in machining a Ti 6Al-4V alloy at cutting speeds (a) 80 m/min and (b) 140 m/min [33]

2) For high feed values, thick chips are generated and they result in increasing cutting loads, increasing chip deformation and separation.
3) As far as usage of coating materials for HSS steel tool in the machining of titanium alloys, it is found that flank wear can be delayed with TiCN coatings.

2.3 Shear-Localized Chip Formation in Ti 6Al-4V-FEM Simulations

Xie *et al.* [13] presented a quasi-static finite element model of chip formation and shear banding in orthogonal metal cutting of Ti 6Al-4V using a commercial FEA code (NIKE2D™). The updated Lagrangian formulation for plane strain conditions is used in this investigation. The tiebreak sideline was used to separate the newly formed chip from the workpiece surface. The effective plastic strain is used as the material failure criterion and a strain-hardening thermal-softening model for the flow stress is used for shear-localized chip simulation. A series of finite element simulated machining tests with different tool rake angles ranging from -16° to 20° were carried out at a cutting speed of

5 m/s and a feed of 0.3 mm to study the effect of rake angle on shear band angle and cutting forces. Fig. 2.10 (a) and (b) shows machining process modeled with a negative rake angle -8°. The simulated results show that the effective plastic strain is within a narrow area along the shear zone angle, and the field of the maximum shear stress matches with the area of the primary and secondary shear zones. They reported that the finite element model predicts the detailed deformation in front of the tool tip and the initiation of the shear band.

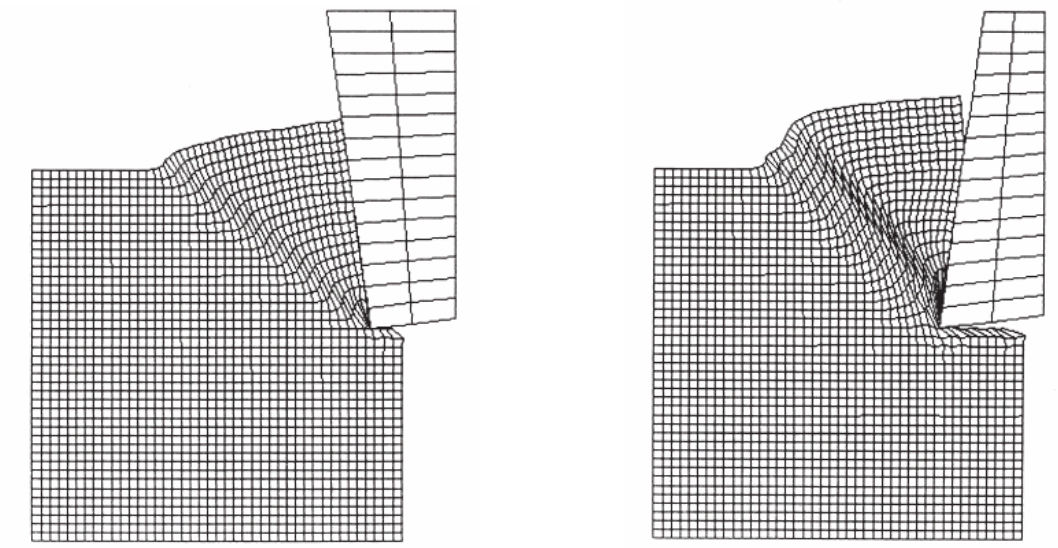

(a) (b)

Fig. 2.10 Chip formation process showing shear localization in finite element simulation of a Ti 6Al-4V alloy at cutting speed of 5m/s and feed 0.3mm using -8° rake angle tool [13]

However, from their investigation, it can be observed that they have not used a reliable material model to represent strain-hardening and thermal-softening behavior of Ti 6Al-4V during metal cutting process as they mentioned in their study that they arbitrarily composed the thermal-softening part of the material behavior by making the stress from strain-hardening part to thermal-softening part to decrease by 50%. Xie *et al.* [13] also mentioned that, they used a debond (node separation) criterion based on critical

effective plastic strain for chip formation. It can be observed from their investigation that they have used an arbitrary value of 0.5 for critical effective plastic strain. Also from the Fig. 2.10 it can be noticed that, they have just shown the onset of chip segmentation and did not show complete chip formation process.

Obikawa and Usui [18] developed a finite element model for the computational machining of titanium alloy Ti 6Al-4V. Fig.2.11 shows the cutting model they used in the finite element analysis. A cemented carbide tool (FGHI) and a titanium alloy (Ti 6Al-4V) (ABCDEF) were modeled with four node (linear) quadratic isoparametric elements. The tool was assumed to be rigid and the finite elements in it were used only for temperature calculations. The cutting speed used was 30 m/min, the undeformed chip thickness was 0.25 mm and the tool rake angle was 20°. The parallelogram ABCF was part of the workpiece to be removed as chip. Two-dimensional elastic plastic analysis was formulated in updated Lagrangian form and procedures needed for metal cutting were developed for unsteady state heat conduction and material nonlinearities. The friction on the rake face and the complicated flow stress characteristic of the titanium alloy at high strain rates and high temperatures were also considered. Fig.2.12 shows the serrated chip formation process in case of the titanium alloy that was obtained by the FEM simulation. In this investigation, to simulate serrated chip formation they used a geometrical criterion based on fracture strain and defined boundary conditions in such a way that crack propagation occurs in the predetermined path. Hence these simulations lack actual physical phenomenon and mechanism of chip segmentation.

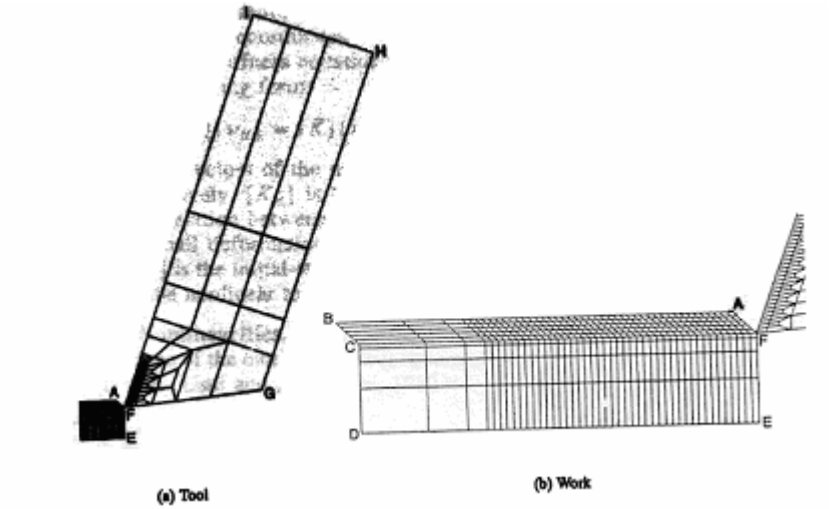

Fig. 2.11 Tool-workpiece mesh system used in finite element simulation of orthogonal metal cutting a Ti 6Al-4V alloy [18]

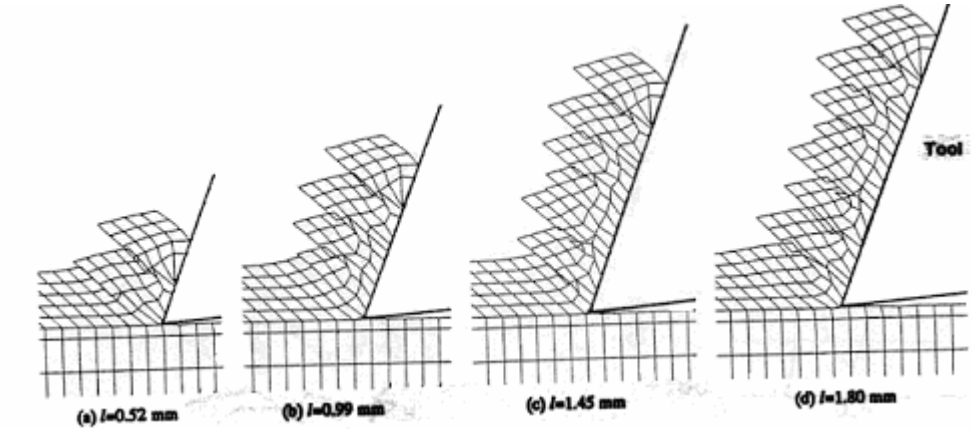

Fig. 2.12 Serrated chip formation with cutting length in finite element simulation of machining a Ti 6Al-4V alloy at cutting speed 30 m/min, feed 0.25 mm and 20° rake angle [18]

Maekawa *et al.* [34] used an iterative convergence method (ICM) to simulate metal cutting process. The ICM uses flow lines which consist of trajectories of particles or a series of finite elements. The chip is supposed to be pre-formed on the surface of the work material and to be stress free. Calculation proceeds by incrementally displacing the workpiece towards the tool so that a load develops between the chip and the tool. A plastic state develops in the chip deformation zone and it is checked with the assumed

chip shape and automatically altered and the calculation is repeated. However, this method simulated only continuous chip. Later, to simulate serrated and discontinuous chips, a sophisticated methodology was developed for approximation of such discontinuity. A failure strain criterion was introduced into the ICM methodology, so that crack initiates at the tool side within the highly deformed workpiece and propagates towards the free surface side, resulting in the periodic segmentation of the chip. Applying this methodology, Ti 6Al-4V alloy machining simulations were carried out at 30 m/min cutting speed and 0.25 mm/rev feed rate using 20° rake angle tool. Fig. 2.13 shows the predicted serrated chip shape in titanium alloy machining simulation. They concluded that serration arises in the chip from a small fracture strain of the alloy and not due to adiabatic shear instability. But then, as stated above, they introduced a failure strain criterion so that crack initiates at the tool side within the highly deformed workpiece and propagates towards the free surface side. And as their simulation approach is based on geometric criterion with preformed chip shape, this work does not represent actual mechanism of chip segmentation observed in machining.

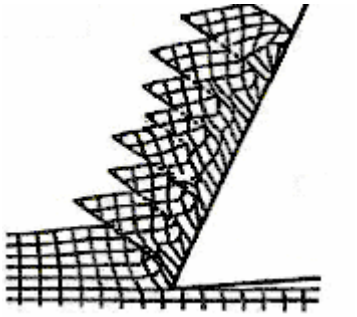

Fig. 2.13 Serrated chip formed in finite element simulation of orthogonal metal cutting of a Ti 6Al-4V alloy at cutting speed 30 m/min, feed 0.25 mm and 20° rake angle [34]

Owen and Vaz Jr. [23], simulated machining of Ti 6Al-4V alloy in which, they addressed such issues as evaluation of the mesh refinement procedure, strain localization

process, and material failure process. The geometry and the initial mesh they used for a rake angle of -3° are depicted in Fig.2.14. An enhanced one-Gauss point element was used in the simulation. The simulations employed an error estimator based on uncoupled integration of Lemaitre's damage model. Tests were undertaken to evaluate the effect of

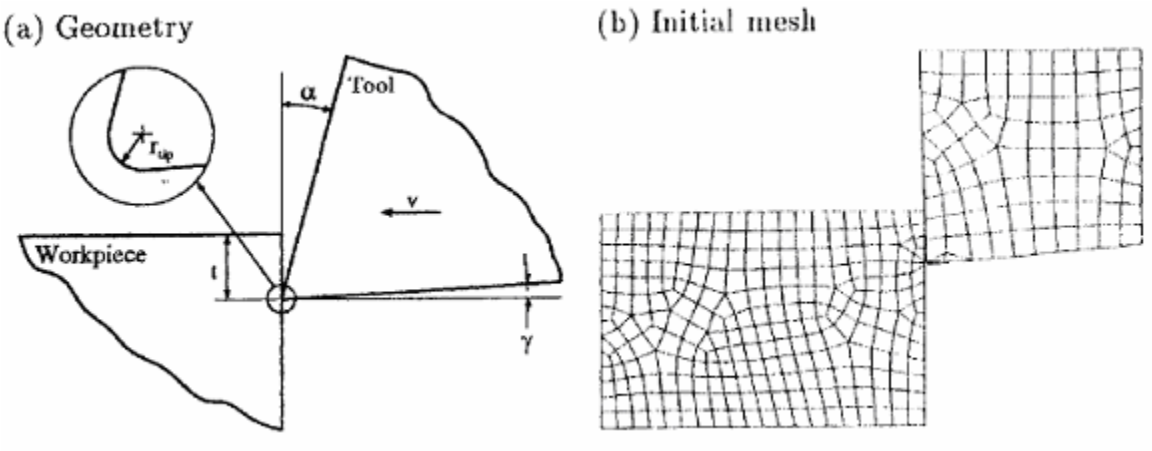

Fig. 2.14 Initial geometry and workpiece-tool mesh used in finite element simulation of orthogonal machining of Ti 6Al-4V alloy [23]

the cutting speed (from 5 to 20 m/s) and rake angle (from -9° to 9°) and to assess the capacity of the remeshing procedure to describe the process evolution. They assumed fracture strain as the governing parameter of material failure in high-speed machining and assessed two indicators of failure, namely, equivalent plastic strain and a fracture strain based on Lemaitre's damage model. The chip breakage process for a fracture strain based on the equivalent plastic strain was illustrated in Fig 2.15 which shows the elements undergoing a failure softening and fracture propagation. This criterion assumes that fracture initiates when effective plastic strain is equal to failure strain which is greater than or equal to 1.0.

However, from the Fig.2.15, it can be observed that only onset of chip segmentation process is shown in this investigation and it does not represent the exact physical phenomenon and mechanism of chip segmentation.

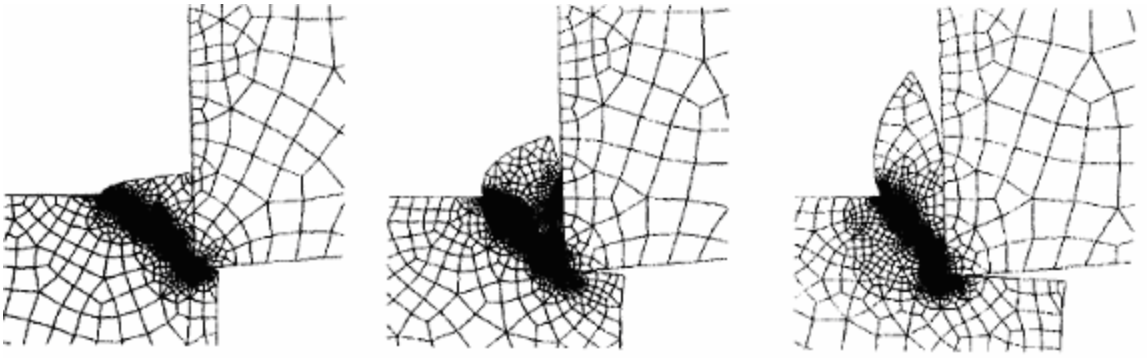

(a) (b) (c)

Fig. 2.15 Segmented chip formation process in machining simulation of a Ti 6Al-4V alloy at 10 m/s cutting speed and 0.5 mm feed using a -3° rake angle tool [23]

Baker *et al.* [35] developed a two-dimensional finite element model to simulate high-speed machining of Ti 6Al-4V using the commercial software, ABAQUS, together with a special mesh generator programmed in C++. In ABAQUS, they used standard program system, which allows the definition of complex contact conditions, leaves many possibilities to define material behavior, and can be customized in many regards by including user-defined subroutines. Preprocessor they used for automatic remeshing was written in C++ using standard class libraries to ensure that elements never become too distorted and refined mesh is created in the shear zone. They assumed that chip segmentation is caused solely by adiabatic shear band formation and that no material failure or cracking occurs in the shear zone. They used four-noded quadrilateral elements which converge better than triangular elements. The number of elements they used in the simulations varied with the number of segments. About 5000 elements and 7000 nodes were used at the beginning of the simulation and 10000 elements and 12000 nodes near

the end. The element edge was about 7 μm in the shear zone and Fig. 2.16 shows the finite element meshes at different stages of the cutting process with segmented chip formation.

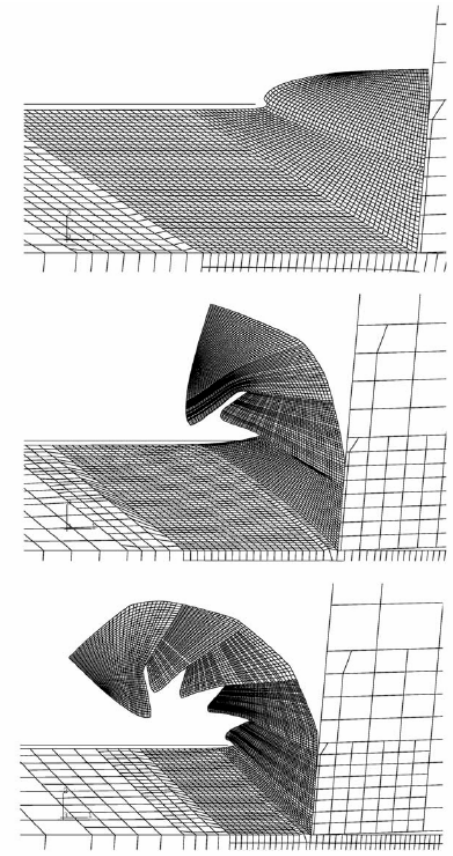

Fig. 2.16 Segmented chip formation process in finite element simulation of orthogonal metal cutting of a Ti 6Al-4V alloy at 50 m/s cutting speed and 0.04 mm cutting depth using a 10° rake angle tool [35]

Baker *et al.* [35] also investigated the influence of the elastic modulus and cutting speed on chip segmentation. They reported that elastic modulus affects the degree of segmentation. They also studied the influence of thermal conductivity on chip segmentation and showed that the degree of segmentation decreases with increasing thermal conductivity.

In this investigation, Baker *et al.* [35] used a pure deformation process to simulate metal cutting process without node separation. The material that overlaps with the tool as

the tool advances is removed using remeshing technique. This phenomenon however does not represent actual physical process of chip formation in machining. They also mentioned that they have found the strain-hardening part of plastic flow curves experimentally and determined the thermal softening part arbitrarily to facilitate the adiabatic shear bands formation which is unrealistic. In their simulations, it can be observed that high speeds are used, no friction is assumed between tool and the workpiece and heat flow into the tool is neglected. Also, Fig.2.16 does not represent actual mechanism of chip segmentation.

Sandstrom and Hodowany [36] modeled the high-speed orthogonal machining of Ti 6Al-4V using the commercial FEM code, Mach2D™ at a cutting speed of 10.16 m/s. Simulation results included chip segmentation, dynamic cutting forces, unconstrained plastic flow of material during chip formation, and thermo-mechanical environments of the workpiece and the cutting tool. They reported good agreement of the simulated cutting force to the experimental data. However, it can be observed that their investigation lack low speed simulations.

Shivpuri *et al.* [21] used a commercial finite element software (DEFORM 2D™) which is a lagrangian implicit code designed for metal forming processes, to simulate the orthogonal machining of Ti 6Al-4V. They modeled workpiece as a rigid-visco-plastic material owing to large plastic deformations taking place in the primary and the secondary deformation zones during the machining process. Furthermore, high mesh density was defined around the tool tip and excessively deformed workpiece mesh was automatically remeshed as needed during simulation. They modeled the tool as rigid (or elastic) material so that stresses in the tool body can be predicted. Dynamic flow stress

model was used to represent material behavior dependence on strain, strain rate, and temperature. Ductile fracture criterion was used to simulate crack initiation and propagation for chip segmentation. Simulations were conducted at cutting speeds of 1.2, 120 and 600 m/min and a feed rate of 0.127 mm/rev. Fig.2.17 shows the plastic strain distribution that presents the initiation of shear plane and the formation of shear zone. Based on simulations, they proposed that chip segmentation during cutting Ti 6Al-4V alloy is caused by flow localization within the primary deformation zone and upsetting

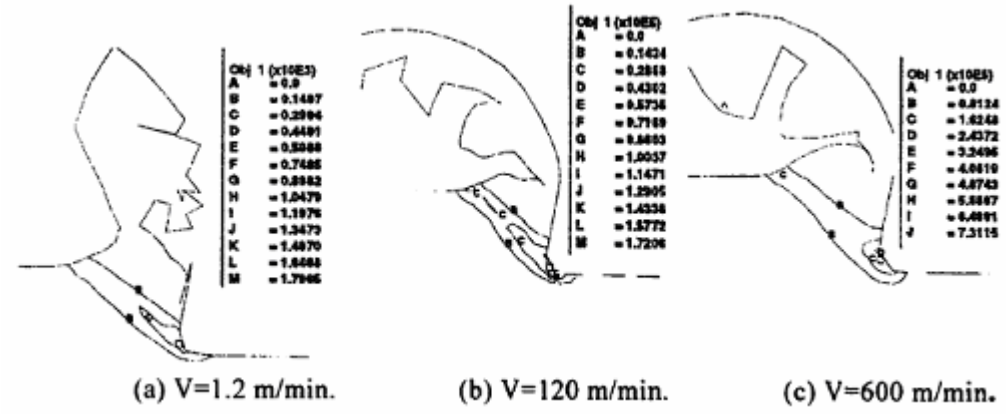

Fig. 2.17 Equivalent plastic strain distribution in serrated chip simulated at cutting speeds of 1.2, 120 and 600 m/min in a Ti 6Al-4V alloy [21]

deformation zone by moving tool rake face on the segment to be formed ahead of it. The flow localization induces fracture that separates segment from the workpiece matrix. Flow localization causes crack in the primary deformation zone while the secondary deformation zone controls the chip morphology (segmented or discontinuous). Discontinuous chip was formed at low speed (1.2 m/min) and segmented chips at higher cutting speeds (120 and 600m/min). At low cutting speeds, crack was observed to initiate

at the tool tip and propagates to the free surface of the chip while at higher cutting speeds, crack propagates from free surface towards the tool tip.

In their investigation, Shivpuri *et al.* [21] used maximum tensile stress criterion for ductile fracture to simulate serrated chip formation while maximum shear stress criterion accurately models serrated chip formation. Also, it can be observed from Fig.2.17, that chip morphology does not look like a serrated chip.

Although most of the researchers reported that their simulation results were in good agreement with the corresponding experimental data and their material model accurately predicts material deformation behavior in simulations, there is no consensus on which criterion represents the best for shear-localized chip formation in orthogonal metal cutting simulation of Ti 6Al-4V alloy.

Some of the major drawbacks of the finite element simulations of shear-localized chip formation in Ti 6Al-4V alloy found in the literature include:

1) The methodology proposed by many researchers using non-commercial FEM codes makes it difficult for end users.
2) Few researchers used extensive computer time and engineering effort, which makes their technique not economical to use.
3) The lack of reliable material data under specific process conditions such as, strain, strain rate and temperature that must be used as inputs to any material flow simulation program results in difficulty in applying to practical processes.
4) Most of the finite element simulations of Ti 6Al-4V alloy, lack proper experimental validations (especially chip morphology).
5) Lack of low speed machining simulations (< 10 m/min).

CHAPTER 3

FINITE ELEMENT FORMULATION OF METAL CUTTING

3.1 Introduction

Improvements in manufacturing processes require better modeling and simulation techniques of metal cutting. The process involves very complicated mechanisms such as interfacial frictional behavior, extremely high temperatures, complex stress state between tool chip interface, high strain rates, different types of chip formation, work hardening and thermal softening. Unfortunately, these complicated mechanisms associated have limited the performance of cutting process modeling and in recent years researchers in the metal cutting field are paying more and more attention to the finite element method due to its capability of numerically modeling different metal cutting problems. The advantages of using finite element method to study machining can be summarized as follows:

1) Material properties can be handled as a function of strain, strain rate, and temperature.
2) The tool-chip interaction can be modeled as sticking and sliding.
3) Non-linear geometric boundaries can be represented and used, such as free surface of chip.

Although the ideas of finite element analysis may date back much further, it was after further treatment of plane elasticity problem by Clough in 1960, that researches began to recognize the efficacy of finite element method in the engineering field. The advent and continuous improvements of digital computers have made finite element analysis a useful analytical tool which has been applied very efficiently in almost every area of engineering field. One of the most important reasons that finite element analysis is so widely used is that it can be routinely used. There are a definite set of several basic and distinct steps used in the FEM simulations:

1) Discretization of the continuum.
2) Selection of the interpolation function.
3) Determination of the element properties.
4) Assembly of the element properties in order to obtain the system equations.
5) Determination of the constraints and other boundary conditions.
6) Solution of the system equations.
7) Computation of the derived variables.

Inspite of the success of the finite element method in solving a very large number of complex problems, there are still many areas where more work needs to be done. Some examples are the handling of problems involving material failures and the modeling of nonlinear material behavior.

3.2 Finite Element Formulation

The basic idea of using the finite element method is to seek a solution to the momentum equation [37]:

$$\sigma_{ij,j} + b_i = \rho \dot{v}_i \qquad (i, j = 1,2,3), \tag{3.1}$$

where $\sigma_{ij,j}$ is the Cauchy stress tensor, ρ is the current mass density, b_i is the body force, v_i is the particle velocity in Cartesian coordinates, $\dot{v}_i$ is the acceleration, and j indicates partial differentiation with respect to x_j. Equation 3.1 satisfies the trajectory boundary condition:

$$\sigma_{ij}\, n_j = T_i \tag{3.2}$$

where n_j is the unit normal to the boundary and T_i is the surface traction on the plane with a unit normal n_j.

In this study, displacement based finite element method, which is the most widely used formulation in engineering among many finite element analysis techniques available, is applied to model the machining process. The displacement boundary condition that Equation 3.1 should satisfy at time t is given by:

$$u_i(t) = \overline{u_i} \tag{3.3}$$

For elastic-plastic deformations, the strain rate tensor is usually decomposed into elastic and plastic parts such that

$$\dot{\varepsilon}_{ij} = \frac{1}{2}\left(v_{i,j} + v_{j,i}\right), \qquad \dot{\varepsilon}_{ij} = \dot{\varepsilon}^{e}{}_{ij} + \dot{\varepsilon}^{p}{}_{i} \tag{3.4}$$

From Hook's law, we have

$$\dot{\varepsilon}^{e}{}_{ij} = C^{e-1}{}_{ijkl}\, \overset{o}{\sigma}_{kl} \;; \qquad C^{e}{}_{ijkl} = 2G\delta_{ik}\delta_{jl} + \frac{2G\nu}{1-2\nu}\delta_{ij}\delta_{kl} \tag{3.5}$$

where, C^{e}_{ijkl} is the elasticity tensor, G and ν are the shear modulus and poisons ratio, respectively, and $\overset{o}{\sigma}_{ij}$ is the corotational strain given by

$$\overset{o}{\sigma}_{ij} = \dot{\sigma}_{ij} - \sigma_{ik}\omega_{jk} + \sigma_{ij}\omega_{ik} \tag{3.6}$$

with α_{ik} being the material spin.

Using the von Mises flow rule, $\dot{\varepsilon}^{p}_{ij}$ is obtained as

$$\dot{\varepsilon}^{p}_{ij} = \frac{\bar{\gamma}}{2\bar{\tau}} s_{ij} \tag{3.7}$$

where s_{ij} is the deviatoric stress, $\bar{\dot{\gamma}} = \left(2\dot{\varepsilon}^{p}_{ij}\dot{\varepsilon}^{p}_{ij} \right)^{\frac{1}{2}}$ is the effective strain rate and $\bar{\tau} = \left(\frac{1}{2} s_{ij} s_{ij}\right)^{\frac{1}{2}}$ is the effective shear stress. The effective strain rate in Equation 3.7 is determined from the yield criterion of the rate-independent materials. For von Mises materials, yield criterion is given by

$$f_y = \sqrt{J_2} - \bar{\tau}\left(\bar{\gamma}\right) = 0\,, \tag{3.8}$$

where J_2 is the second invariant of $s_{ij,}$ from the consistency condition one can obtain the relation

$$\bar{\dot{\gamma}} = \frac{\overset{o}{s}_{ij}\, s_{ij}}{2\sqrt{J_2}h},\ h = \frac{\partial \bar{\tau}}{\partial \bar{\gamma}}, \tag{3.9}$$

where h is the hardening/softening modulus. Combining Equations 3.2 to 3.5, 3.7 and 3.9 we obtain,

$$\overset{o}{\sigma}_{ij} = C_{ijkl}\,\dot{\varepsilon}_{ij}\,, \tag{3.10}$$

where C_{ijkl} is the elastic-plastic incremental tensor and is given by

$$C_{ijkl} = C^{e}{}_{ijkl} - C^{p}{}_{ijkl}\,, \qquad C^{p}{}_{ijkl} = \frac{G^2}{\bar{\tau}^2\left(G+h\right)} s_{ij} s_{kl} \tag{3.11}$$

For rate-dependent materials, Equations 3.4 and 3.5 yield

$$\overset{o}{\sigma}_{ij} = C^{e}{}_{ijkl}\left(\dot{\varepsilon}_{kl} - \frac{\dot{\bar{\gamma}}}{2\bar{\tau}} s_{kl} \right) \tag{3.12}$$

These equations are implemented in all finite element programs. The solutions of engineering problems require the application of three conditions:

1) Equilibrium of forces.
2) Compatibility of deformations.
3) Constitutive relationship (material behavior).

These three conditions are used to generate the system of equations with stresses or displacements as unknowns. The former approach is called the force method and latter approach is called the displacement method. In general among many finite element techniques available displacement-based finite element method is most widely used formulation in engineering. The displacement method generates finite element equations of the form [38]:

$$[K]\{u\}^{(e)} = \{F\} \tag{3.13}$$

where [K] is the global stiffness matrix, {F} is the vector of all applied loads (known variables), and $\{u\}^{(e)}$ is the nodal displacement vector (unknown variables). It should be noted that applied load is not necessarily the force; it may be stress, displacement rate, etc. Solving the above equation yields the nodal displacement vector $\{u\}^{(e)}$. Then, the element strains {ε} can be determined by the strain-displacement relationship and stress {σ} can be calculated from the constitutive relationship [38] as:

$$\begin{aligned} \{\varepsilon\} &= [B]\{u\}^{(e)} \\ \{\sigma\} &= [M][B]\{u\}^{(e)} = [S]\{u\}^{(e)} \end{aligned} \tag{3.14}$$

where [B] is the strain-displacement matrix which usually has all constants, [M] is the material property matrix, and [S] = [M][B] is usually called the element stress matrix. The following coupled system of ordinary differential equations are used:

$$[M]\{\ddot{u}\} + \{F_{\text{int}}(u, \dot{u}, T)\} = \{P(u, b, t, T)\} \tag{3.15}$$

where $\{F_{int}\}$ is the internal nodal force vector and $\{P\}$ is the external nodal force vector which can be a function of nodal displacement u, body force per unit volume b, time t and nodal temperature T. The element stiffness $[K]^{(e)}$ can be calculated as:

$$[K]^{(e)} = \int_{D^e} \left([B]^{(e)}\right)^T [M]^{(e)} [B]^{(e)} dD^e \tag{3.16}$$

where $[B]^{(e)}$ is the strain-displacement matrix, $[M]^{(e)}$ is the material matrix and D^e is the element volume. The element contribution to the internal nodal force vector $\{F_{int}\}^{(e)}$ can be obtained as:

$$\{F_{\text{int}}\}^{(e)} = \int_{D^e} \left([B]^{(e)}\right)^T \{\tau_i\} dD \tag{3.17}$$

Then the global stiffness matrix [K] and internal load vector $\{F_{int}\}$ can be constructed as:

$$\begin{aligned} [K] &= \sum_e [K]^{(e)} \\ \{F_{\text{int}}\} &= \sum_e \{F_{\text{int}}\}^{(e)} \end{aligned} \tag{3.18}$$

It is necessary to point out that for metal cutting simulations, the matrices $[B]^{(e)}$ and $[M]^{(e)}$ are no longer constant as metal cutting analysis is a non-linear, large deformation analysis. Therefore $[B]^{(e)}$ and $[M]^{(e)}$ need to be evaluated at each step of the finite element calculation.

For quasi-static analysis of metal cutting process, the finite element equations (Equation 3.13) are simplified by eliminating the inertial effects, and thus have the form:

$$\left\{F_{\text{int}}\left(u,\dot{u},T\right)\right\} = \{P(u,b,t,T)\} \tag{3.19}$$

To obtain the solution at time step t_{n+1}, the finite element equations are first linearized about the configuration at t_n as:

$$[K]_n \{\Delta u\}^0 = \{P\}_{n+1} - \{F_{\text{int}}\}_n \tag{3.20}$$

where $[K]_n$ is the stiffness matrix based on the configuration at t_n and $\{\Delta u\}^\circ$ is the increment in displacement where the superscript denotes iteration number. $\{\Delta u\}^\circ$ can be solved from Equation 3.20 and displacement is updated by:

$$\{u\}_{n+1} = \{u\}_n + s^0 \{\Delta u\}^0 \tag{3.21}$$

where s° is a parameter between 0 and 1 which is determined by line search scheme. Finally, the equilibrium iterations can be performed by solving the following equations:

$$[K]^i \{\Delta\}^i = \{P\}_{n+1} - \{F_{\text{int}}\}^i{}_{n+1} = \{Q\}^i{}_{n+1} \tag{3.22}$$

where $\{Q\}^i{}_{n+1}$ is the residual. And the convergence is determined by examining both the displacement norm

$$\frac{\left\|\{\Delta u\}^i\right\|}{u_{\max}} \le \varepsilon_d , \tag{3.23}$$

and energy norm:

$$\frac{\left(\{\Delta u\}^i\right)^T \{Q\}^i{}_{n+1}}{\left(\{\Delta u\}^0\right)^T \{Q\}^0{}_{n+1}} \le \varepsilon_e , \tag{3.24}$$

In the Equations 3.23 and 3.24, u_{max} is the maximum displacement norm above all of the n steps including the current iteration, ε_d and ε_e are the tolerances that are typically 10^{-2} to

10^{-3} or smaller and are usually adjustable for different problems. If the convergence is not attained and solution is divergent, the solution is obtained by:

$$\{u\}^i_{n+1} = \{u\}^i_{n+1} + s^i \{\Delta u\}^i \tag{3.25}$$

where s^i is the parameter same as s° at the i^{th} iteration. Iterations will then continue and if the solutions are determined to be divergent, or convergence fails to occur within an assigned number of iterations the stiffness matrix is [*K*] is reformed using the current estimation of the geometry before continuing the equilibrium iteration.

The commercial software AdvantEdge™ is used in this study to simulate the metal cutting process. The finite element formulation used in this software is a Lagrangian formulation. The central difference rule is used to integrate the equations of motion. AdvantEdge™ uses a lumped mass formulation for efficiency, which produces a diagonal mass matrix that renders the solution of the conservation of the momentum equation given by [37]:

$$\sigma_{ij,j} + \rho b_i = \rho \ddot{u}_i \tag{3.26}$$

This equation shows the inertial forces and internal forces, due to the current state of stress, are in balance with the applied boundary loads. The weak form of the above equation based on the principle of virtual work becomes:

$$\int_B v_i \sigma_{ij,j} + v_i \rho b_i dV = \int_B \rho v_i \ddot{u}_i \, dV \tag{3.27}$$

solving and rearranging the above equation gives:

$$\int_B \rho v_i \ddot{u}_i \, dV + \int_B v_{i,j} \sigma_{ij} dV = \int_{\partial B} v_i \sigma_{ij} n_j d\Omega + \int_B v_i \rho b_i dV \tag{3.28}$$

Finite element discretization of the above equation provides:

$$\int_B \rho N_a N_b \ddot{u}_{ib}\, dV + \int_B N_{a,j}\sigma_{ij} dV = \int_{\partial B} N_a \tau_i d\Omega + \int_B \rho N_a b_i dV \tag{3.29}$$

It can be represented in matrix form as:

$$Ma_{n+1} + R_{n+1}^{\text{int}} = R_{n+1}^{ext} \tag{3.30}$$

where

$$M_{ab} = \int_{B_0} \rho_0 N_a N_b dV_0 \tag{3.31}$$

is the mass matrix and

$$R_{ia}^{ext} = \int_{B_0} b_i N_a dV_0 + \int_{\partial B_0} \tau_i N_a d\Omega_0 \tag{3.32}$$

is external force array and

$$R_{ia}^{\text{int}} = \int_{B_0} P_{ij} N_{a,j} dV_0 \tag{3.33}$$

is the internal force array. In the above expressions, $N_{a,}$ *a=1,….,numnp* are the shape functions, repeated indices imply summation and *a* (,) represents partial differentiation with respect to the corresponding spatial coordinate, and P_{ij} is the first Piola-Kirchoff stress tensor analogous to nominal or engineering stress. Using the Newmark family of algorithms for temporal integration of the discretized weak form, second order accurate explicit analysis can be achieved through the central difference scheme. Since plasticity results in softening of stiffness matrix, it suffices to look to the bounding case of linear elasticity, for which the generalized eigen problem is given by:

$$\left(K_{ij} - \lambda^l M_{ij}\right) d_j^{\,l} = 0 \tag{3.34}$$

Accurate computation of the system eigen values is essential due to changes in mesh geometry (eigen values) arising from deformation. Since the largest system eigen value is

bounded by the largest element eigen value, it suffices to compute the largest eigen value of each element to determine the critical time step for the mesh. Heat generation and transfer are handled via the Second Law of Thermodynamics. A discretized weak form of the law is given by:

$$T_{n+1} = T_n + \Delta t \dot{T}_n \tag{3.35}$$

$$C T_{n+1} + \dot{K} T_{n+1} = Q_{n+1} \tag{3.36}$$

A lumped capacitance matrix is used to eliminate the need for solving any equations.

$$C \dot{T} + KT = Q \tag{3.37}$$

where T is the array of nodal temperatures.

$$C_{ab} = \int_{B_t} c\rho N_a N_b dV_0 \tag{3.38}$$

is the heat capacity matrix and

$$K_{ab} = \int_{B_0} D_{ij} N_{a,i} N_{b,j} dV \tag{3.39}$$

is the conductivity matrix and

$$Q_a = \int_{B_t} s N_a dV + \int_{B\pi q} h N_a dS \tag{3.40}$$

is the heat source array with h, having an appropriate value for the chip or tool. In machining applications, the main sources of heat are plastic deformation in the shear zone and frictional sliding in the tool-workpiece interface. The rate of heat supply due to the first is estimated as:

$$s = \beta \dot{W}^P \tag{3.41}$$

where $\dot{W}^{P}$ is the plastic power per unit deformed volume and Taylor-Quinney coefficient β is of the order of 0.9. The rate at which the heat generated at the frictional contact, on the other hand is given by:

$$h = -t \cdot \|v\| \tag{3.42}$$

where t is the contact traction and $\|v\|$ is the jump in velocity across the contact.

A staggered procedure is adopted to couple mechanical and thermal equations. Geometrically identical meshes for the mechanical and thermal models are used. Mechanical and thermal computations are staggered assuming constant temperature during the mechanical step and constant heat generation during the thermal step. A mechanical step is taken first based on current distribution of temperatures, and the heat generated is computed from plastic working and frictional heat generation. The heat thus computed is transferred to the thermal mesh and the temperatures are recomputed by recourse to the forward-Euler algorithm. The resulting temperatures are transferred to the mechanical mesh and are incorporated into the thermal-softening model which completes one time step cycle.

3.3 Friction formulation along tool-chip interface

Friction along the tool-chip contact during the cutting process is a very complex phenomenon. Friction influences chip formation, built-up edge formation, cutting temperature and tool wear. Therefore it is necessary to understand the friction mechanism across the tool face and around the edge of the tool, in order to develop accurate models

for cutting forces and temperature. In the AdvantEdge™ software, the friction model incorporated is coulomb friction model and it is represented by:

$$\tau = \mu\sigma \tag{3.43}$$

where τ is the frictional shear stress and σ is the normal stress to the surface. Usually the friction coefficient μ is assumed to be constant for a given interface. In the metal cutting, the cutting pressure at the tool-chip interface will become several times the yield stress of the workpiece material. In this extreme case, the real contact between the tool and workpiece is so nearly complete in the sticking region that sliding occurs only beyond this region. Therefore the frictional force becomes that required to shear the weaker of the two materials across the whole interface. This force is almost independent of the normal force, but is directly proportional to the apparent area of contact.

3.4 Formulation of Contact Conditions

In metal cutting simulations, mesh-on-mesh contact occurs between the workpiece and the tool and this contact is formulated in AdvantEdge™ software using predictor-corrector method of PRONTO2D™ explicit dynamics code. The two contacting surfaces are designated as master and slave surfaces (Fig. 3.1). Assuming that no contact has occurred, nodal accelerations from the out-of-balance forces are calculated and nodal positions, velocities, and accelerations are predicted by predictor algorithm. A resulting predictor configuration shows penetration of the master surface into the slave surface. The contact conditions are designated by an auxiliary consecutive numbering of the nodes on the contacting surfaces. The penetration distances for all nodes on the slave surface are then calculated. The contact force required to prevent penetration is equal to

the force required to keep the master surface remain stationary on predictor configuration. Tangential force exerted by the master surface on the slave node cannot exceed the maximum frictional resistance. This condition should be satisfied to prevent unwanted penetration. A balanced master-slave approach in which surfaces alternately act as master and slave is also employed; however, rigid surfaces are always treated as master surfaces.

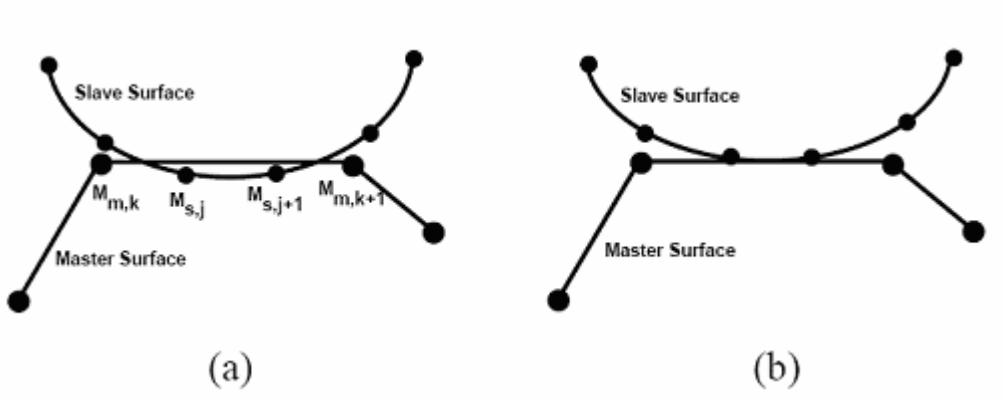

Fig. 3.1 Contacting surfaces in a mesh showing (a) predictor configuration and (b) kinematically compatible configuration [14]

3.5 Adaptive remeshing

In AdvantEdge™ finite element formulation incorporates a six-noded quadratic triangular element with three corner and three midside nodes providing quadratic interpolation of displacements within the element as shown in Fig. 3.2. The element is integrated with three-point quadrature interior to the element. At the integration points, the constitutive response of the material is computed and consequently linear pressure distribution is provided within the element.

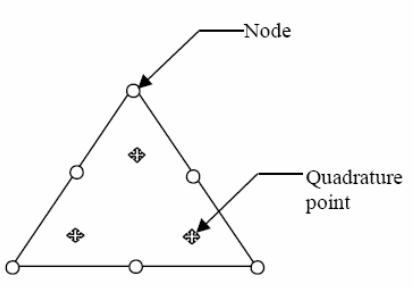

Fig. 3.2 Six-nodes and three quadrature points shown in a typical six-noded triangular element used in the finite element mesh of the workpiece and tool [14]

During metal cutting, workpiece material flows around the cutting tool edge. In this process, at the tool vicinity elements get distorted and the accuracy is lost. To alleviate element distortion, finite element mesh is updated periodically, refining large elements, remeshing distorted elements and coarsening smaller elements. For instance, if an element needs refinement, the diagonal of the element is split, a midside node becomes new corner node and new midside nodes are added to both elements as shown in Fig.3.3.

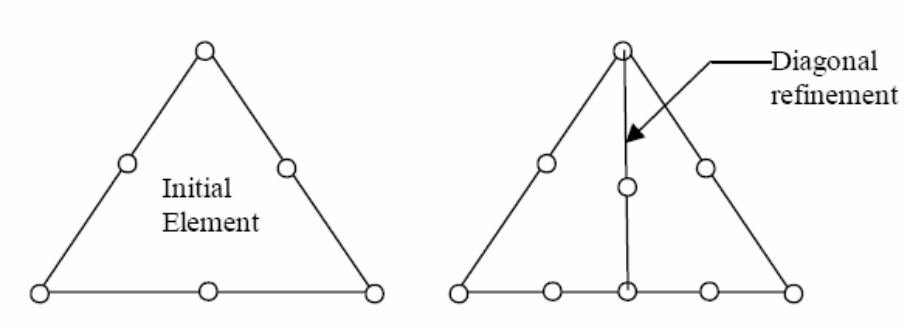

Fig. 3.3 Element shape in a finite element mesh (a) before and (b) after adaptive remeshing [14]

For adaptive remeshing, an adaptation criterion based on the equidistribution of plastic power is used. In this approach, elements with plastic power content exceeding a

prescribed tolerance TOL, are targeted for refinement. The criterion can be represented as [14]:

$$\int_{\Omega_h^e} \dot{W}^p d\Omega > TOL \tag{3.44}$$

here Ω_h^e denotes the domain of the element e and the plastic power for an element is given by

$$\dot{W}^p = \bar{c}\,\dot{\varepsilon}^p \tag{3.45}$$

if, despite this continuous remeshing, elements arise with unacceptable aspect ratios, the mesh is subjected to Laplacian smoothing. Besides sidestepping the problem of element distortion, adaptive remeshing provides a means of simultaneously resolving multiple scales in the solution. Transport of data, such as displacement and temperature from old mesh to new mesh after remeshing is done by interpolation technique.

3.6 Chip formation

Different numerical techniques for modeling chip separation exist and they can be divided into two categories- geometrical and physical. The geometrical model is usually based on the tied slide-line interface which debonds when certain criterion is fulfilled. This criterion may be a certain level of stress, strain or simply when the cutting edge is close enough to the front nodes. On the other hand, physical model is based on the physical behavior of the material, such as plastic deformation, crack initiation and crack propagation without pre-determining its path.

AdvantEdge™ simulation software uses critical stress intensity factor, K_{IC}, as a fracture criterion for brittle materials and crack tip opening displacement (CTOD) for ductile fracture. Brittle fracture, such as the one that occurs below the transition temperature, proceeds by cleavage. In particular, conditions for brittle fracture are found to be consistent with the attainment of a critical opening stress σ_f at a critical distance l.

The critical stress σ_f is found to be relatively independent of temperature and strain rate and can be inferred from the toughness K_{IC} through the small scale yielding relation [14]

$$\sigma_f = \frac{K_{IC}}{\sqrt{2\pi l}} \tag{3.46}$$

The crack trajectory under conditions of brittle fracture is predicted using maximum hoop stress criterion according to which crack propagates along the angle θ from the crack face at which the hoop stress $\sigma_{\theta\theta}$ attains a relative maximum. Void growth and coalescence are known to be principal mechanisms of ductile fracture. The rate of growth of voids is accelerated by the blunting of the crack tip, which has the effect of raising the hydrostatic stress at the location of the void. The crack tip opening displacement (CTOD) criterion for ductile fracture can be recast as the attainment of critical effective plastic strain ε^p_f of the effective plastic strain at a distance l ahead of the crack tip [14]. The criterion can be represented as:

$$\max_{\theta} \varepsilon^p(l,\theta) = \varepsilon^p_f \tag{3.47}$$

where θ is the angle at which the crack propagates when the criterion is met. The critical effective plastic strain (ε^p_f) can be estimated as

$$\varepsilon^p_f \approx 2.48 e^{-1.5\frac{p}{\bar{\sigma}}} \tag{3.48}$$

where $p = \sigma_{kk}/3$ is the hydrostatic pressure.

CHAPTER 4

PROBLEM STATEMENT

As mentioned in the literature review, many researchers in the past have developed analytical models to explain the theory of chip segmentation. Many theories based on adiabatic shear failure, damage model and crack initiation and propagation have been proposed for segmented chip formation in Ti 6Al-4V. But most of the models suffer from a lack of adequate acceptable methodologies for application under a wide range of cutting conditions. In addition, very little work has been done on finite element simulations of machining Ti6Al-4V alloy (especially at very low speeds). Most of these simulations have limited experimental validation under few selected cutting conditions and tool geometries. This is an area deserving more study because a reliable finite element model of chip segmentation needs a realistic material model to describe material behavior accurately under high temperatures, high strains, and high strain rates and a proper failure criterion to represent the mechanism of chip segmentation.

Thus an attempt has been made in this study to deal with the above mentioned aspects. The specific objectives of this study are:

1) To study the mechanism of chip formation in machining Ti 6Al-4V using finite element simulations.

2) To formulate a reliable material model, such as the Johnson-Cook model into the user defined material code (UMAT) so that it can represent material flow stress with respect to strain, strain rate, and temperature at different machining conditions.
3) To derive equations for Recht's catastrophic shear failure criterion and incorporate it into UMAT code as a failure criterion for shear-localized chip formation in Ti 6Al-4V.
4) To validate the finite element simulations with experimental results obtained from the literature by comparing the cutting forces, rake face temperature and chip morphology.
5) To predict the critical cutting speed for the onset of chip segmentation.
6) To conduct finite element simulations using commercial finite element software, AdvantEdge™.
7) To study the effect of different machining conditions, such as cutting speed, feed, rake angle and coefficient of friction on cutting forces, rake face temperature, shear zone temperature, equivalent plastic strain, frequency of chip segmentation, shear band width, and power consumption.

CHAPTER 5

SHEAR LOCALIZATION IN Ti 6Al-4V MACHINING

5.1 Shear-Localized Chip in Ti 6Al-4V

Titanium alloys are one of the most attractive materials because of their high specific strength maintained at high temperatures, excellent fracture resistance and corrosion resistance. They are much sought after materials for aerospace applications. Although Ti 6Al-4V comprises about 45% to 60% of titanium products in practical use, it is considered as difficult-to-machine material because of its unfavorable thermal properties. Generally, two types of chip formation are observed in machining Ti 6Al-4V based on the cutting speed. They are the continuous chip and the segmented chip. Segmented chip is also called shear-localized chip because of intense plastic deformation in the narrow band between the chip segments and negligible deformation within the segment. According to Komanduri and Hou [25], for titanium alloys shear localization occurs even at very low cutting speeds (<0.5 m/min) and continues over the entire conventional cutting-speed range. Consequently, continuous chip can be observed only at very low speeds (below 0.5 m/min). The chips formed in Ti 6Al-4V machining looks like saw tooth with chip being inhomogeneous and shows two regions, shear band with very large shear strains between the chip segments and a trapezoidal shaped segments body

with relatively small deformation. Once the shear localization is initiated, the chip topside looks like saw tooth with each tooth corresponding to a segment.

Many researchers have done extensive studies on the mechanism of chip formation when machining titanium alloys since the early 1950s using several techniques, such as high-speed photography, in-situ machining inside a scanning electron microscope and metallurgical analysis of chips generated in machining. Based on these studies many models were formulated to describe the mechanism of segmented chip formation in titanium alloys. In this study, Recht's thermoplastic shear instability criterion is used to simulate shear-localized chip formation.

5.2 Mechanism of Shear-Localized Chip formation

In machining Titanium alloys, the chips formed are segmented and strain is not uniformly distributed but is confined to narrow bands between the segments. Whereas, in the continuous chip formation, the deformation is largely uniform. The sequence of events leading to shear-localized chip formation in Ti 6Al-4V was described by Komanduri and Turkovich [11] based on the detailed chip formation studies of video tapes of low speeds experiments inside the scanning electron microscope, high-speed movie films at higher cutting speeds and the micrographs of midsection of chips. They observed the mechanism of chip formation to be invariant with respect to cutting speed. The mechanism of shear-localized chip formation can be explained based on the Fig. 5.1. The process can be divided into two basic stages. The first stage involves shear instability and strain localization in a narrow band in the primary shear zone ahead of the tool. This narrow band originates from the tool tip almost parallel to the cutting velocity vector and

gradually curves with the concave surface upwards until it meets the free surface. The shear failure of the chip appears as a crack on the outside while it is a heavily deformed band inside.

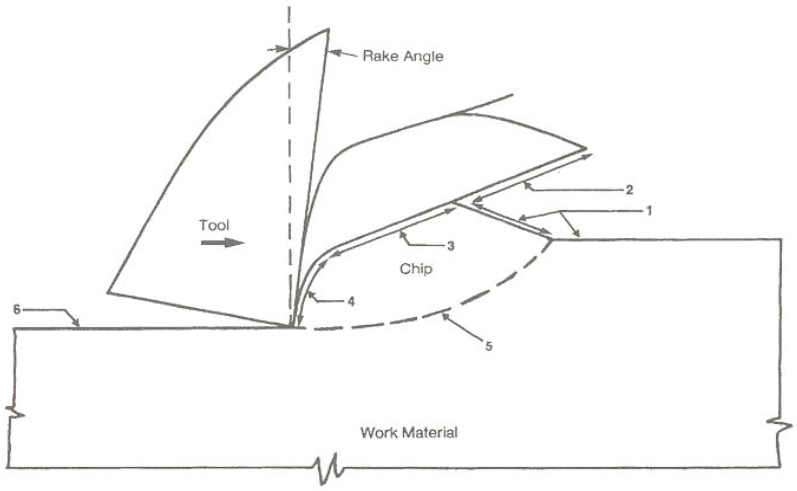

1. Undeformed surfaces
2. Part of the catastrophically shear failed surface separated from the following segment due tointense shear
3. Intense shear band formed due to catastrophic shear during upsetting stage of the segment being formed
4. Intensely sheared surface of a segment in contact with the tool and subsequent sliding on the tool face
5. Intense localized deformation in the primary shear zone
6. Machined surface

Fig. 5.1 Description of shear-localized chip formed due to adiabatic shear localization [26]

The second stage involves upsetting of an inclined wedge of work material by the advancing tool, with negligible deformation, forming a chip segment. During upsetting of the chip segment in the primary shear zone ahead of the tool tip, intense shear takes place at approximately 45° to the cutting direction. This occurs not between the tool face and chip but between the last segment formed and the one just forming. The initial contact of the tool face with the segment being formed is very less and it gradually increases as the upsetting progresses. There is almost no relative motion between the bottom surface of the chip segment being formed and the tool face until the end of the upsetting stage of the

segmentation process. The gradual upsetting process slowly pushes the segment formed previously upwards. The velocity of the chip along the rake face is same as the upsetting chip until the shear is initiated and progresses rapidly. Once this occurs, it pushes the chip segment being formed faster parallel to the shear surface. This will then push the previous segment formed rather rapidly. Thus the chip velocity along the rake face fluctuates cyclically. This mechanism of segmented chip formation occurs almost at all speeds. However, as the cutting speed increases, intense shear in the narrow shear band occurs so rapidly that contact area between any two segments decreases to a stage that individual segments of the chip get separated.

5.3 Criterion for Thermo Plastic Shear Instability

Recht in 1964 [12] developed a criterion for the prediction of catastrophic shear instability in metals under dynamic plastic conditions. Accordingly, shear-localized chip formation can be attributed to dynamic plastic behavior of the material which is influenced by internally generated temperature gradients. These gradients are function of thermo-physical properties of the workmaterial as well as strain rate and shear strength. Catastrophic shear will occur at a plastically deformed region within a material when the slope of the true stress-true strain curve becomes zero, i.e. when local rate of change of temperature has a negative effect on the strength which is equal to or greater than the positive effect of strain hardening. The criterion for catastrophic shear failure can be represented as:

$$0 \le \frac{\dfrac{\partial \tau}{\partial \varepsilon}}{\dfrac{-\partial \tau}{\partial \theta}\dfrac{d\theta}{d\varepsilon}} \le 1.0 \qquad (5.1)$$

where τ, ε, θ refer to shear stress, shear strain, and temperature, respectively. Accordingly, material will shear catastrophically when this ratio lies between zero and one; catastrophic shear will be imminent when this ratio equals one. No catastrophic shear will occur when this ratio is greater than one. High positive values above one indicate that strain hardening is predominant and shear deformation will distribute throughout the material, in which case material will strain harden more than it will thermal soften. Negative values indicate that material will actually become stronger with an increase in temperature and that shear deformation will distribute. Thus thermoplastic shear instability (frequently referred to as adiabatic shear) is a major contributor to chip segmentation. Just so long as material can withstand shear stress by virtue of its shear strength, it will remain thermoplastically stable. As stress increases, material strains and if rate of change of strength matches the rate of change of stress, material will undergo stable deformation. When instability occurs, the applied stress will be borne by the remaining (diminishing) strength of the material. And inertial reactions associated with, accelerate instability, leading to catastrophic shear failure. Recht thus provided the first explanation for segmented chip formation in machining. Since the fundamental contributions of Recht, much work has been done on the adiabatic shear band formation, often in connection with the applications, such as armor penetration and explosive fragmentation.

5.4 Metallurgical Aspects of Shear-Localized Chip Formation

In metal cutting, the temperatures generated in the primary and secondary deformation zones can be high enough to cause several changes in the workpiece material, such as thermal softening, phase transformation, and even grain shape and size changes. These changes to a certain extent can effect the prediction of optimal cutting conditions for a given machining operation. Adiabatic shear banding is a phenomenon observed in machining titanium alloys. The formation of shear-localized chip in titanium alloys is also accompanied by certain metallurgical changes. Komanduri [26] noted that during segmented chip formation in titanium alloys, there may be a transition from the low-temperature hexagonal close packed (HCP) structure to the body centered cubic (BCC) structure with a corresponding increase in the number of available slip systems. Accordingly, this phenomenon further localizes the shear strain. This transition in the crystal structure results primarily from the increase in temperature and this increase can cause further increase in plastic deformation.

Ti 6Al-4V is an alloy with α+β structure which consists of lamellar α structure and intergranular β structure. Bayoumi and Xie [39] conducted metallurgical studies using a scanning electron microscope (SEM) and an X-ray diffraction studies of both uncut and machined Ti6Al4V chips. Fig.5.2 shows X-ray diffraction spectra for Ti 6Al-4V alloy before and after cutting. They compared the spectrum of the chip with uncut material and found that the peaks corresponding to β-phase structure disappearing after cutting, indicating that a non-diffusional phase transformation took place in the process of shear band formation. When the temperature in the chip reaches the β-transus

temperature of Ti 6Al-4V (which is 980°C) during the cutting process and cools back from this high temperature, the temperature change along with tremendous cutting pressure would produce the lamellar α structure from β-phase by nucleation and growth. Accordingly, they concluded that there is only grain change during the phase transformation and no chemical change.

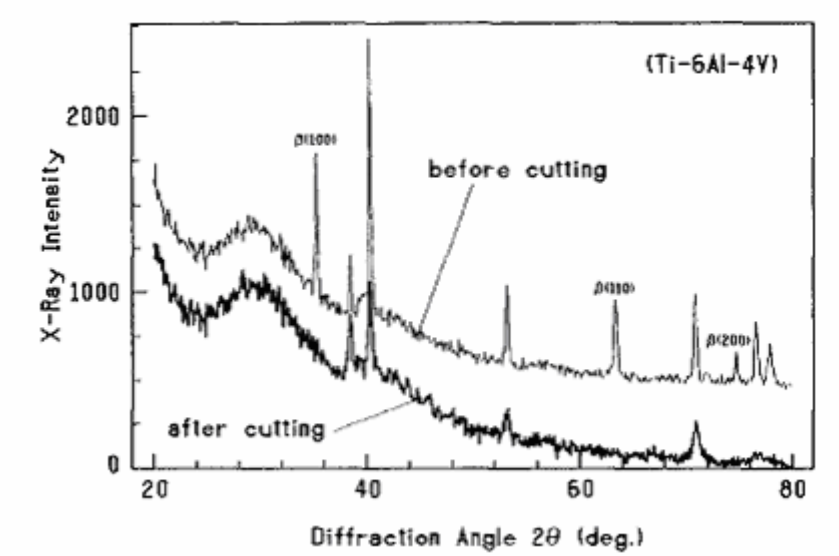

Fig. 5.2 X-ray diffraction spectra for chip and uncut material in a Ti 6A-l4V alloy [39]

From the microstructural examination of the chip and uncut Ti 6Al-4V, they concluded that as both are similar in appearance, the shear-localized chips may be caused by material flow in shear bands due to adiabatic shear instability.

CHAPTER 6

FEM SIMULATION OF CHIP SEGMENTATION IN Ti 6Al-4V

6 .1 Introduction

One of the state-of-art efforts in manufacturing engineering is the finite element simulation of the metal cutting process. These simulations would have great value in increasing our understanding of the metal cutting process and reducing the number of trial and error experiments, which traditionally was the approach used for tool design, process selection, machinability evaluations, chip formation and chip breakage investigations. Compared to empirical and analytical methods, finite element methods used in the analysis of chip formation has advantages in several respects, such as developing material models that can handle material properties as a function of strain, strain rate and temperature. The tool-chip interaction can be modeled as sticking and sliding; and non-linear geometric boundaries such as the free surface of the chip can be represented and used. In addition to the global variables, such as cutting force, thrust force and chip geometry; the local variables such as stress, temperature distributions, can also be obtained.

As mentioned in the literature review, very limited work has been done on FEM simulation of titanium alloys. Qualitative analysis of such simulations seems to suffer with lack of accurate material model to describe the material behavior of titanium alloys

under high temperature, high strain and high strain rates. Also, most of the simulations lack appropriate failure criterion to simulate shear-localized chip formation. Further, most of the simulations were performed for high-speed machining while in titanium alloys segmented chip is found to occur even at very low speeds. In this study, Johnson-Cook material model is used to represent material behavior as a function of strain, strain rate, and temperature; Recht's catastrophic shear failure criterion is used for chip segmentation and a commercial, general-purpose FE software, AdvantEdge is used to simulate orthogonal metal cutting of Ti 6Al-4V under various machining conditions.

AdvantEdge machining modeling software is a two-dimensional central difference explicit finite element code using a Lagrangian mesh. The material model of the software accounts for elastic-plastic strains, strain rates and temperature. It has an isotropic power law for strain hardening and as the material flow properties are temperature dependent it also accounts for thermal softening. A staggered method for coupled transient mechanical and heat transfer analyses is utilized. A six-node quadratic triangular element with three quadrature points is used. This software also features adaptive remeshing option to alleviate mesh distortion.

6.2 Material Constitutive Model

The flow stress or instantaneous yield strength at which work material starts to deform plastically is mostly influenced by temperature, strain, and strain rate. The constitutive model proposed by Johnson and Cook describes the flow stress of a material as a product of strain, strain rate, and temperature that are individually determined by the following equation:

$$\sigma = [A+B(\varepsilon)^n][1+C\ln(\dot{\varepsilon}^*)][1+(T^*)^m] \quad (6.1)$$

where σ is the effective stress, ε is the effective plastic strain, $\dot{\varepsilon}^*$ is the normalized effective plastic strain rate, n is the work hardening exponent, m is the thermal softening exponent and A, B, C and m are constants [9]. It may be noted that formulation of Johnson-Cook model is empirically based. The expression in the first set of brackets gives the stress as a function of strain for $\dot{\varepsilon}^*$ =1.0 and T^*=0.The expressions in the second and third sets of brackets represent the effects of strain rate and temperature, respectively. The parameter A is in fact the initial yield strength of the material at room temperature at a strain rate of 1 s^{-1}. The non-dimensional parameter T^* is defined as

$$T^* = (T- T_{room})/(T_{melt}- T_{room}) \quad (6.2)$$

where T is the current temperature, T_{room} is the ambient temperature, and T_{melt} is the melting temperature. Temperature term in this model reduces the flow stress to zero at the melting temperature of the workmaterial, leaving the constitutive model with no temperature effects. The non-dimensional normalized effective plastic strain rate $\dot{\varepsilon}^*$ is the ratio of the effective plastic strain rate $\dot{\varepsilon}^p$ to the reference strain rate $\dot{\varepsilon}^\circ$ (usually equal to 1.0). In general, the parameters A, B, C, n and m are fitted to the data obtained by several mechanical tests conducted at low strains and strain rates as well as split Hopkinson pressure bar (SHPB) tests and ballistic impact tests. Johnson-Cook model provides good fit for strain hardening behavior of the metals. It is numerically robust and can be easily used in finite element simulation models.

6.3 Formulation of Recht's Catastrophic Shear Failure Criterion

Perhaps the first criterion for shear localization was developed by Recht [12]. According to this criterion, shear instability was predicted to occur when the rate of strain hardening of the material is balanced by thermal softening. This indicates that when an increase in shear strain is associated with a decrease in shear stress, the strain hardening slope would become negative:

$$\frac{d\bar{\tau}}{d\bar{\gamma}} \le 0 \qquad \text{with} \quad \frac{d\bar{\tau}}{d\bar{\gamma}} = \frac{\partial\bar{\tau}}{\partial\bar{\gamma}} + \frac{\partial\bar{\tau}}{\partial T}\frac{dT}{d\bar{\gamma}} \tag{6.3}$$

The criterion R can be written as follows:

$$R = \frac{\dfrac{\partial\bar{\tau}}{\partial\bar{\gamma}}}{\dfrac{-\partial\bar{\tau}}{\partial T}\dfrac{dT}{d\bar{\gamma}}} \qquad \text{and} \qquad 0 \le R \le 1 \tag{6.4}$$

where $\bar{\tau}, \bar{\gamma}$ and T represent shear stress, shear strain and temperature respectively. When R is equal to zero, instability starts and when R is equal to one catastrophic shear failure occurs.

The numerator and denominator terms of R are derived from Johnson-Cook flow stress equation:

$$\bar{\sigma} = \left(A + B\left(\bar{\varepsilon}\right)^{n}\right)\left(1 + C\ln\frac{\dot{\bar{\varepsilon}}}{\dot{\varepsilon}^{o}}\right)\left(1 - \frac{T - T_r}{T_m - T_r}\right) \tag{6.5}$$

where A, B, C, n, m are constants. T is the current temperature, T_r is the ambient temperature, T_m is the melt temperature. $\bar{\varepsilon}$ is the strain, $\dot{\bar{\varepsilon}}$ is the effective plastic strain rate and $\dot{\varepsilon}^o$ is the reference plastic strain rate.

The shear stress $\bar{\tau}$ and the shear strain $\bar{\gamma}$ can be expressed in terms of strain and strain rate as follows:

$$\bar{\tau} = \frac{\bar{\sigma}}{\sqrt{3}} \qquad \text{and} \qquad \bar{\gamma} = \bar{\varepsilon}\sqrt{3} \tag{6.6}$$

Substituting the Equation 6.6 into Equation 6.5, we get

$$\bar{\tau} = \frac{1}{\sqrt{3}}\left[A + B\left(\frac{\bar{\gamma}}{\sqrt{3}}\right)^n\right]\left[1 + C\ln\left(\frac{\dot{\bar{\gamma}}}{\dot{\bar{\gamma}}_0}\right)\right]\left[1 - \left(\frac{T - T_r}{T_m - T_r}\right)\right] \tag{6.7}$$

The partial differentiation of Equation 6.7 with respect to the shear strain $\bar{\gamma}$ gives the strain hardening term $\frac{\partial \bar{\tau}}{\partial \bar{\gamma}}$ as

$$\frac{\partial \bar{\tau}}{\partial \bar{\gamma}} = \left[\frac{nB}{3}\left(\frac{\bar{\gamma}}{\sqrt{3}}\right)^{n-1}\right]\left[1 + C\ln\left(\frac{\dot{\bar{\gamma}}}{\dot{\bar{\gamma}}_0}\right)\right]\left[1 - \left(\frac{T - T_r}{T_m - T_r}\right)^m\right] \tag{6.8}$$

while the partial differentiation of Equation 6.8 with respect to temperature T gives the thermal softening term $\frac{\partial \bar{\tau}}{\partial T}$ as

$$\frac{\partial \bar{\tau}}{\partial T} = \frac{1}{\sqrt{3}}\left[A + B\left(\frac{\bar{\gamma}}{\sqrt{3}}\right)^n\right]\left[1 + C\ln\left(\frac{\dot{\bar{\gamma}}}{\dot{\bar{\gamma}}_0}\right)\right]\left[\frac{-m}{T - T_r}\left(\frac{T - T_r}{T_m - T_r}\right)^m\right] \tag{6.9}$$

The second term in the denominator of Recht's criterion $\frac{dT}{d\bar{\gamma}}$ is the rate of change of temperature with strain in the catastrophic shear zone. Recht developed a model [12] to determine the temperature gradient with strain. According to this model, the zone in Fig. 6.1 with unit area *A* and unit thickness *T* is assumed to be the weakest zone within the length *L* of the specimen. Catastrophic shear is achieved by applying a constant rate of average strain $\frac{\dot{x}}{L}$ high enough to produce catastrophic slip in this zone and when this is achieved, this shear zone will remain thin and it can be seen that plastic deformation is confined to this region. Since this zone is very thin, it is assumed to be a plane of uniform heat generation.

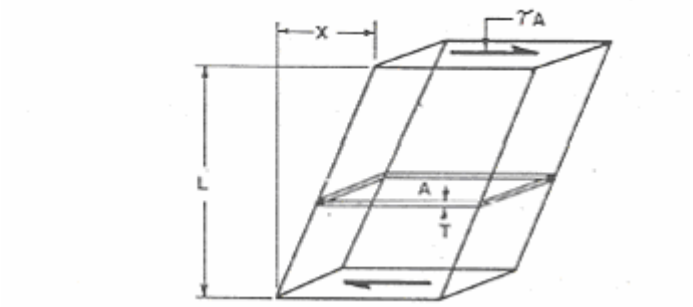

Fig. 6.1 Model used for determination of temperature gradient with strain in catastrophic shear zone [12]

Thus the heat generation rate over the unit area *A* is given by

$$q = \frac{\tau L}{W}\dot{\gamma} \tag{6.10}$$

where q is the heat generation rate per unit area, τ is the shear strength in the weak zone, L is the specimen length, $\dot{\gamma}$ is the average shear strain rate equal to $\frac{\dot{x}}{L}$ and W is the work equivalent of heat. Using Carslaw and Jaeger's solution for the temperature on a plane in

an infinite medium at constant heat generation, the instantaneous temperature T_A on unit area A is given as

$$T_A = \frac{\tau_y L \dot{\gamma}}{W} \sqrt{\frac{t}{\pi \kappa \rho C}} \tag{6.11}$$

where τ_y is the initial shear yield strength, t is the time, κ is the thermal conductivity, C is the specific heat and ρ is the specific weight.

Differentiating the above equation with respect to time t, gives

$$dT_A = \frac{1}{2} \frac{\tau_y L \dot{\gamma}}{W} \sqrt{\frac{1}{\pi \kappa \rho C t}} dt \tag{6.12}$$

But, for constant strain rate, $\gamma = \dot{\gamma} t + \gamma_y$ and $\frac{d\gamma}{dt} = \dot{\gamma}$

where γ is the unit shear strain and γ_y is the initial yield strain.

Substituting these two in Equation 6.12, we get,

$$\frac{dT_A}{d\gamma} = \frac{1}{2} \frac{\tau_y L}{W} \sqrt{\frac{\dot{\gamma}}{\pi \kappa \rho C (\gamma - \gamma_y)}} \tag{6.13}$$

Substituting Equations 6.8, 6.9 and 6.13 in Equation 6.4, will give the following equation which can be used to formulate the Recht's criterion into the UMAT code.

$$R = \frac{\left[\frac{nB}{3} \left(\frac{\bar{\gamma}}{\sqrt{3}} \right)^{n-1} \right] \left[1 - \left(\frac{T - T_r}{T_m - T_r} \right)^m \right]}{\frac{1}{\sqrt{3}} \left[A + B \left(\frac{\bar{\gamma}}{\sqrt{3}} \right)^n \right] \left[\frac{m}{T - T_r} \left(\frac{T - T_r}{T_m - T_r} \right)^m \right] \left[\frac{1}{2} \frac{\tau_y L}{W} \sqrt{\frac{\dot{\gamma}}{\pi \kappa \rho C (\gamma - \gamma_y)}} \right]} \tag{6.14}$$

For each integration point of the element of workpiece mesh, Recht criterion is evaluated. When Recht criterion is satisfied by all the integration points of the element,

the stress state of all these integration points is made zero. The code of the element is stored in a temporary file. All these coded (listed) elements are then deleted and then the border of the workpiece is extracted and smoothed. This smoothing operation reduces the loss of volume in the workpiece determined by element deletion and helps in the convergence of FEM solver. A new mesh is generated and the interpolation gives the new elements of the mesh the corrected properties.

Using C, a program is developed and the values of Recht's criterion *R* is calculated for a particular value of strain, varying the values of strain rates and temperatures. Figs. 6.2 (a) and (b) show the variation of *R* with temperatures and strain rates for strains 3 and 4 respectively.

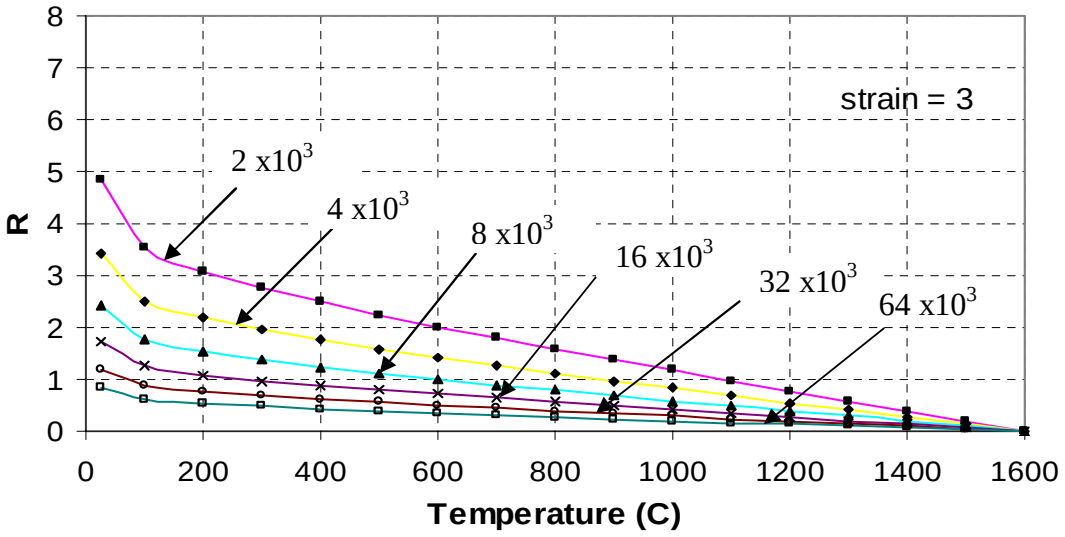

Fig. 6.2 Variation of Recht's criterion value (R) with temperature for Ti 6Al-4V alloy at different strain rates and a strain of 3.

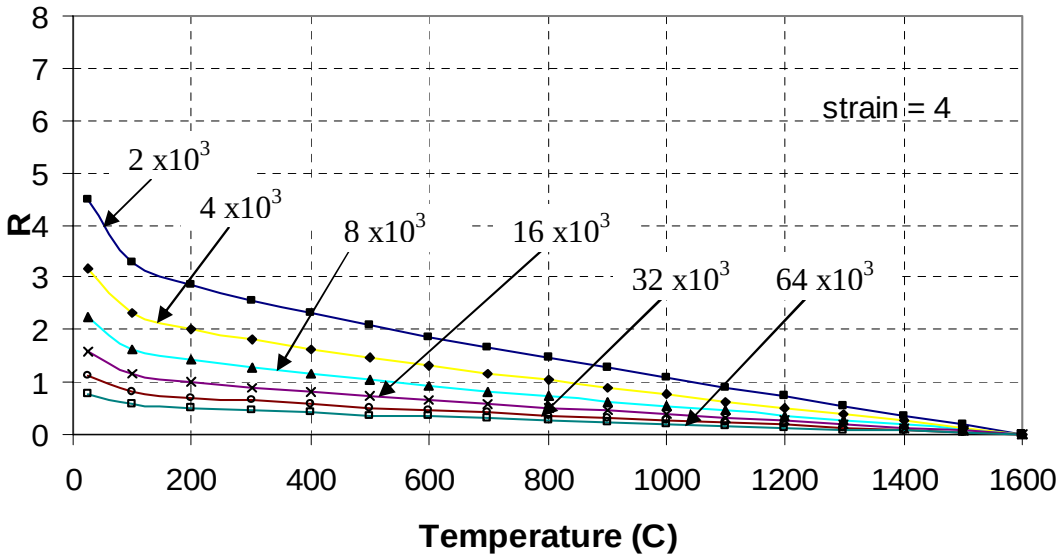

Fig. 6.3 Variation of Recht's criterion value (R) with temperature for Ti 6Al-4V alloy at different strain rates and a strain of 4.

6.4 Stress Update Algorithm

A user subroutine code UMAT is generally used to define the mechanical constitutive behavior of a material and update the solution-dependent state variables. In this study, Johnson-Cook material model is incorporated along with Recht's catastrophic shear failure criterion into the UMAT subroutine. Tool-workpiece system is considered as generalized plane strain case for an elastic/plastic material with isotropic hardening. Stress update algorithm is called for each integration point within an element and the result of this update is finally extrapolated on to the nodes.

The center of the yield surface in the deviatoric stress space is given by the tensor α, which has the initial values of zero. The stress difference, ξ, is the stress measured from the center of the yield surface and is given by

$$\xi = S - \alpha \tag{6.15}$$

where *S* is the deviatoric part of the stress.

The von Mises yield surface is a cylinder in deviatoric stress space with a radius of

$$R^i = \sqrt{\frac{2}{3}}\sigma^i \tag{6.16}$$

where c^i is the flow stress for the i[th] time step.

It is updated for each iteration using Johnson-Cook material model. The normal to the Mises yield surface can be written as

$$Q^i = \sqrt{\frac{3}{2}}\frac{S^i}{c^i} \tag{6.17}$$

The strain rate can be divided into elastic and plastic part using an additive decomposition

$$\dot{\varepsilon} = \dot{\varepsilon}^{el} + \dot{\varepsilon}^{pl} \tag{6.18}$$

The plastic part of the strain rate is given by a normality condition

$$\dot{\varepsilon}^{pl\,i} = \dot{\gamma} Q^i \tag{6.19}$$

where $\dot{\gamma}$ is scalar multiplier which has to be determined.

The equivalent plastic strain rate is related to $\dot{\gamma}$ by

$$\dot{\bar{\varepsilon}}^{pl} = \sqrt{\frac{2}{3}}\dot{\gamma} \tag{6.20}$$

where H^i is the slope of the uniaxial yield stress versus plastic strain curve, given as

$$H^i = \frac{EE_p^{\,i}}{E - E_p^{\,i}} \tag{6.21}$$

where E is the elastic part of Young's modulus and ${E_p}^i$ is the plastic part of the Young's modulus.

Trace of the strain rate increments is computed as

$$tr(d)^k = {d^k}_{11} + {d^k}_{22} + {d^k}_{33} \tag{6.22}$$

A trial elastic stress is computed for each time step as

$${\sigma^{trial}}_{new} = \sigma_{old} + \lambda\ tr(d)^k + (d)^k \tag{6.23}$$

where the subscripts old and new refer to the beginning and end of the increment, respectively; λ and 2μ are the Lame's constants for the material [41]. If the trial stress does not exceed the yield stress, the new stress is set equals to the trial stress. If the yield stress is exceeded, plasticity occurs in the increment. Then the incremental analogs of the rate equation is written as

$${\sigma^i}_{new} = {\sigma^i}_{new}^{trial} - 2\mu\Delta\gamma^i Q^i \tag{6.24}$$

$${\bar{\varepsilon}^{pl}}_{new} = {\bar{\varepsilon}^{pl}}_{old} + \sqrt{\frac{2}{3}}\Delta\gamma \tag{6.25}$$

Iterations for radial return algorithm in the ith time step begin with the computation of deviatoric stress from trial stress state. Hydrostatic stress term is deducted from the directional stress terms to get deviatoric stress state.

$$P^i = \frac{{\sigma_{lm}}^{i(tr)}\delta_{lm}}{3} \qquad\qquad {S^i}^{trial} = {\sigma_{lm}}^{i(tr)} - P^i\delta_{lm} \tag{6.26}$$

The value of increment in equivalent plastic strain $\Delta\gamma$ is used in the incremental equations to determine ${c}_{new}$ and ${\bar{\varepsilon}^{pl}}_{new}$ for each time step [41] where $\Delta\gamma$ for the ith step is given by

$$\Delta\gamma^i = \frac{1}{2\mu\left(1+\frac{H^i}{3\mu}\right)}\left(S^{i\,trial}_{\quad new} : S^{i\,trial}_{\quad new}\right)^{\frac{1}{2}} - R^i \tag{6.27}$$

This algorithm used for numerical integration is often referred to as radial return algorithm because the correction to the trial stress under the active plastic loading condition returns the stress state to the yield surface along the direction defined by the vector from the center of the yield surface to the elastic trial stress. Thus, using the above procedure, stress state and solution dependent variables are updated for each time step.

Finally, it may be noted that implementation of the Recht's criterion for shear failure and the derivation of its equations from Johnson-Cook material model and applying it into the user subroutine code UMAT was conducted jointly with Mr. Dhananjay Joshi and Mr. Parag Konde. The author acknowledges their valuable contributions.

CHAPTER 7

RESULTS AND DISCUSSION

The main objective of this investigation is to study shear-localized chip formation in machining Ti 6Al-4V by conducting finite element simulations under different cutting conditions using commercial simulation software, AdvantEdge™. For this a user material subroutine (UMAT) containing Johnson-Cook material model to represent material behavior under different cutting conditions and Recht's criterion for catastrophic shear failure is developed. Validation of the cutting forces and chip morphology is done with experimental results obtained from the literature.

7.1 Process Model and Material Properties

In the finite element simulations of Ti 6Al-4V machining using AdvantEdge™ the following conventions are followed:

1) The tool is assumed stationary while the workpiece moves at the cutting velocity.
2) The rake and clearance angles are shown with their normal conventions.

3) Workpiece is considered as an elastic-plastic material, material properties are assigned to it rather than selecting the standard workpiece material properties from the AdvantEdge™ software library.
4) Tool material is selected from the standard tool material library of the software. In this study, general carbide tool is considered and it is a rigid-elastic tool.
5) A constant coefficient of friction (0.3) is used for tool-chip interface.
6) Adiabatic temperature boundary conditions are assumed and steady state heat transfer analysis is considered.
7) Depth of cut and cutting speed are constants for the simulation.
8) Effect of cutting fluids is not considered in the simulations.
9) High mesh density is considered in the region of workpiece and tool contact. Fig.7.1 shows the initial mesh for workpiece-tool system.
10) Adaptive remeshing option is utilized to alleviate the excessively deformed workpiece mesh.

A Lawrence Livermore National Laboratory (LLNL) report [9] described the studies of the deformation and failure behavior of Ti 6Al-4V alloy. Data were obtained for those studies at high strain rates of 10^3-10^4 s^{-1} and large strains using split Hopkinson pressure bar technique. Accordingly, this and additional data from literature were used to critically evaluate the ability of the Johnson-Cook material model to represent deformation and failure response of Ti 6Al-4V under conditions relevant to simulations of engine containment and the influence of uncontained debris on aircraft structures. The results of the experimental work reported were used to define a new set of material

constants for the strength component of the Johnson-Cook model for Ti 6Al-4V and it was concluded that Johnson-Cook material model accurately represents the stress-strain response of the material even at high strain rates ($>10^3$-10^4 s^{-1}). The Johnson-Cook parameters for Ti 6Al-4V used in these simulations in (Table 7.1) were taken from this report. Figs. 7.2 and 7.3 show plots from the Johnson-Cook material parameters of true stress-true strain for different values of temperature and variation of true stress with temperature for different values of strains, respectively.

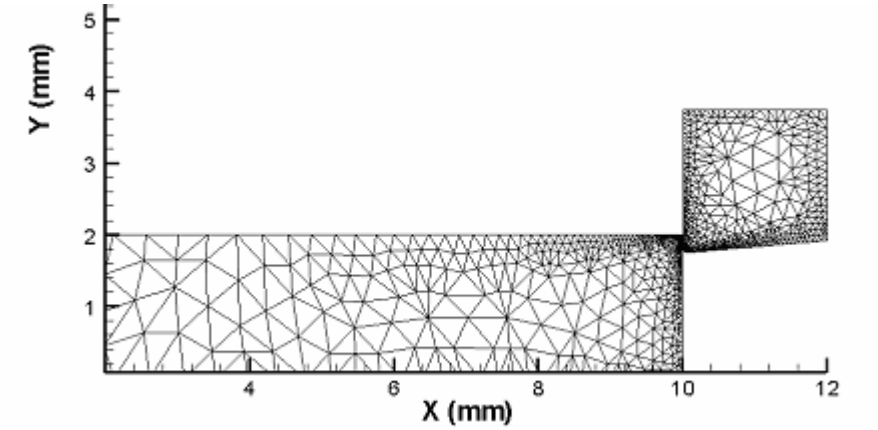

Fig. 7.1 Workpiece-tool system used for FEM simulations showing initial mesh.

Table 7.1 Physical properties of Ti 6Al-4V [9, 43]

Density (Kg/m^3)	4428.8
Rockwell C hardness	36
Elastic modulus (GPa)	113.8
Poissons ratio	0.342
Ultimate tensile strength (MPa)	950
Yield tensile strength (MPa)	880
Thermal conductivity (W/m.K)	6.785

Heat capacity (J/Kg.K)	526.3
Coefficient of thermal expansion (10^{-6} / K)	8.6
Melting temperature range ($^{\circ}$C)	1604-1650

Table 7.2 Johnson-Cook material properties for Ti 6Al-4V [9]

A (GPa)	B (GPa)	C	n	m	$\dot{\varepsilon}_0$ (1/s)	Room Temperature (C)	Melting Temperature (C)
1.098	1.092	0.014	0.93	1.1	0.00001	20.0	1605

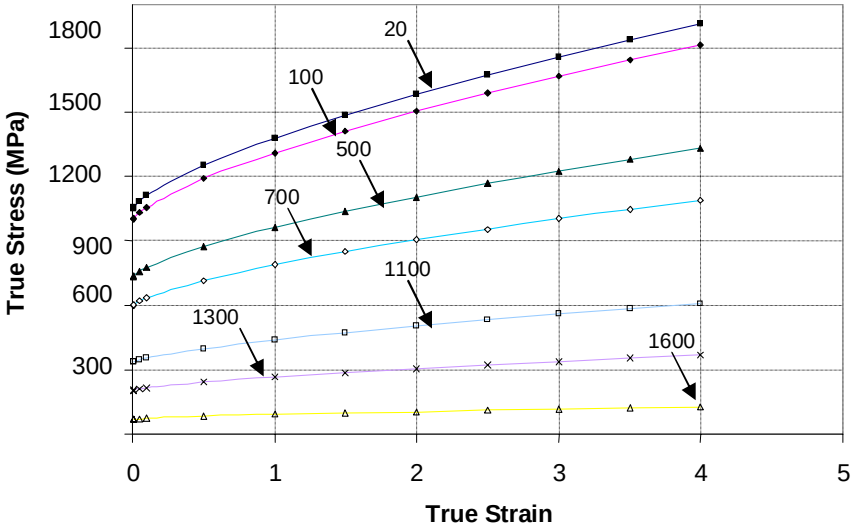

Fig. 7.2 True stress-strain curves of Ti 6Al-4V alloy based on Johnson-Cook material model in the temperature range of 20° to 1600° C at a strain rate of 1x 10^4 s^{-1}.

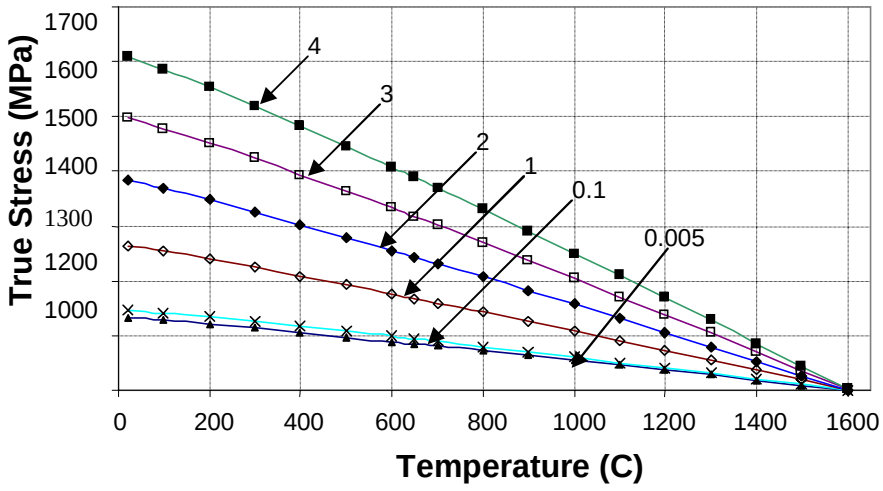

Fig. 7.3 The variation of True stress as a function of temperature for Ti 6Al-4V in the different strain range of 0.005 to 4.0 at a strain rate of $1x\ 10^{4}\ s^{-1}$.

7.2 Simulation Approach and Cutting Conditions

Finite element simulations were performed at different machining conditions, such as cutting speed, depth of cut, rake angle, and coefficient of friction to study their effect on cutting forces, rake face temperature, shear zone temperature, equivalent plastic strain, frequency of chip segmentation, shear band width, and power consumption. The combination of the cutting conditions used for a 3 mm length of cut and 1 mm width of cut can be listed as:

1) For 0.25 mm and 0.5 mm depths of cut and 0° rake angle, the following cutting speeds are used: 10, 20, 30, 40, 50, 60, 70, 80, 90, 100, and 200 m/min.

2) For 0.5 mm depth of cut, 30 m/min cutting speed the following rake angles are used: -15°, 0°, 15°, 30°, 45°.

3) For 0.5 mm depth of cut, 30 m/min cutting speed and 0° rake angle the following coefficients of friction are used: 0.3, 0.5, 0.7, and 0.9.

In addition to these, the following simulations are performed to validate cutting forces and chip morphology with the experimental results available in the literature:

1) For 200 m/min cutting speed and 0° rake angle, the following depths of cut are used: 0.02, 0.05, 0.075, and 0.1mm

2) For 15° rake angle three different cutting speeds of 60, 120 and 240 m/min are used and for each speed, simulations are conducted for two different depths of cut of 0.127 and 0.35 mm.

3) For -6° rake angle and 180 m/min cutting speed four different simulations are performed at depths of cut of 0.04, 0.06, 0.08 and 1.0 mm.

For all these simulations, workpiece, cutting conditions, tool dimensions and adaptive mesh options used are listed in Tables 7.3, 7.4 and 7.5.

Table 7.3 Cutting conditions used for FEM simulations

Workpiece length (mm)	10
Workpiece height (mm)	2
Width of cut (mm)	1
Length of cut (mm)	3

Table 7.4 Tool dimensions used in FEM simulations

Relief angle	5°
Rake length (mm)	2
Relief length (mm)	2
Cutting edge radius	0.05

Table 7.5 Adaptive mesh options input to the FEM software

Mesh refinement factor	8
Mesh coarsening factor	1
Maximum element size (mm)	0.1
Minimum element size (mm)	0.02

7.3 Observations of Chip Formation Process

From metallurgical point of view, Ti 6Al-4V alloy at room temperature has an h.c.p. lattice structure with limited number of slip systems. With increase in temperature, it undergoes an allotropic transformation from a h.c.p. to a b.c.c. structure. The b.c.c. structure has more number of slip systems and this allows more deformation locally wherever the structure has changed to b.c.c. This plastic deformation localizes in a narrow band in primary shear zone due to poor thermal properties of this alloy. With this localized deformation in a narrow band, the heat generated concentrates in this region

leading to increase in temperature. If this local increase in temperature is high enough to cause allotropic transformation, considerable additional slip can occur. This process in turn causes additional heat. Such a mechanism causes the shear localization and leads to instability. This catastrophic shear instability leads to shear-localized chip formation when machining Ti 6Al-4V alloy. The thermoplastic shear instability and adiabatic shear failure in Ti 6Al-4V can be attributed to its poor thermal properties.

While during the machining process, workpiece undergoes tremendous plastic deformation and majority of this deformation occurs in the primary deformation zone. Workmaterial in front of the tool tip and rake face experiences very large compressive stresses, which may be well over yield strength of the material. This leads to plastic instability in the workpiece and shear strain gradually increases in the primary deformation zone leading to strain hardening. Most of the energy expended in the plastic deformation generates heat leading to increase in temperature which softens the material in primary deformation zone. As this machining process involves high strain rates, very small amount of heat transfer occurs between workpiece and the tool due to very short time of deformation. In addition to this, due to low thermal conductivity of Ti 6Al-4V alloy, high temperatures are localized in some region of primary shear zone leading to further thermal softening of the material in this region. The instability then takes place in a narrow band in primary shear zone where material strength has dwindled due to further thermal softening. Shear strains in the zones of instability are much higher than in the segments dividing this shear localized zones. Thus this inhomogeneous strain distribution causes adiabatic pure shear leading to shear-localized chip formation during machining process. Fig.7.4 (a) to (j) shows equivalent plastic strain plots at various stages of chip

segmentation in Ti 6Al-4V alloy simulated at 30 m/min speed and 0.5 mm depth of cut with a -15° rake angle tool.

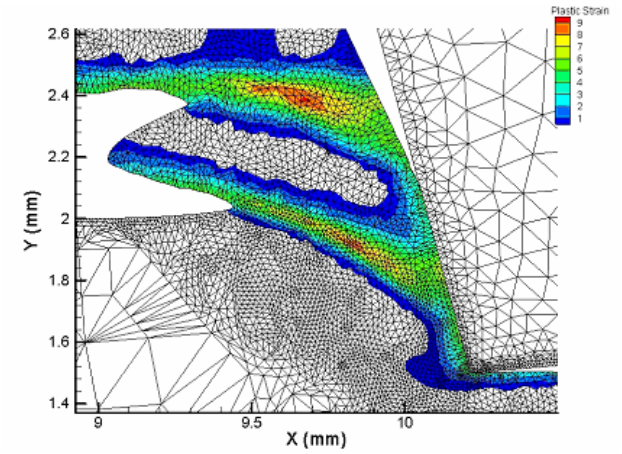

(a)

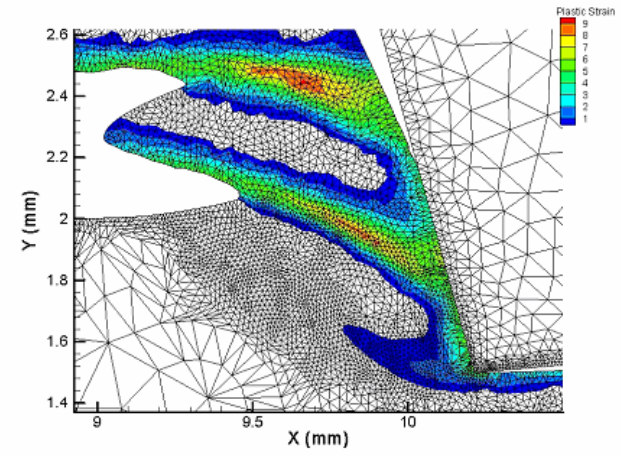

(b)

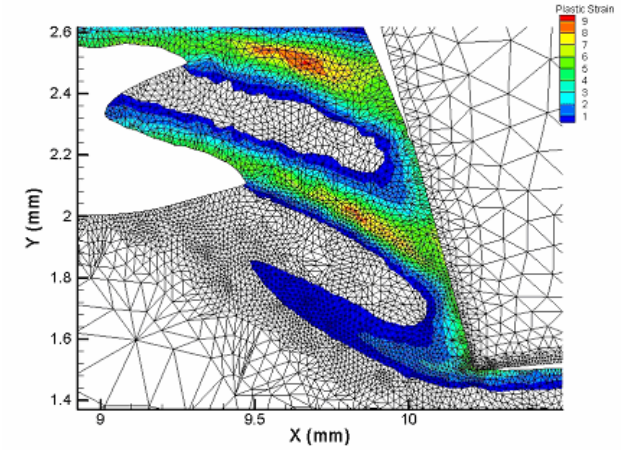

(c)

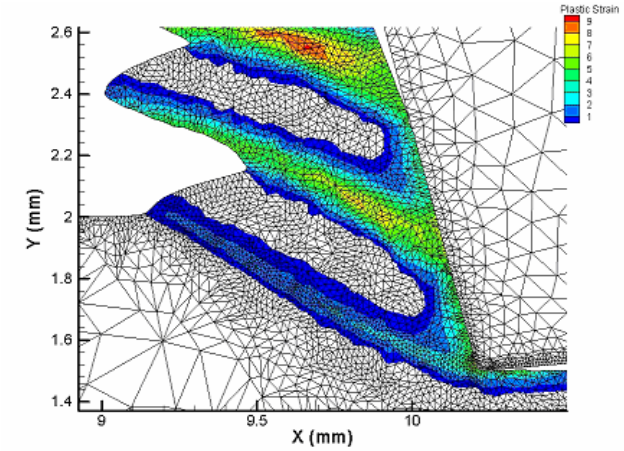

(d)

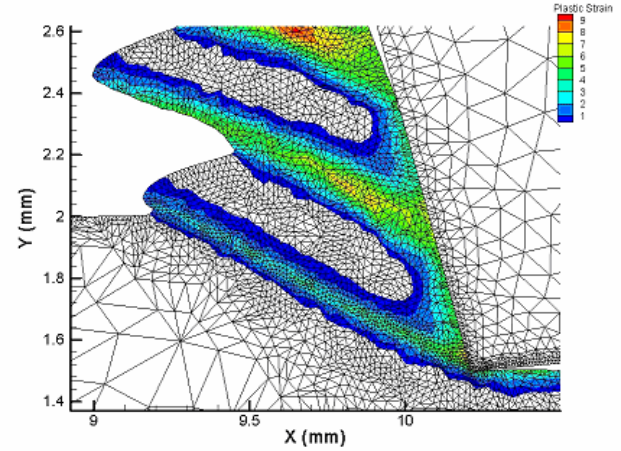

(e)

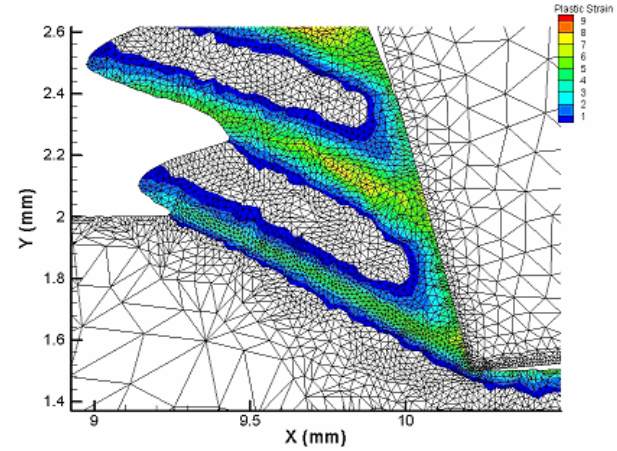

(f)

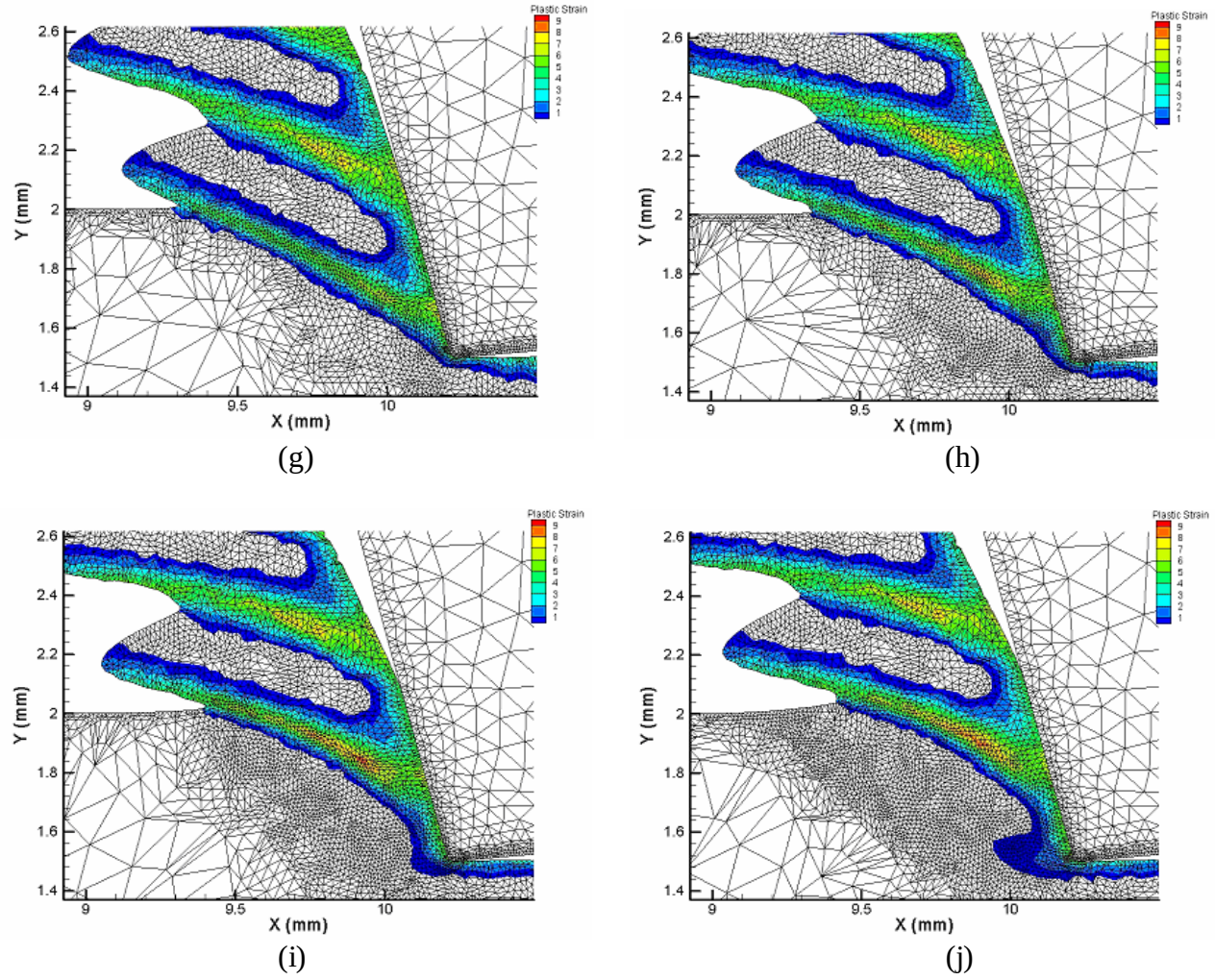

Fig. 7.4Various stages of shear-localized chip formation in machining simulation of Ti 6Al-4V conducted at 30 m/min cutting speed and 0.5 mm depth of cut for -15° rake angle showing equivalent plastic strain localization in narrow shear bands.

The mechanism involved in the shear-localized chip formation as seen from these pictures closely resemble the schematic diagrams of the sequence of events leading to cyclic chip formation when machining Ti 6Al-4V as described by Komanduri and von Turkovich [11] based on the experimental studies. In brief, two stages can be seen in shear-localized chip formation. One stage involves shear instability and strain localization in a narrow band in the primary shear zone ahead of the tool. The other stage

involves upsetting of an inclined wedge of work material by advancing tool, with negligible deformation, forming a chip segment. During first stage of segmented chip formation as explained by Komanduri [26], it can be seen that the initial contact on the tool face with the segment being formed is extremely short and the contact length increases as the upsetting progresses. Also, there is almost no relative motion between the chip segment being formed and the tool face almost until the end of the upsetting process of the chip segmentation. The gradual bulging of the chip segment slowly pushes the chip segment previously formed upwards. The contact between the segment being formed and the previous segment shifts gradually, starting close to the work surface and moving towards the tool face. A distinct feature of the process is the periodic development of narrow shear band with very large strain (~900%) accompanied by rapid shear failure due to plastic instability. Almost no secondary deformation zone is observed in this case unlike in continuous chip formation process. This mechanism of shear-localized chip formation occurs almost at all speeds in case of Ti 6Al-4V alloy. However, as the cutting speed increases, intense shear in the narrow shear band occurs so rapidly that contact area between any two segments decreases to a stage that individual segments of the chip get separated.

7.4 Temperature and Equivalent Plastic Strain distribution in the chip

Fig.7.5 shows the temperature distribution plot of shear-localized chip in Ti 6Al-4V alloy machining simulation for 30 m/min cutting speed and 0.5mm depth of cut with a -15° tool rake angle. The temperature rise is observed to be moderate (~800°C) during the formation of most of the segment because of the low strains involved during upsetting process. However, the temperature rise in the shear failure layer is substantially higher as

the shear strain in this layer is larger at least by an order of magnitude or more. Temperatures as high as 1400°C are noticed in the narrow shear band of the segmented chip and below 100°C in most part of the bulk material of the workpiece. This can be accounted for the poor thermal conductivity of the workpiece material. As high temperatures are seen in the chip than in the bulk of the workpiece material, it can be concluded that most of the heat is carried away by the chips. However, in all the finite element simulations conducted in this investigation, it is observed that high temperatures from the narrow shear band diffuse very rapidly into the bulk material between the chip segments, which in turn is carried away by the chips.

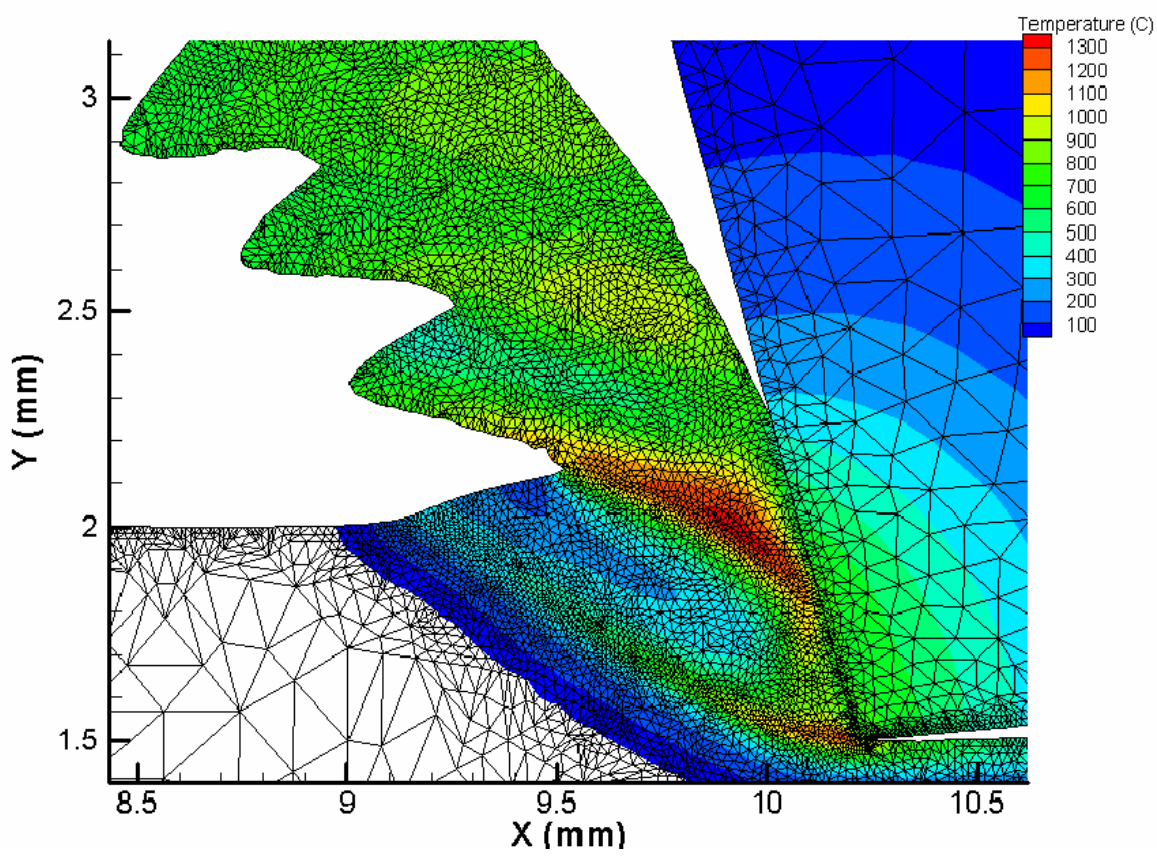

Fig. 7.5 Temperature distribution in the shear-localized chip formation obtained from FEM simulation of machining Ti 6Al-4V at a cutting speed of 30 m/min and a depth of cut of 0.5mm for a -15° rake angle.

Fig.7.6 shows that segments are separated by intense narrow shear bands with high shear strain (>500%) concentrated in the bands and very low strain values (<100%) in the bulk material of the chip segments. Strain localization is clearly observed to start at the tool tip and proceed towards the free end of the workpiece along the shear plane. In addition, intense shear region is seen at the underside of the chip close to the tool face.

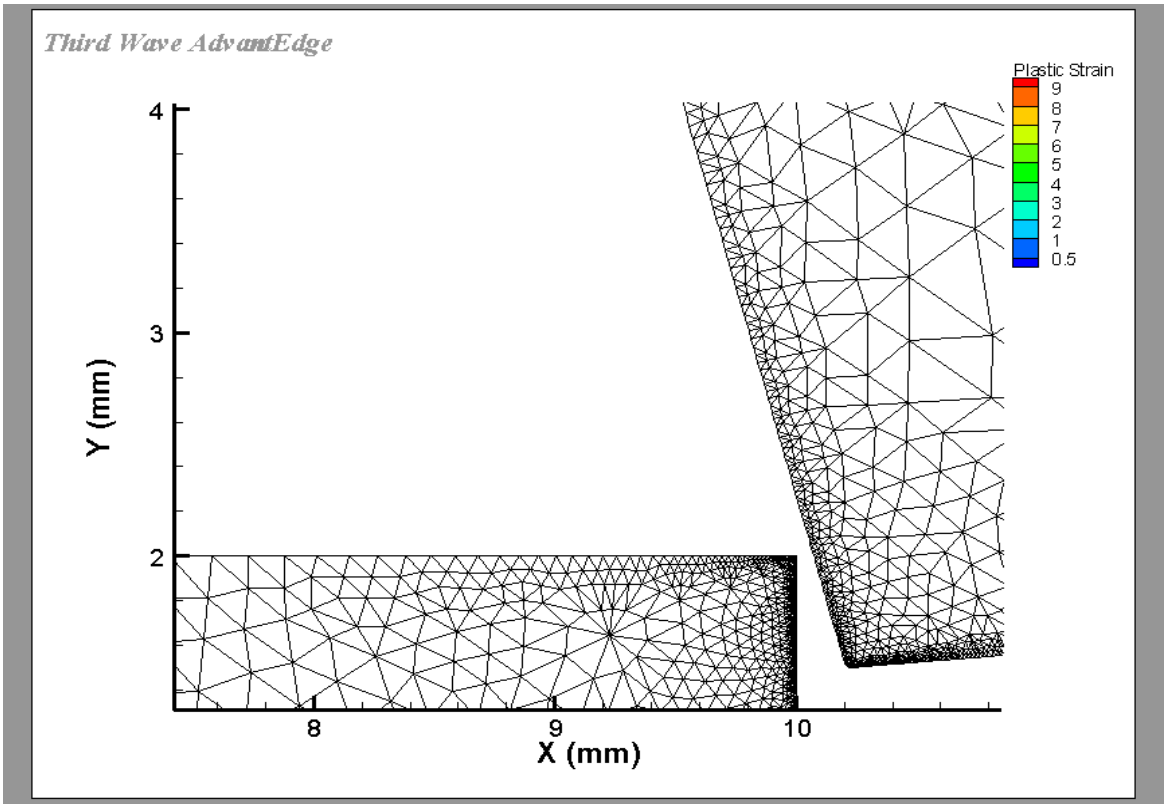

Fig. 7.6 Animation of equivalent plastic strain distribution in the shear-localized chip formation from FEM simulation of machining Ti 6Al-4V at a cutting speed of 30m/min and a depth of cut of 0.5 mm for a -15° rake angle.

This is not actually due to secondary deformation as in the case of continuous chip formation but due to intense shear in a narrow band formed during the upsetting stage of the segment being formed and the one before it [26]. However, this region is relatively insignificant in the case of machining of titanium alloys.

7.5 Effects of Cutting Speed and Feed rate

Figs.7.7 (a) to (j) and Figs.7.8 (a) to (j) show the contour plots of temperature and equivalent plastic strain of Ti 6Al-4V machining simulations conducted for a length of cut of 3 mm at cutting speeds varying from10 to 100 m/min with two different depths of cut 0.25 and 0.5mm. Rake angle of the tool used in this case is 0°. It is observed that as the cutting speed increases, the width of the adiabatic shear band between the segments decreases as heat generated in the shear band has less time to diffuse and hence the number of chip segments increases. In the case of 0.25 mm depth of cut, the number of segments increase from 5 to 10 for an increase in cutting speed from 10 to 100 m/min whereas for 0.5 mm depth of cut the increase in the number of segments is from 3 to 7.Chip segmentation at lower velocities is due to weaker thermo-mechanical instability.

(a)

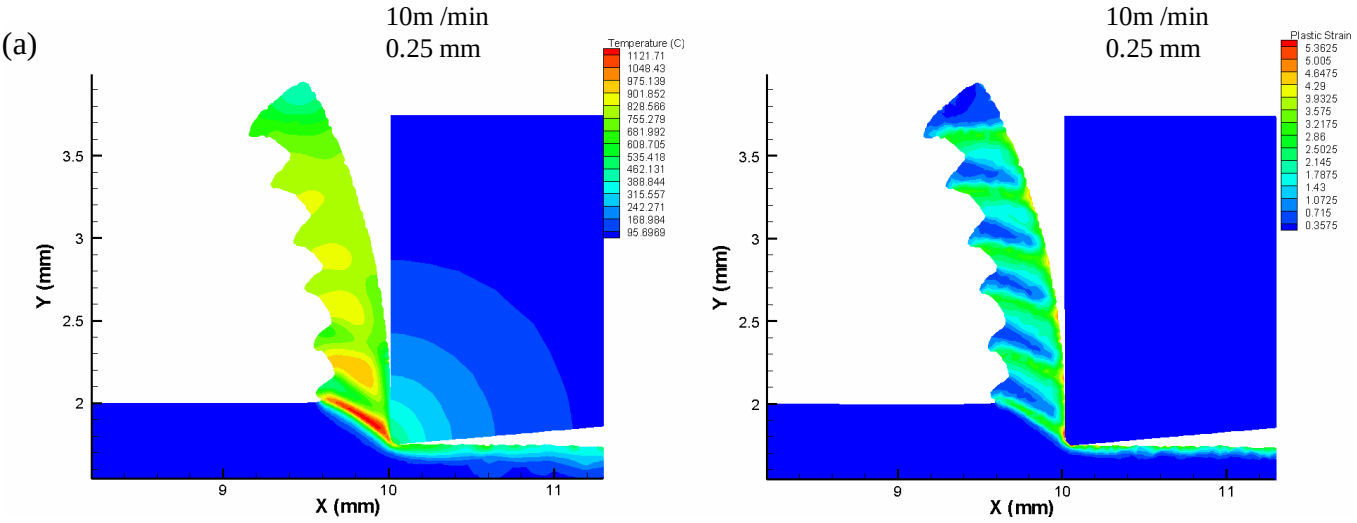

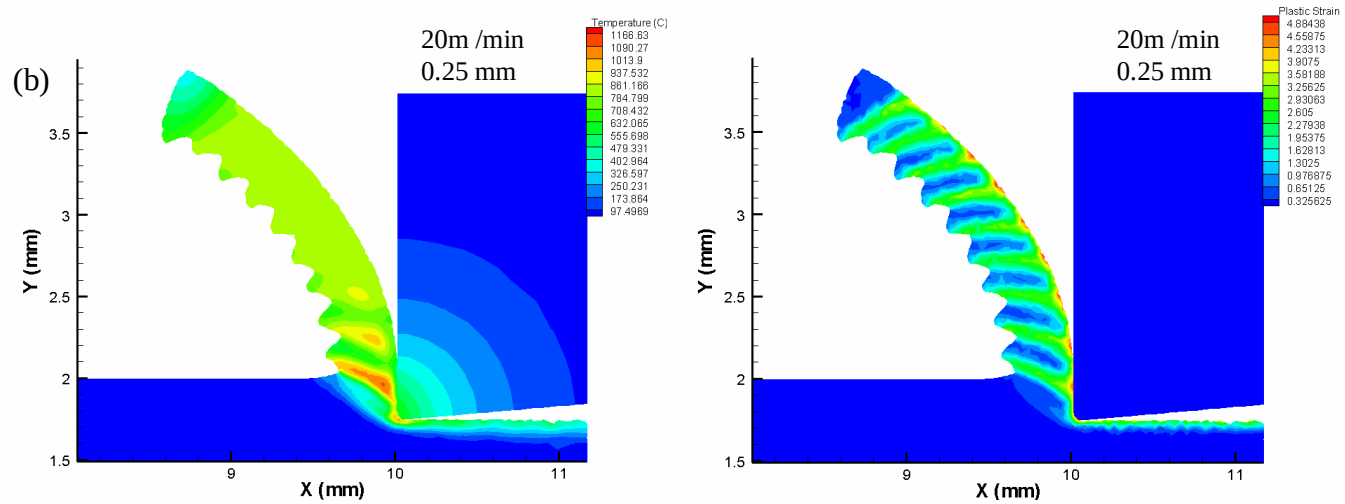
(b)
20m /min
0.25 mm
Temperature (C)
1166.63
1090.27
1013.9
937.532
861.166
784.799
708.432
632.065
555.698
479.331
402.964
326.597
250.231
173.864
97.4989
Y (mm)
X (mm)
20m /min
0.25 mm
Plastic Strain
4.88438
4.55875
4.23313
3.9075
3.58188
3.25625
2.93063
2.605
2.27938
1.95375
1.62813
1.3025
0.976875
0.65125
0.325625
Y (mm)
X (mm)

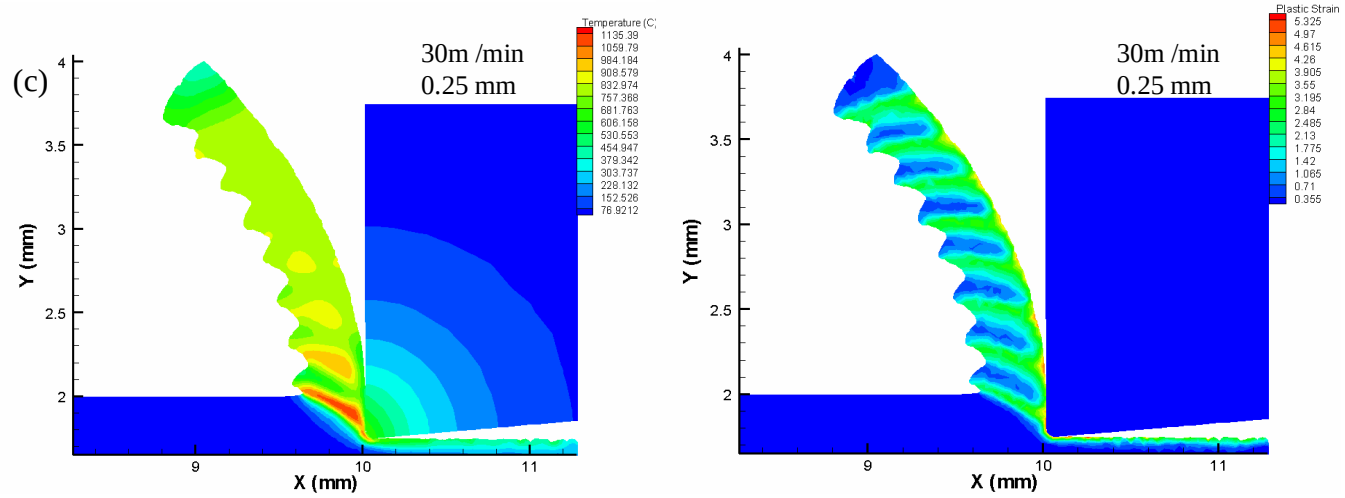
(c)
30m /min
0.25 mm
Temperature (C)
1135.39
1059.79
984.184
908.579
832.974
757.368
681.763
606.158
530.553
454.947
379.342
303.737
228.132
152.526
76.9212
Y (mm)
X (mm)
30m /min
0.25 mm
Plastic Strain
5.325
4.97
4.615
4.26
3.905
3.55
3.195
2.84
2.485
2.13
1.775
1.42
1.065
0.71
0.355
Y (mm)
X (mm)

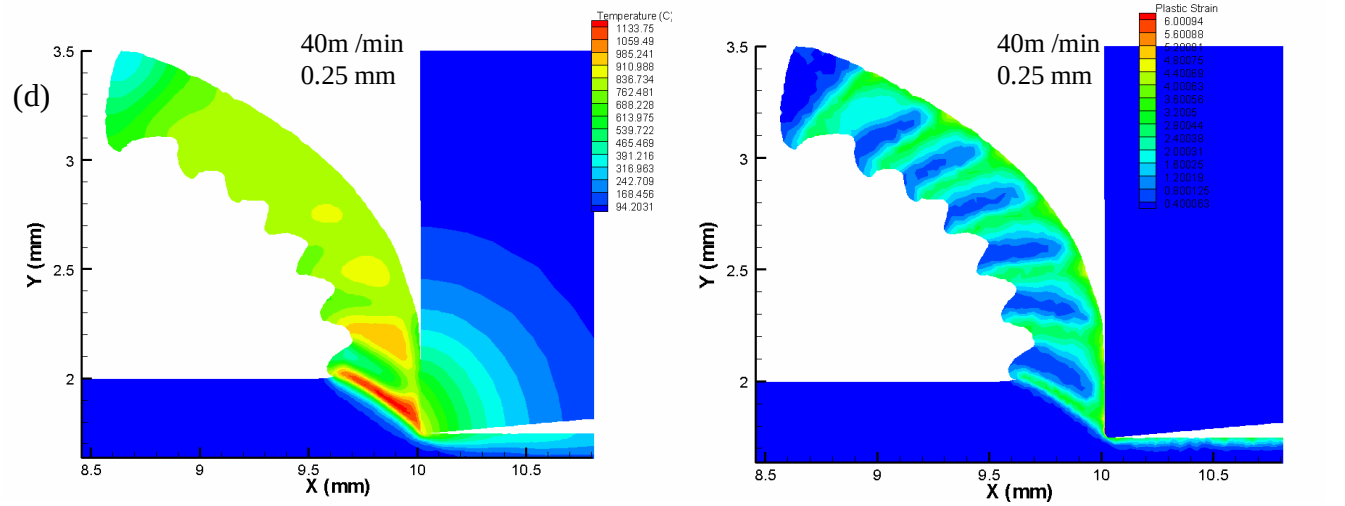
(d)
40m /min
0.25 mm
Temperature (C)
1133.75
1059.49
985.241
910.988
836.734
762.481
688.228
613.975
539.722
465.469
391.216
316.963
242.709
168.456
94.2031
Y (mm)
X (mm)
40m /min
0.25 mm
Plastic Strain
6.00094
5.60088
4.80075
4.40069
4.00063
3.60056
3.2005
2.80044
2.40038
2.00031
1.60025
1.20019
0.800125
0.400063
Y (mm)
X (mm)

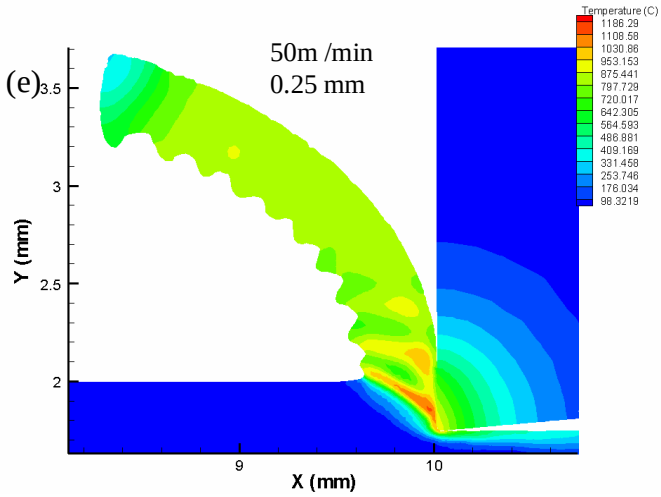
(e)
50m /min
0.25 mm
Temperature (C)
1186.29
1108.58
1030.86
953.153
875.441
797.729
720.017
642.305
564.593
486.881
409.169
331.458
253.746
176.034
98.3219
Y (mm)
X (mm)

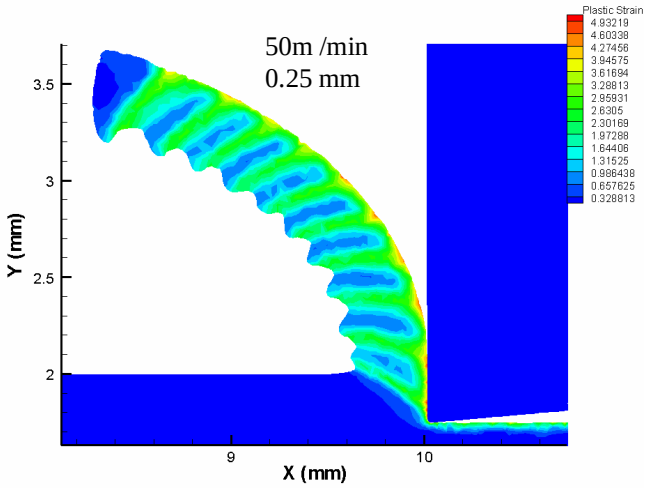
50m /min
0.25 mm
Plastic Strain
4.93219
4.60338
4.27456
3.94575
3.61694
3.28813
2.95931
2.6305
2.30169
1.97288
1.64406
1.31525
0.986438
0.657625
0.328813
Y (mm)
X (mm)

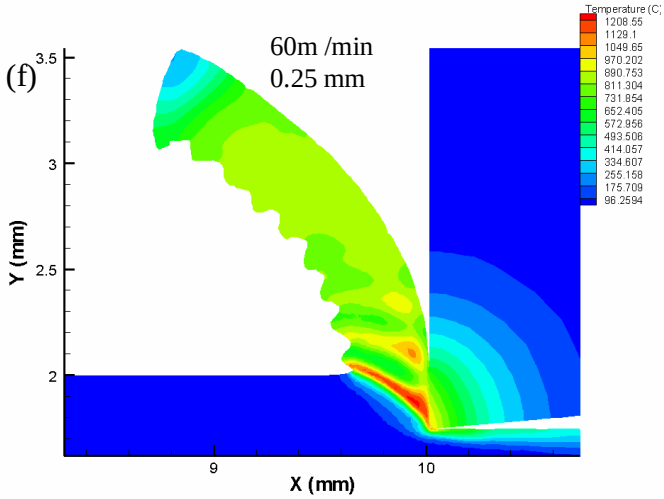
(f)
60m /min
0.25 mm
Temperature (C)
1208.55
1129.1
1049.65
970.202
890.753
811.304
731.854
652.405
572.956
493.508
414.057
334.607
255.158
175.709
96.2594
Y (mm)
X (mm)

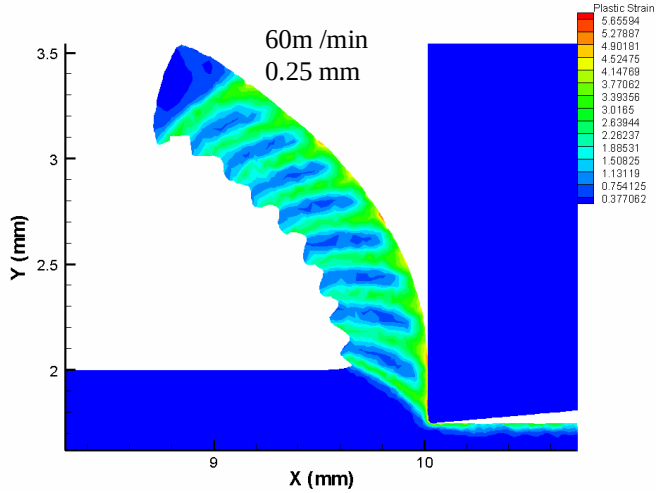
60m /min
0.25 mm
Plastic Strain
5.65594
5.27887
4.90181
4.52475
4.14769
3.77062
3.39356
3.0165
2.63944
2.26237
1.88531
1.50825
1.13119
0.754125
0.377062
Y (mm)
X (mm)

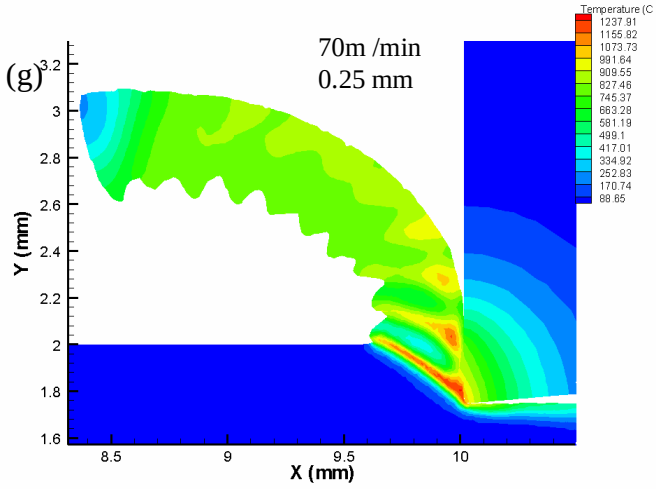
(g)
70m /min
0.25 mm
Temperature (C
1237.91
1155.82
1073.73
991.64
909.55
827.46
745.37
663.28
581.19
499.1
417.01
334.92
252.83
170.74
88.65
Y (mm)
X (mm)

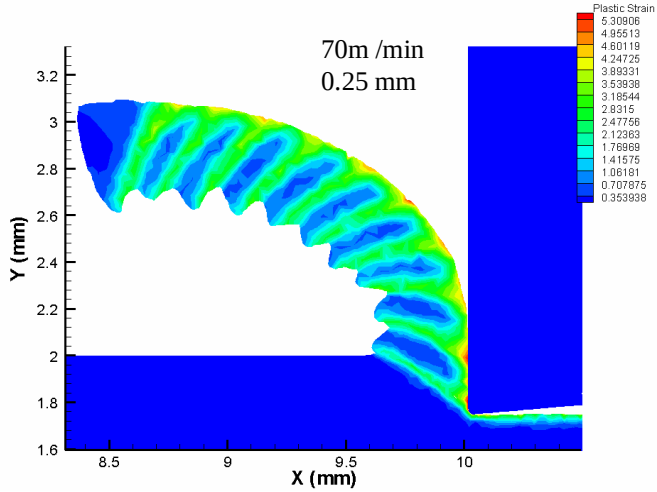
70m /min
0.25 mm
Plastic Strain
5.30906
4.95513
4.60119
4.24725
3.89331
3.53938
3.18544
2.8315
2.47756
2.12363
1.76969
1.41575
1.06181
0.707875
0.353938
Y (mm)
X (mm)

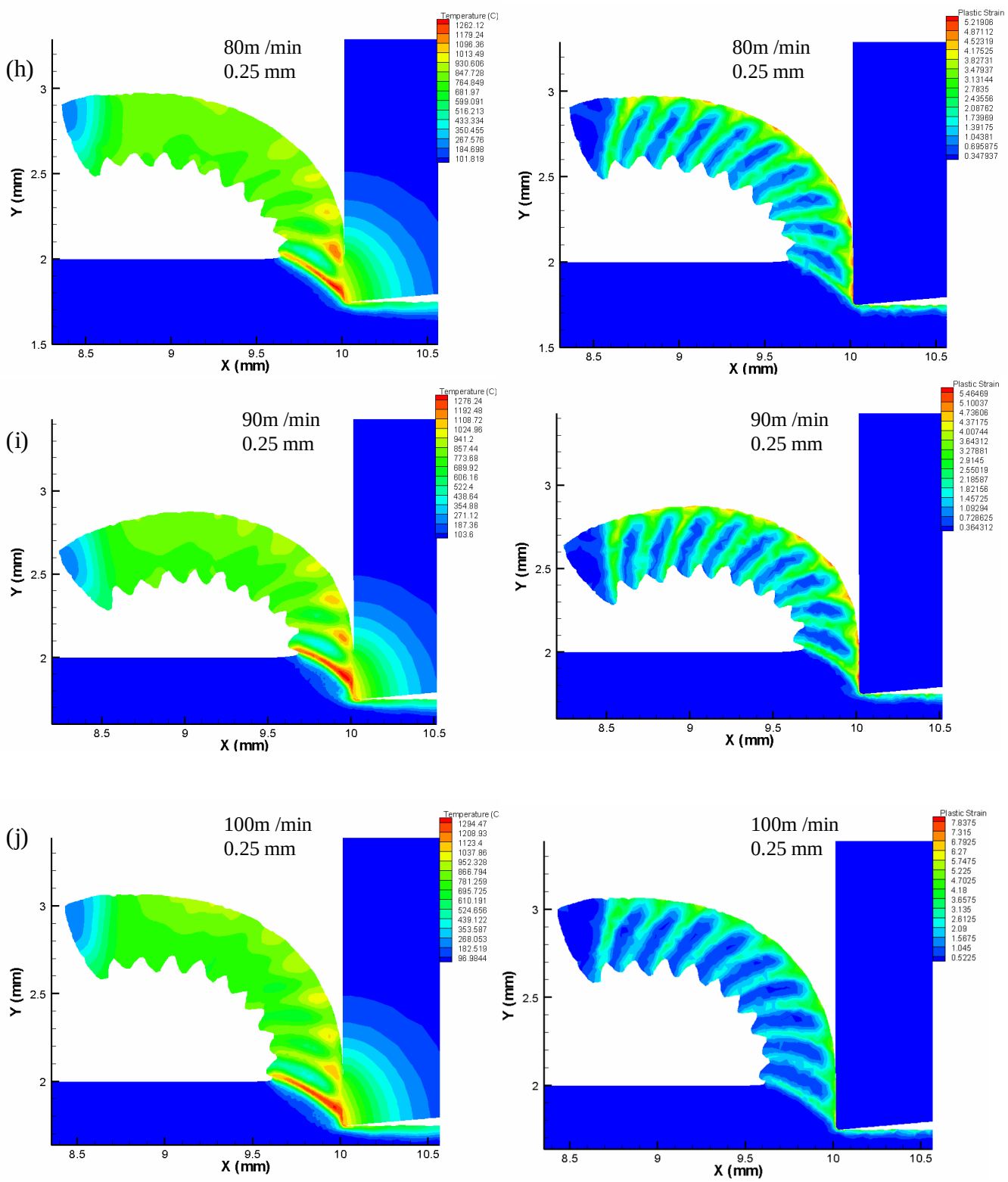

Fig. 7.7 Temperature and equivalent plastic strain contour plots in shear-localized chips formed in machining simulations of Ti 6Al-4V for a depth of cut of 0.25 mm at different cutting speeds varying from 10 to100 m/min using 0° rake angle tool.

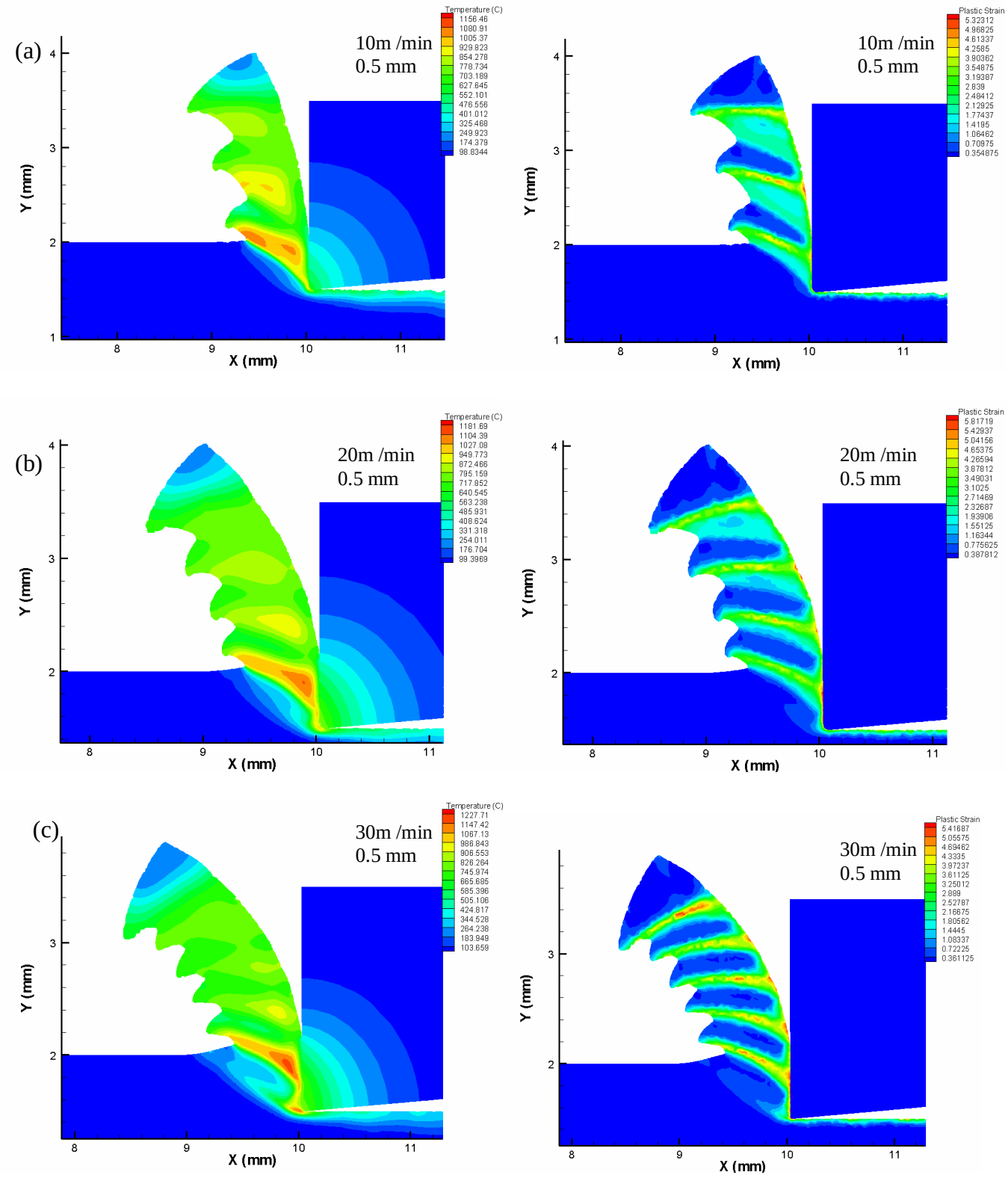
(a)
10m /min
0.5 mm
Temperature (C)
1156.46
1080.91
1005.37
929.823
854.278
778.734
703.189
627.645
552.101
476.556
401.012
325.468
249.923
174.379
98.8344
Plastic Strain
5.32312
4.96825
4.61337
4.2585
3.90362
3.54875
3.19387
2.839
2.48412
2.12925
1.77437
1.4195
1.06462
0.70975
0.354875
(b)
20m /min
0.5 mm
Temperature (C)
1181.69
1104.39
1027.08
949.773
872.466
795.159
717.852
640.545
563.238
485.931
408.624
331.318
254.011
176.704
99.3969
Plastic Strain
5.81719
5.42937
5.04156
4.65375
4.26594
3.87812
3.49031
3.1025
2.71469
2.32687
1.93906
1.55125
1.16344
0.775625
0.387812
(c)
30m /min
0.5 mm
Temperature (C)
1227.71
1147.42
1067.13
986.843
906.553
826.264
745.974
665.685
585.396
505.106
424.817
344.528
264.238
183.949
103.659
Plastic Strain
5.41687
5.05575
4.69462
4.3335
3.97237
3.61125
3.25012
2.889
2.52787
2.16675
1.80562
1.4445
1.08337
0.72225
0.361125
Y (mm)
X (mm)

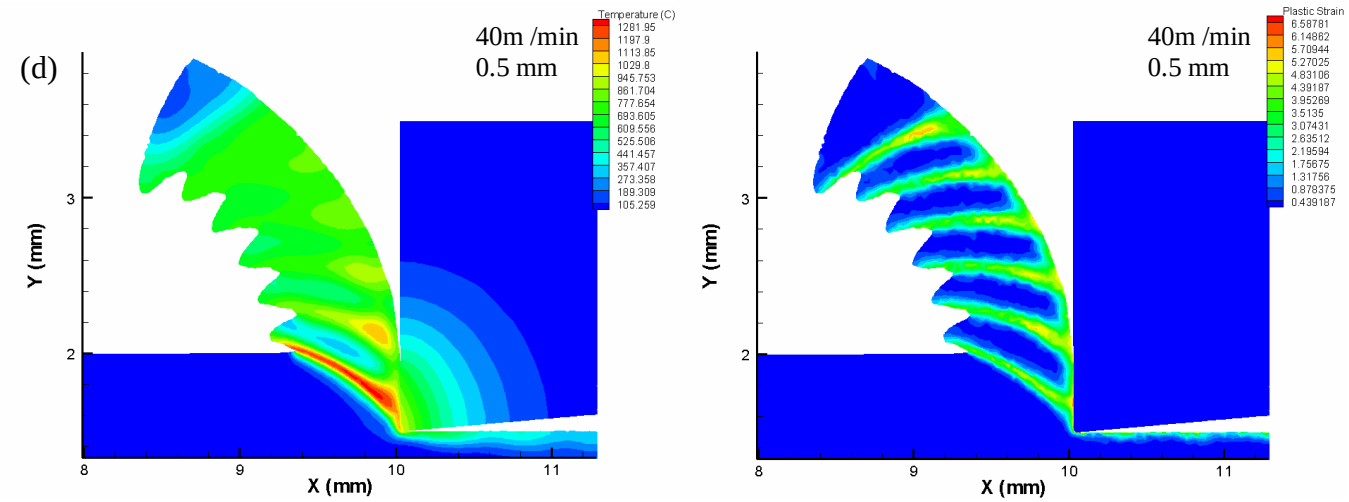
(d)
40m /min
0.5 mm
Temperature (C)
1281.95
1197.9
1113.85
1029.8
945.753
861.704
777.654
693.605
609.556
525.506
441.457
357.407
273.358
189.309
105.259
Y (mm)
X (mm)
40m /min
0.5 mm
Plastic Strain
6.58781
6.14862
5.70944
5.27025
4.83106
4.39187
3.95269
3.5135
3.07431
2.63512
2.19594
1.75675
1.31756
0.878375
0.439187
Y (mm)
X (mm)

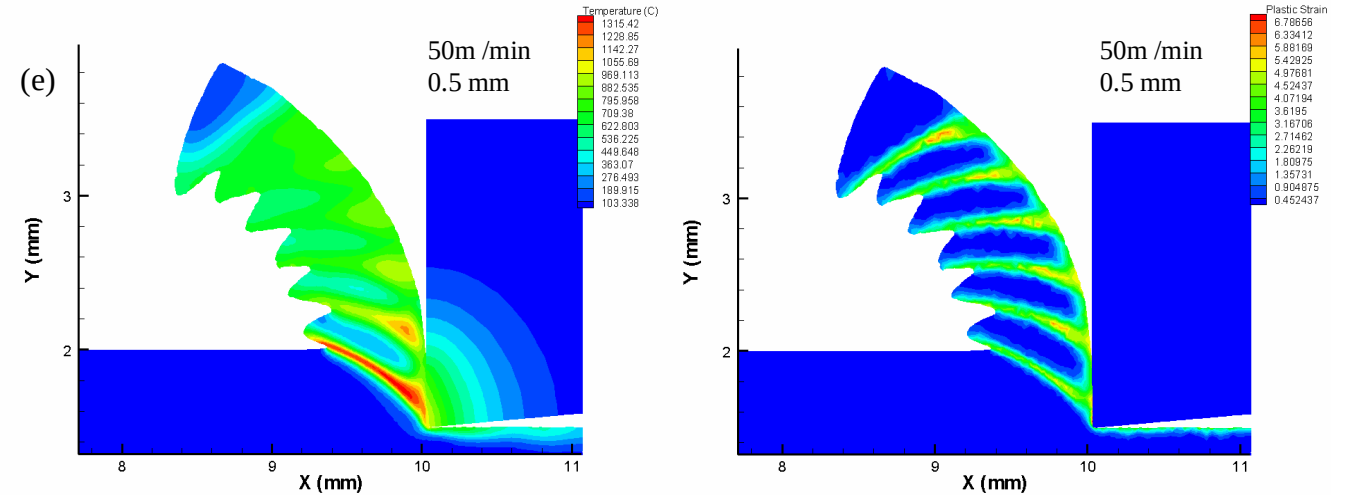
(e)
50m /min
0.5 mm
Temperature (C)
1315.42
1228.85
1142.27
1055.69
969.113
882.535
795.958
709.38
622.803
536.225
449.648
363.07
276.493
189.915
103.338
Y (mm)
X (mm)
50m /min
0.5 mm
Plastic Strain
6.78656
6.33412
5.88169
5.42925
4.97681
4.52437
4.07194
3.6195
3.16706
2.71462
2.26219
1.80975
1.35731
0.904875
0.452437
Y (mm)
X (mm)

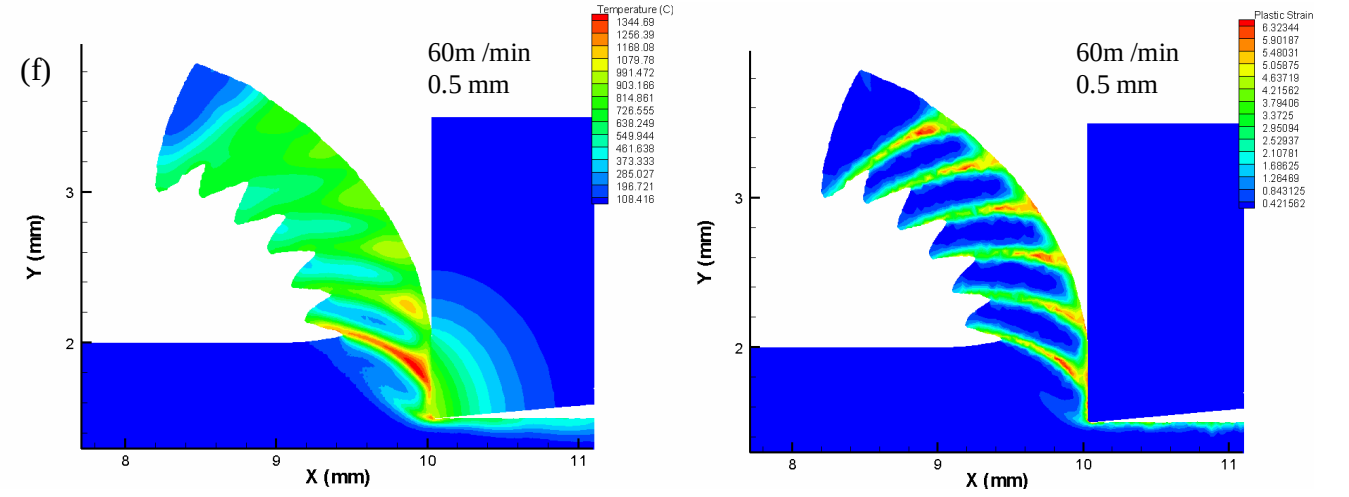
(f)
60m /min
0.5 mm
Temperature (C)
1344.69
1256.39
1168.08
1079.78
991.472
903.166
814.861
726.555
638.249
549.944
461.638
373.333
285.027
196.721
108.416
Y (mm)
X (mm)
60m /min
0.5 mm
Plastic Strain
6.32344
5.90187
5.48031
5.05875
4.63719
4.21562
3.79406
3.3725
2.95094
2.52937
2.10781
1.68625
1.26469
0.843125
0.421562
Y (mm)
X (mm)

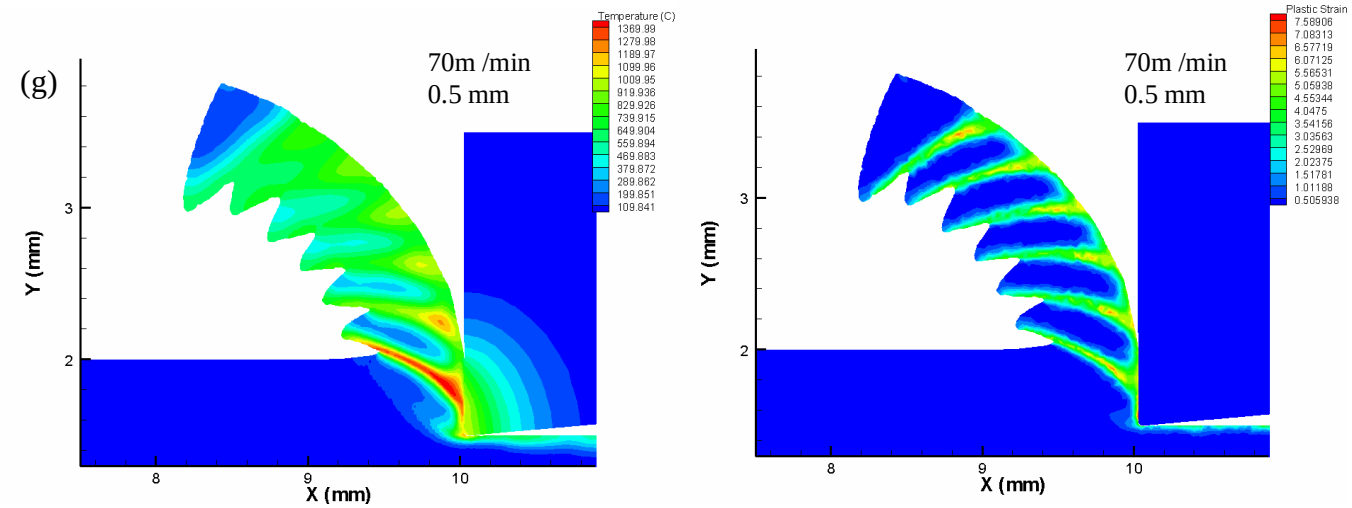
(g)
70m /min
0.5 mm
Temperature (C)
1389.99
1279.98
1189.97
1099.96
1009.95
919.936
829.926
739.915
649.904
559.894
469.883
379.872
289.862
199.851
109.841
Y (mm)
X (mm)
70m /min
0.5 mm
Plastic Strain
7.58906
7.08313
6.57719
6.07125
5.56531
5.05938
4.55344
4.0475
3.54156
3.03563
2.52969
2.02375
1.51781
1.01188
0.505938
Y (mm)
X (mm)

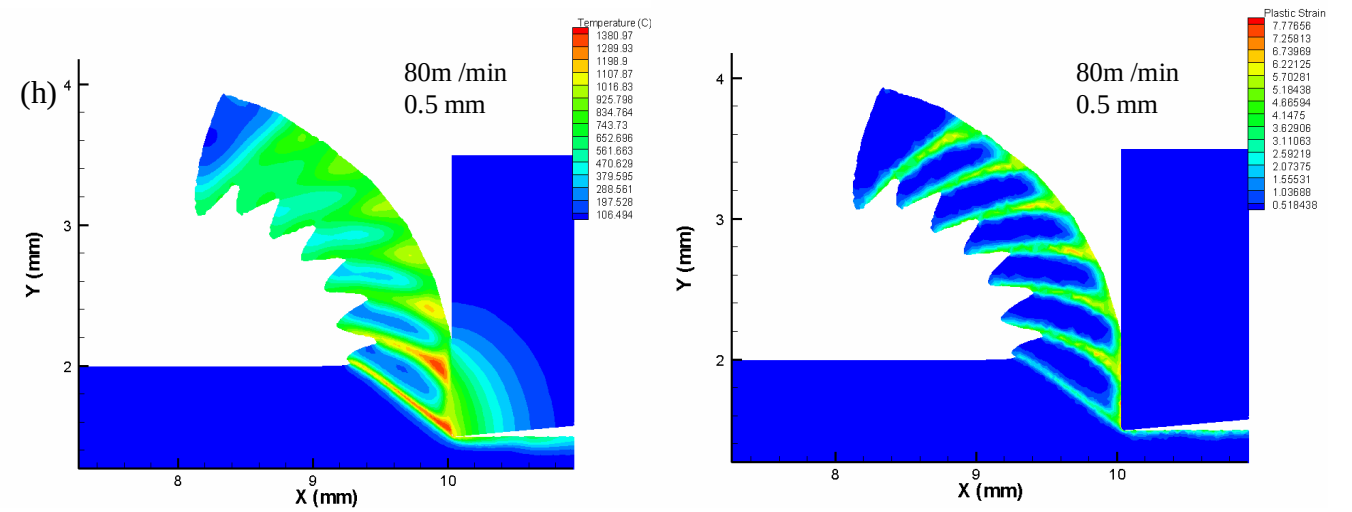
(h)
80m /min
0.5 mm
Temperature (C)
1390.97
1299.93
1198.9
1107.87
1016.83
925.798
834.764
743.73
652.696
561.663
470.629
379.595
288.561
197.528
106.494
Y (mm)
X (mm)
80m /min
0.5 mm
Plastic Strain
7.77656
7.25813
6.73969
6.22125
5.70281
5.18438
4.66594
4.1475
3.62906
3.11063
2.59219
2.07375
1.55531
1.03688
0.518438
Y (mm)
X (mm)

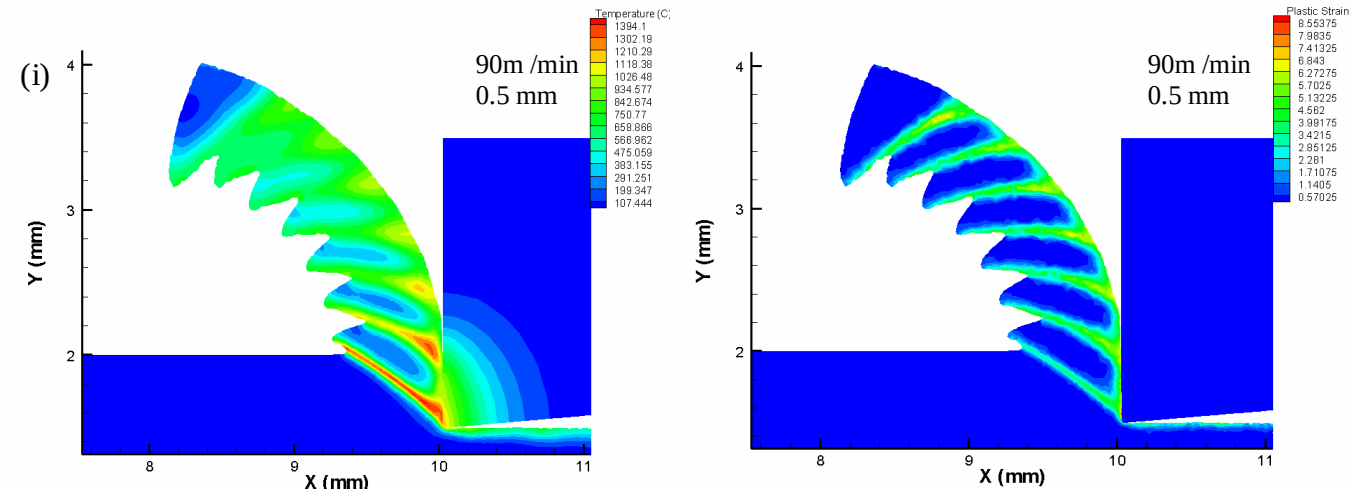
(i)
90m /min
0.5 mm
Temperature (C)
1394.1
1302.19
1210.29
1118.38
1026.48
934.577
842.674
750.77
658.866
566.962
475.059
383.155
291.251
199.347
107.444
Y (mm)
X (mm)
90m /min
0.5 mm
Plastic Strain
8.55375
7.9835
7.41325
6.843
6.27275
5.7025
5.13225
4.562
3.99175
3.4215
2.85125
2.281
1.71075
1.1405
0.57025
Y (mm)
X (mm)

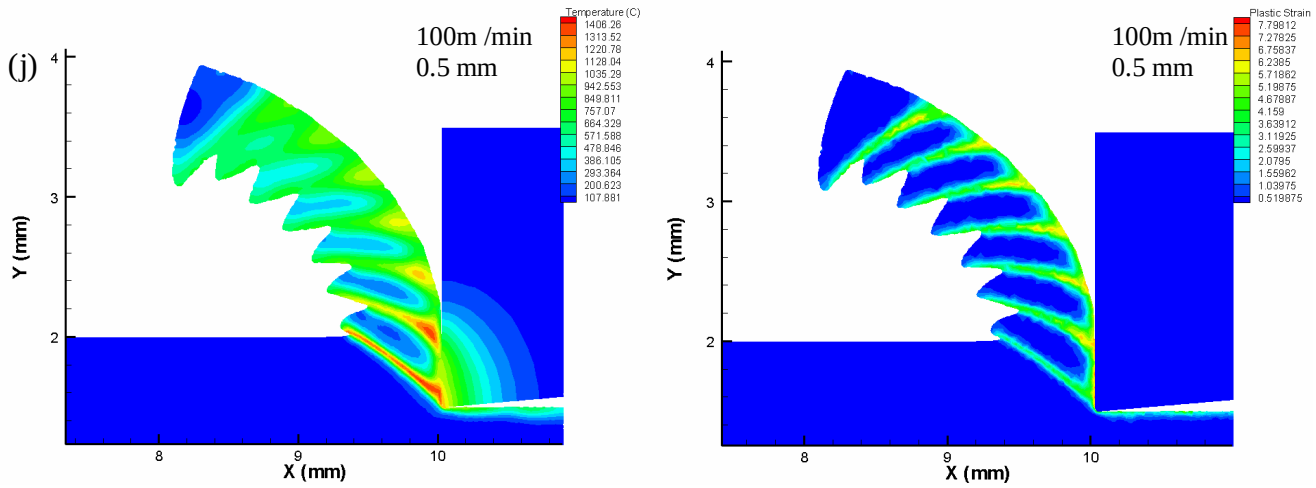

Fig. 7.8 Temperature and equivalent plastic strain contour plots in shear-localized chips formed in machining simulations of Ti 6Al-4V for a depth of cut of 0.5 mm at different cutting speeds varying from 10 to100 m/min using 0° rake angle tool.

Localization of plastic flow is not so intense as in the case of higher cutting speeds. Equivalent plastic strain in the shear zone is observed to be dependent on thermo-mechanical instability.

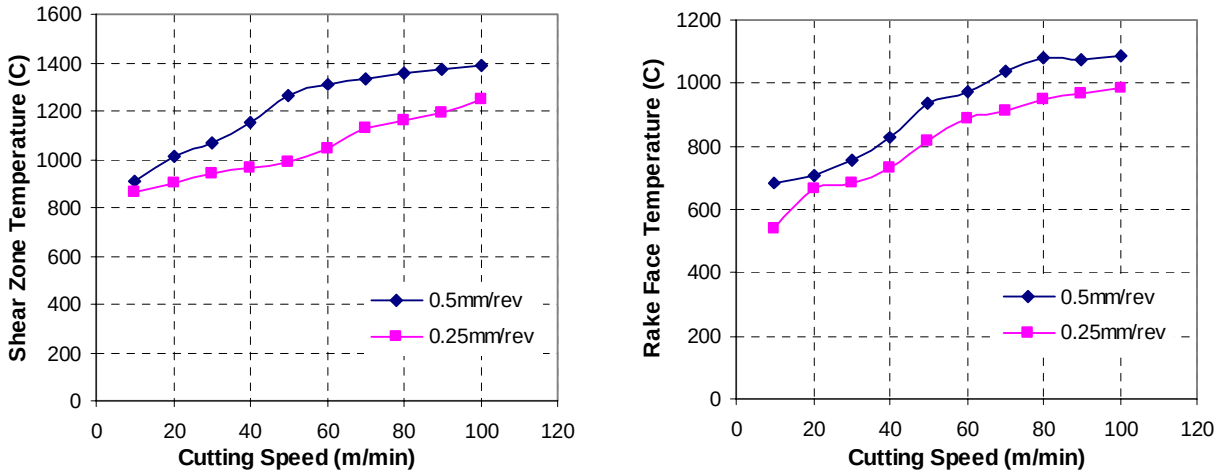

(a) (b)

Fig. 7.9 Effect of cutting speed on (a) the shear zone temperature and (b) the rake face temperature for FEM simulations of Ti 6Al-4V at cutting speeds from 10 to 100 m/min for two different depths of cut of 0.25 and 0.5 mm.

Figs.7.10 (a) and (b) show that equivalent plastic strain and strain rate in the shear zone increases with increase in cutting speed. For a depth of cut of 0.25 mm, the strain rate at 10 m/min cutting speed is ~ 4×10^3 s^{-1} and it increases to 18×10^3 s^{-1} when the cutting speed increases to 100 m/min. While the increase in strain rate for a depth of cut of 0.5 mm and cutting speed increase from 10 to 100 m/min is from 45×10^2 s^{-1} to 34×10^3 s^{-1}.

At the initial stage of cutting, the plastic strains are relatively small and concentrate around the tool tip in both the chip and the machined surface. As the cutting process continues, strains increase and spread out into a narrow zone where shear banding occurs. The maximum value of equivalent plastic strain in a narrow shear band goes upto 6. As the cutting speed increases from 10 m/min to 100 m/min, the average value of equivalent plastic strain in shear zone increases by 200%.

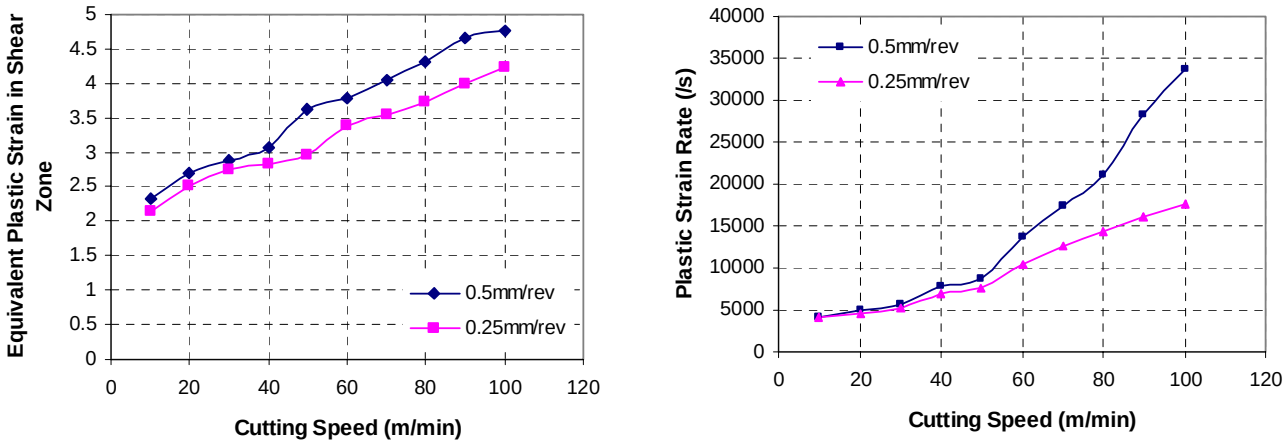

(a) (b)

Fig.7.10 Effect of cutting speed on (a) equivalent plastic strain and (b) plastic strain rate for FEM simulations of Ti 6Al-4V at cutting speeds varying from 10 to 100 m/min for two different depths of cut of 0.25 and 0.5mm.

Fig.7.9 shows that shear zone temperature increases with the increase in cutting speed as the heat generated in the shear zone has less time to dissipate. The maximum temperature

in the shear band reaches ~1400°C. With increase in cutting speed, the chip-tool contact area reduces and rake face temperature increases. This is because intense heat is concentrated in this reduced area resulting in high tool temperatures as the cutting speed increases.

At higher cutting speeds, thermo-mechanical instability is intense and less work is needed for the shear failure. Hence, the value of average cutting force and average thrust force decreases with the increase in cutting speed as shown in Fig.7.14. In case of 0.25mm depth of cut, average value of the cutting force is observed to decrease from 700N to 500N as the cutting speed increases from 10 to 100m/min; while the decrease is from 1200N to 900N in case of 0.5mm depth of cut. Cyclic variation of cutting force is seen from Fig.7.11 with increase during upsetting stage of the chip segmentation and drastic drop during the shear failure stage. Same variation as cutting force is observed for power consumption during chip segmentation process. Fig.7.15 (a) shows that the average value of power consumption increases with the increase in the cutting speed.

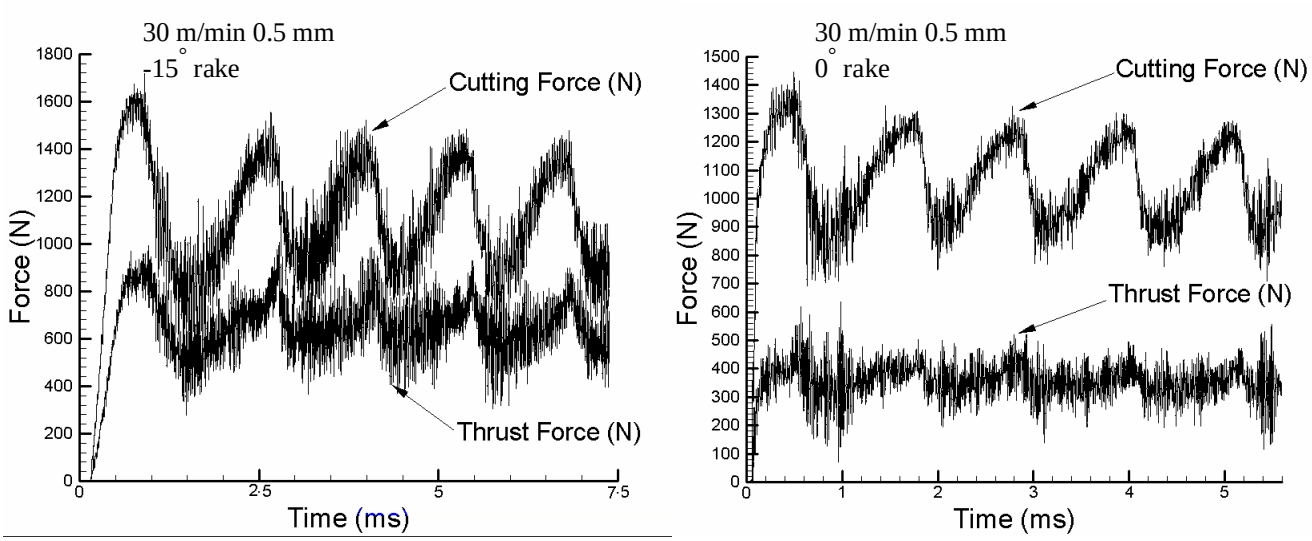

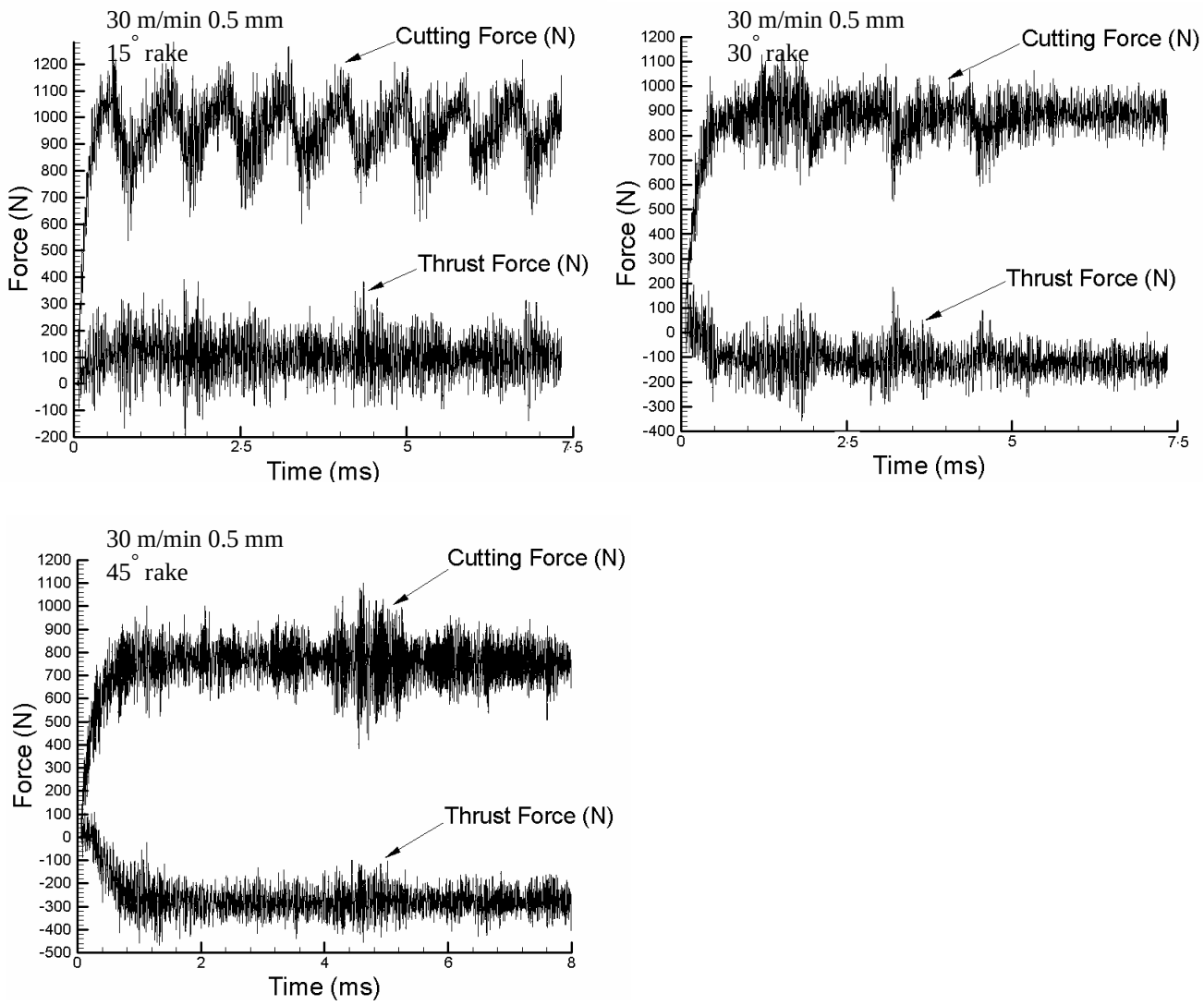

Fig. 7.11 Cutting and thrust force plots with time for finite element simulations of Ti 6Al-4V for a cutting speed of 30 m/min and depth of cut of 0.5 mm using different rake angles of -15°, 0°, 15°, 30° and 45°.

Fig.7.11 shows the dynamic components of cutting and thrust forces for different rake angles and it is observed for -15° rake angle that the cutting force reaches to as high as 1400 N during upsetting stage of the chip segmentation process and drops to 800 N during shear failure stage. And as the rake angle varies from -15° to 45° it is observed that this cyclic variation in the cutting force gradually reduces and for 45° rake angle, it is almost constant showing the chip form variation from segmented to continuous. It is also

observed that the dynamic components of cutting and thrust force are not smooth curves. This is due to serious vibrations that are encountered during Ti 6Al-4V machining which can be accounted for low elastic modulus of the alloy.

For cutting speeds less than 10 m/min, no shear localization is observed for a depth of cut of 0.25 mm and a continuous chip is formed. Figs. 7.12 (a) and (b) shows temperature and equivalent plastic strain plots for finite element simulation of Ti 6Al-4V at 5 m/min cutting speed and 0.25 mm depth of cut. Whereas for 5 m/min cutting speed and 0.5 mm depth of cut, shear-localized chip formation is noticed but from Fig. 7.13 it can be seen that shear localization is not in a narrow band.

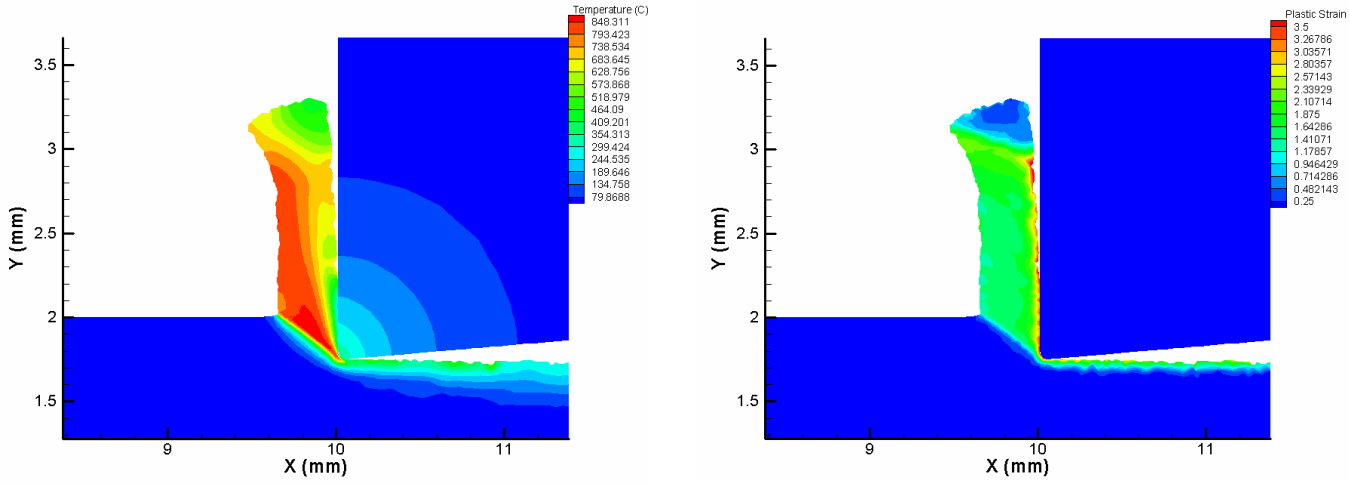

Fig. 7.12 Temperature and equivalent plastic strain contour plots in the chip formed in machining simulation of Ti 6Al-4V for a depth of cut of 0.25 mm and a cutting speed of 5 m/min using a 0° rake angle tool.

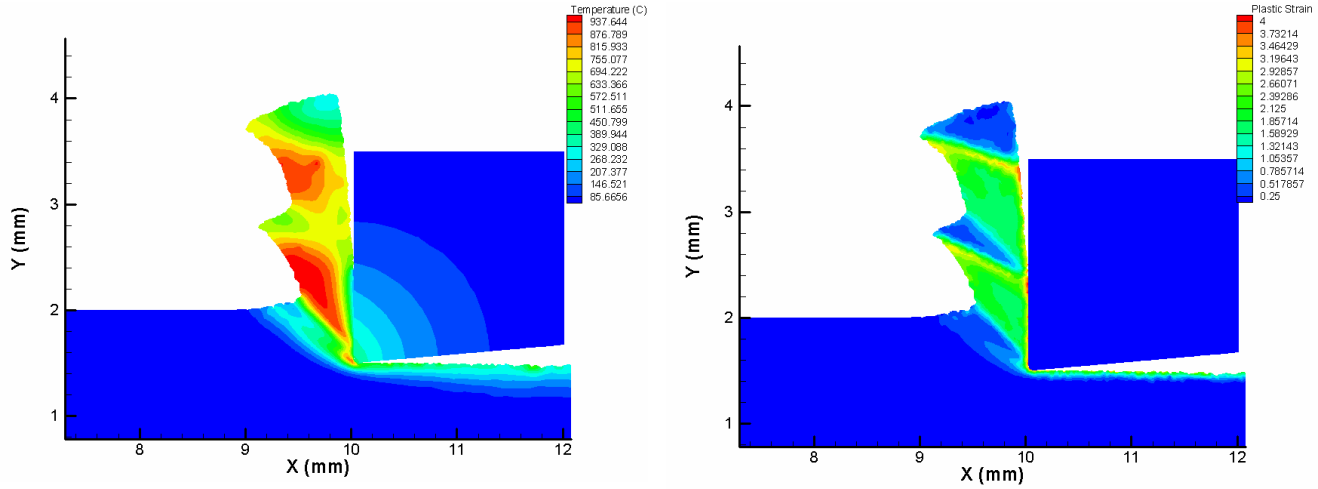

Fig. 7.13 Temperature and equivalent plastic strain contour plots in the chip formed in machining simulation of Ti 6Al-4V for a depth of cut of 0.5 mm and a cutting speed of 5 m/min using a 0° rake angle tool.

At very low speeds, thermo-mechanical instability is weak and heat generated in the shear plane has more time to diffuse. Hence localized increase in temperature necessary for thermal softening is not available. Therefore from this study, it can be concluded that the cutting speed for the onset of shear localization is 5 m/min for depth of cut of 0.5 mm and 10 m/min for depth of cut of 0.25 mm using a 0° rake angle tool. As Recht's thermoplastic shear instability criterion does not simulate shear-localized chip formation accurately at speeds less than 10 m/min in Ti 6Al-4V alloys, other mechanisms such ductile fracture may be responsible for the instability and shear-localized chip formation. This ductile fracture mechanism is an extremely complex phenomenon dependent on the microstructure of the material in combination with the stress and strain states developed during the deformation process. If the crack formed in the primary deformation zone during the cutting process propagates from the free surface of the workpiece, a segmented chip is obtained. For a given material, crack initiation and propagation are very much

dependent upon the level of the hydrostatic stress, shear stress and maximum principal stress in the primary deformation zone.

As the effect of cutting speed is observed for two different depths of cut of 0.25 and 0.5 mm, the effect of increase in depth of cut can be seen from the same figures: Fig.7.7, Fig.7.8, Fig.7.9, Fig.7.10, Fig.7.14, and Fig.7.15. Shear zone temperature and rake face temperatures increase with the increase in depth of cut. The increase in the equivalent plastic strain is not so high when compared to increase in strain rate when the depth of cut is doubled. The average cutting and thrust forces are almost doubled and the power consumption increases for increase in depth of cut from 0.25 to 0.5 mm.

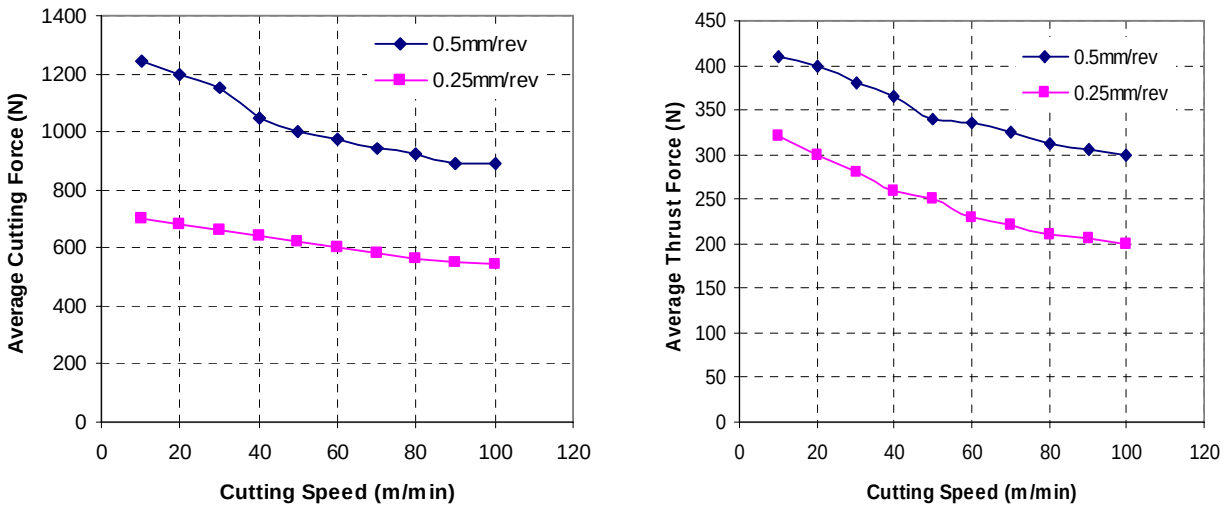

(a) (b)

Fig. 7.14 Effect of cutting speed on (a) average cutting force and (b) average thrust force for FEM simulations of Ti 6Al-4V at cutting speeds from 10 to 100 m/min for two different depths of cut of 0.25 and 0.5 mm, respectively .

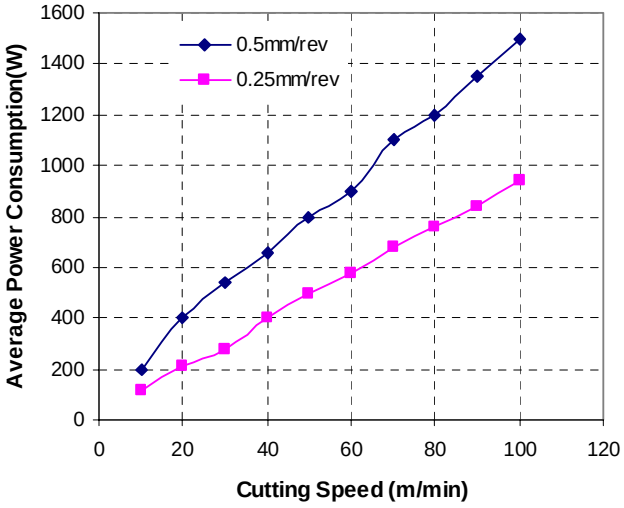

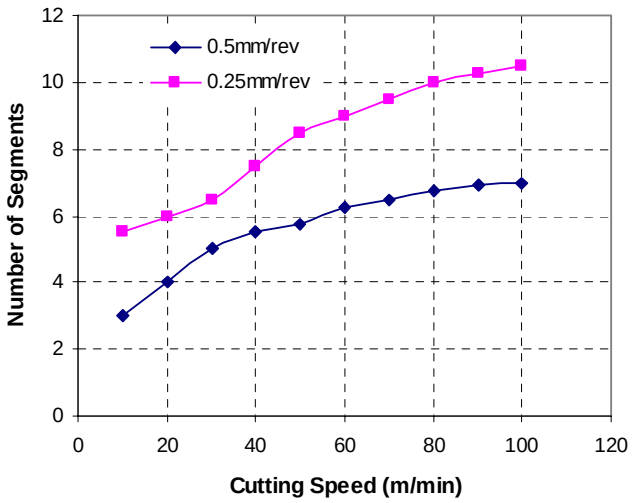

(a) (b)

Fig. 7.15 Effect of cutting speed on (a) average power consumption and (b) number of segments for FEM simulations of Ti 6Al-4V at cutting speeds from 10 to 100 m/min for two different depths of cut of 0.25 and 0.5 mm, respectively.

Whereas number of segments formed for a given value of speed decrease with the increase in depth of cut because more time is needed for thermo-mechanical instability to reach and catastrophic shear failure to occur. As the depth of cut increases from 0.25 mm to 0.5 mm, the cutting speed for the onset of shear localization decreases from 10 to 5 m/min. The degree of chip segmentation is more at 0.5 mm depth of cut when compared to that of 0.25 mm.

7.6 Effects of Rake angle

Finite element simulations are performed for 30 m/min cutting speed and 0.5 mm depth of cut using different rake angles of -15°, 0°, 15°, 30° and 45° to study the effect of rake angle on rake face temperature, shear zone temperature, cutting forces, equivalent

plastic strain, and strain rate. Figs.7.16 (a) to (e) shows the contour plots of temperature and equivalent plastic strain of segmented chip for different rake angles. It is observed that as the rake angle increases from -15° to 45°, the chip formed varies from segmented to continuous chip. Use of negative rake angles leads to increase in tool-chip contact area and higher chip volume. The chip has to be more deformed, requiring more work to be done on it and more pressure on the tool face. Both of these lead to increase in cutting forces and heat generation in shear band. Hence, with -15° rake angle, contact area between any two segments is relatively less leading to deep chip segments are formed and high strain localization (>600%) is seen in narrow shear bands. As the tool rake angle increases from -15° to 45°, Fig.7.17 (a) shows that shear zone temperatures decrease sharply. This is due to weak thermoplastic instability as strain localization is not imminent. The cutting force and thrust force decreases with the increase in the rake angle. For positive rake angle the main force is slightly downward, canceling out some of the upward force due to friction. In fact, with high positive rake angles we can get downward force to dominate so that the forces are actually pulling the tool into the workmaterial. Fig.7.17 (d) shows that, at high positive rake angles, the thrust force is negative. As the thrust force is needed to keep the tool in the workpiece, when the thrust force becomes negative, tool is pulled into the workpiece. Also it is observed from the simulation for 45° rake angle that the simulation aborts after a cutting length of 2.0 mm due to tool penetration into the workmaterial.

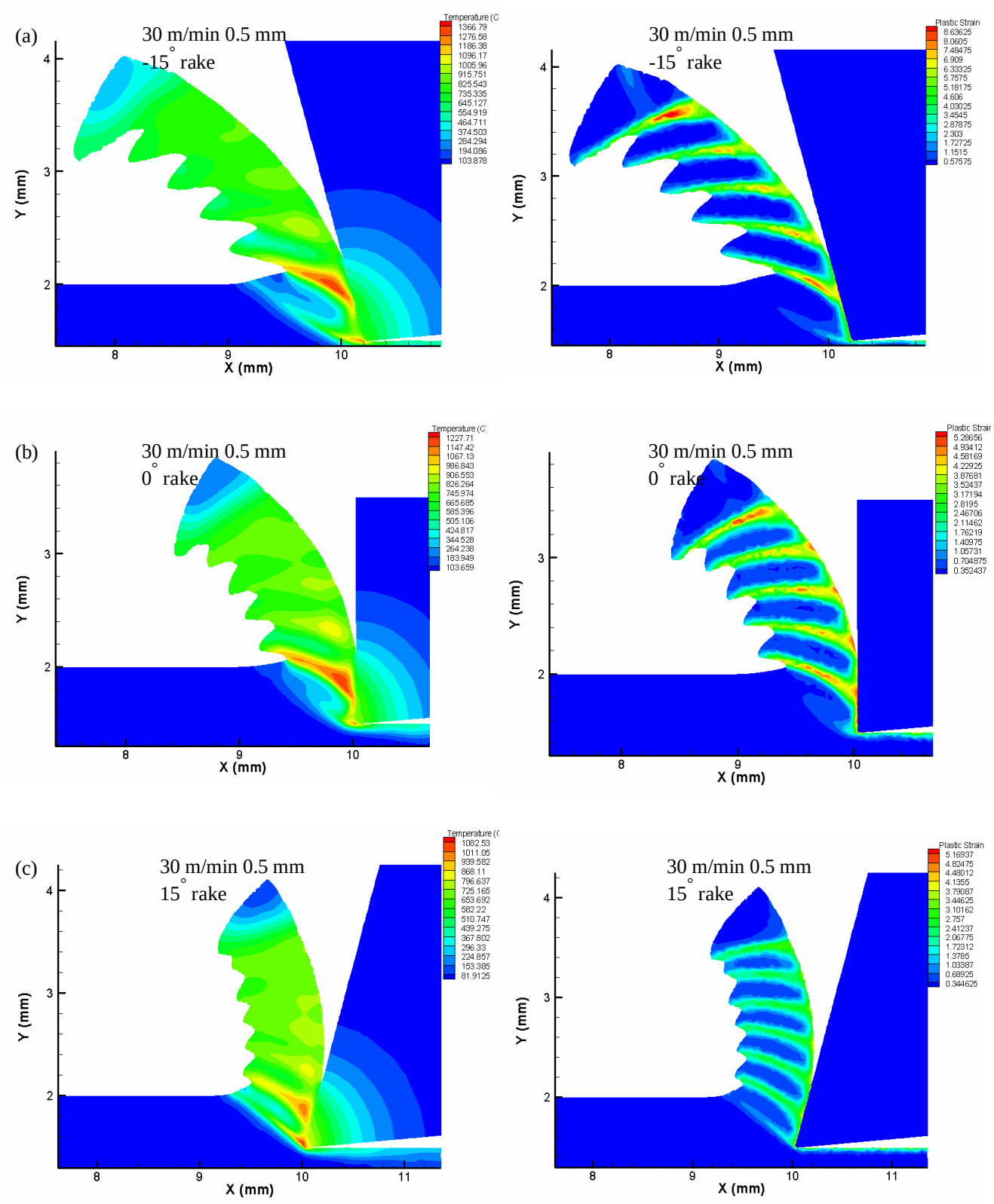
(a)
30 m/min 0.5 mm
-15° rake
Temperature (C
1366.79
1276.58
1186.38
1096.17
1005.96
915.751
825.543
735.335
645.127
554.919
464.711
374.503
284.294
194.086
103.878
Plastic Strain
8.63625
8.0605
7.48475
6.909
6.33325
5.7575
5.18175
4.606
4.03025
3.4545
2.87875
2.303
1.72725
1.1515
0.57575
(b)
30 m/min 0.5 mm
0° rake
Temperature (C
1227.71
1147.42
1067.13
986.843
906.553
826.264
745.974
665.685
585.396
505.106
424.817
344.528
264.238
183.949
103.659
Plastic Strain
5.28656
4.93412
4.58169
4.22925
3.87681
3.52437
3.17194
2.8195
2.46706
2.11462
1.76219
1.40975
1.05731
0.704875
0.352437
(c)
30 m/min 0.5 mm
15° rake
Temperature (C
1082.53
1011.05
939.582
868.11
796.637
725.165
653.692
582.22
510.747
439.275
367.802
296.33
224.857
153.385
81.9125
Plastic Strain
5.16937
4.82475
4.48012
4.1355
3.79087
3.44625
3.10162
2.757
2.41237
2.06775
1.72312
1.3785
1.03387
0.68925
0.344625
Y (mm)
X (mm)

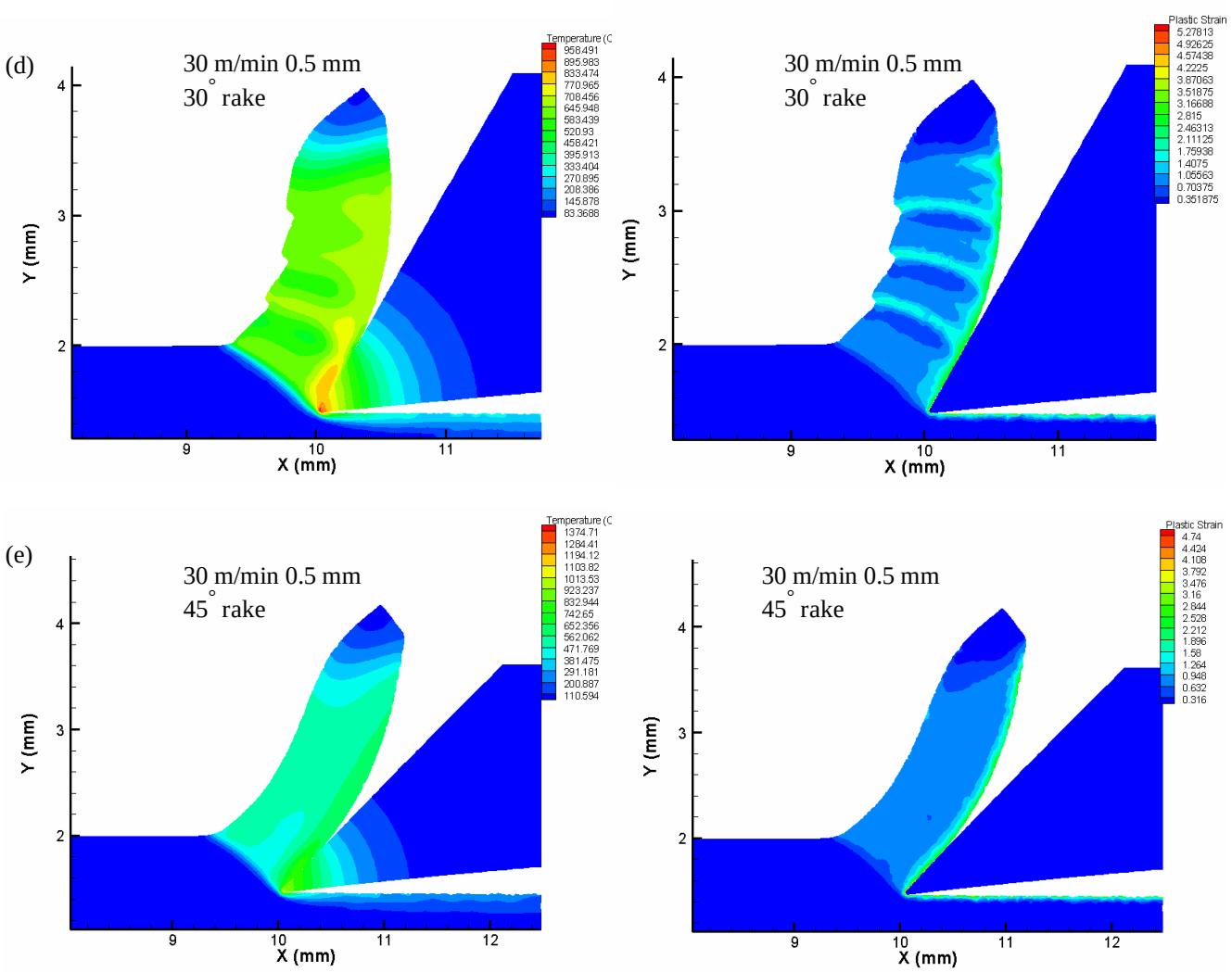

Fig. 7.16 Temperature and equivalent plastic strain contour plots in chip segmentation in machining simulations of Ti 6Al-4V for a depth of cut of 0.5 mm at a cutting speed of 30 m/min using different rake angles of -15°, 0°, 15°, 30° and 45°.

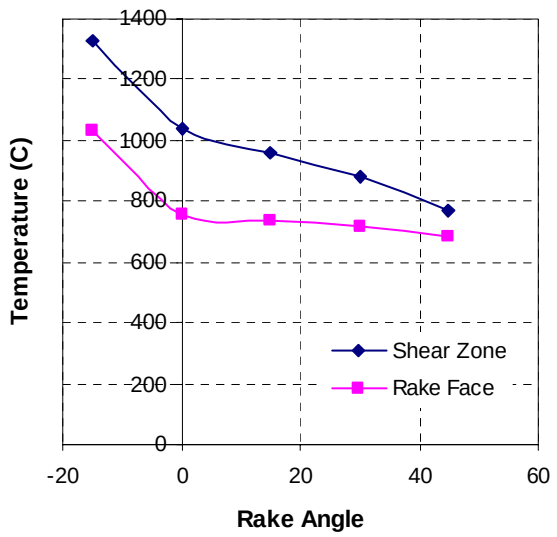

(a)

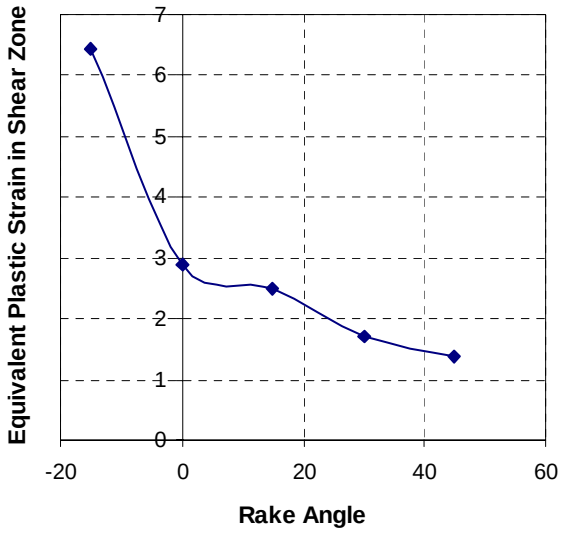

(b)

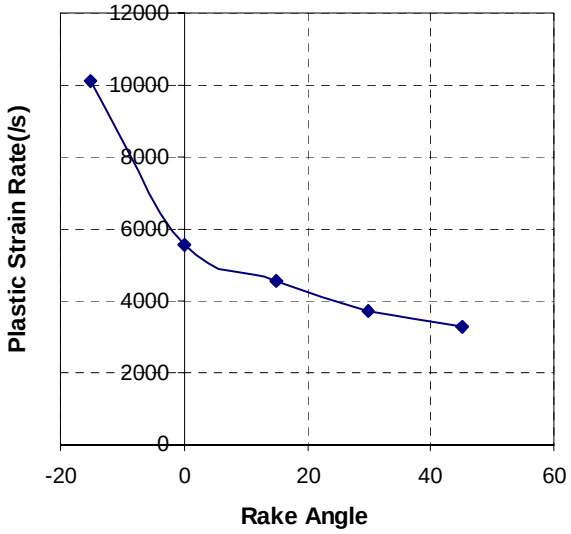

(c)

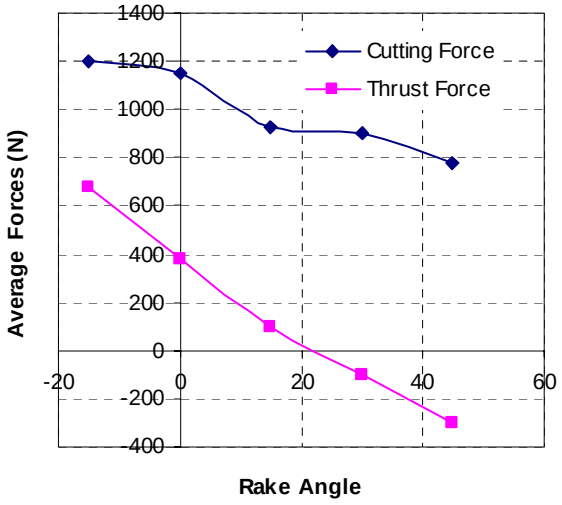

(d)

Fig. 7.17 Effect of rake angle on (a) shear zone and rake face temperatures (b) equivalent plastic strain in the shear zone (c) plastic strain rate and (d) cutting forces for FEM simulations of Ti 6Al-4V at cutting speed 30 m/min and depth of cut of 0.5 mm.

7.7 Effects of Coefficient of friction

Figs.7.18 (a) to (d) shows that using higher friction coefficients causes stagnation of the chip in the secondary deformation zone and as the value of friction coefficient increases, the curvature of the chip decreases. The increase in rake face temperature is more than increase in the shear zone temperature, which can be seen from Fig.7.19, as the value of friction coefficient increases. This is due to high strain gradients in the rake face region caused by sticking contact of the chip with the tool's rake face near the tool tip. From the Fig.7.20 (b) can be seen that as the value of coefficient of friction increases, the cutting force also increases because of increased resistance due to friction along the tool-chip interface. However, no appreciable increase in thrust force is noticed. It can be concluded that with the increase in the value of coefficient of friction, increase in equivalent plastic strain and temperature in shear zone is observed leading to decrease in contact between any two segments to a certain extent.

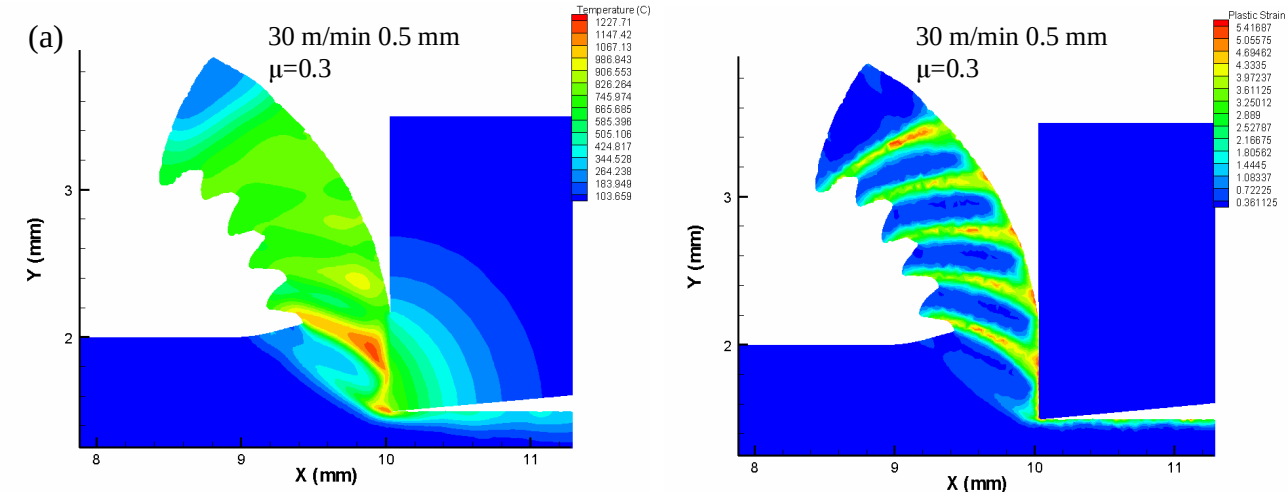

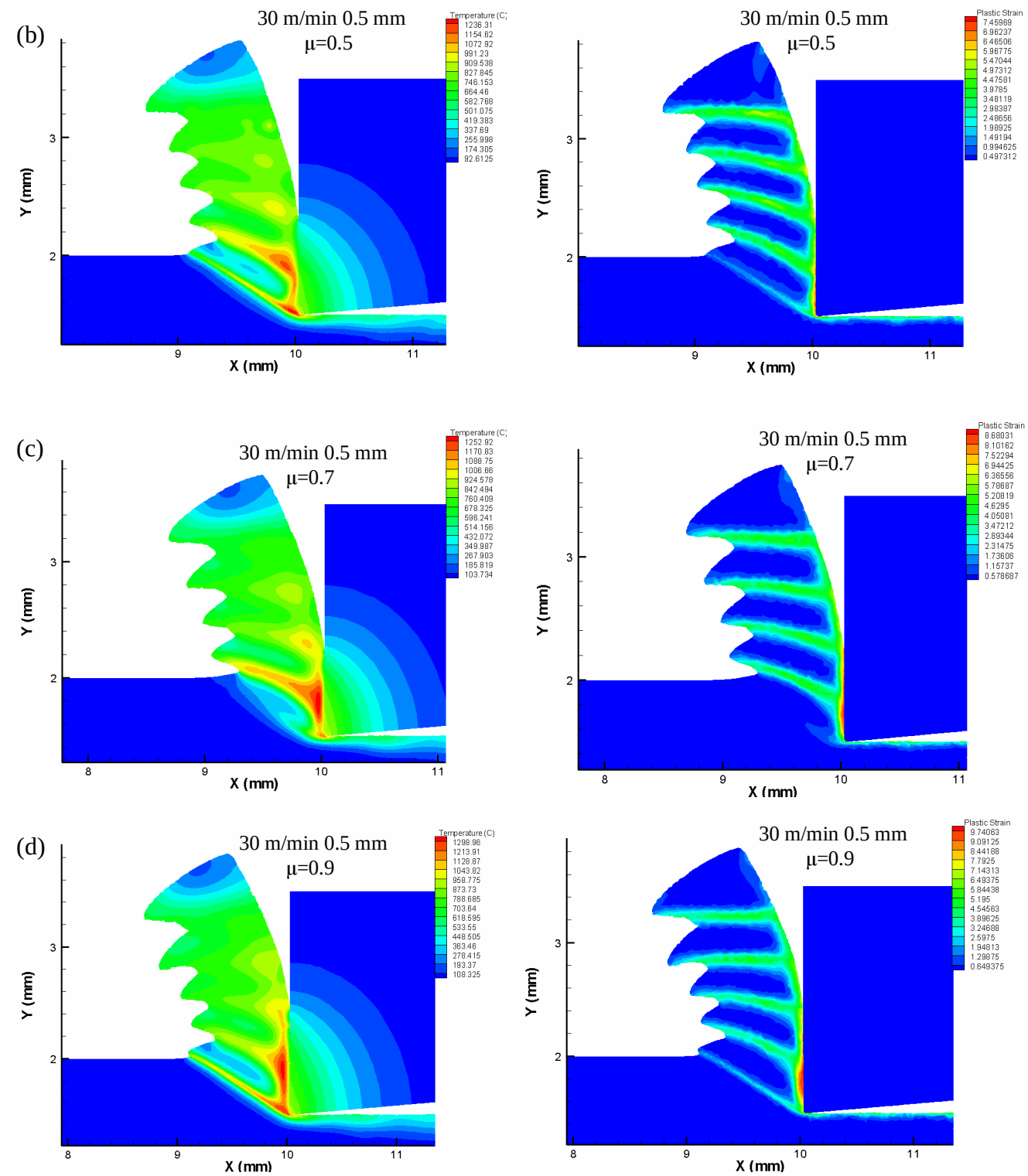

Fig. 7.18 Temperature and equivalent plastic strain contour plots in chip segmentation in machining simulations of Ti 6Al-4V for a depth of cut of 0.5 mm and cutting speed of 30 m/min using different friction coefficients (0.3, 0.5, 0.7, 0.9).

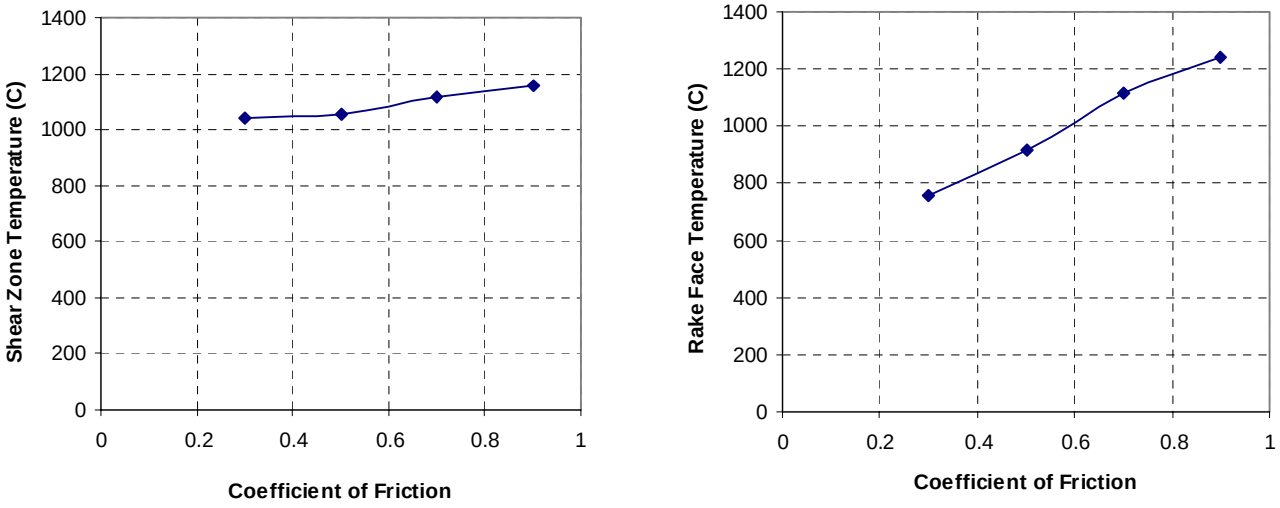

(a) (b)

Fig. 7.19 Effect of friction coefficient on (a) shear zone temperature and (b) rake face temperature for FEM simulations of Ti 6Al-4V at a cutting speed of 30 m/min and depth of cut of 0.5 mm.

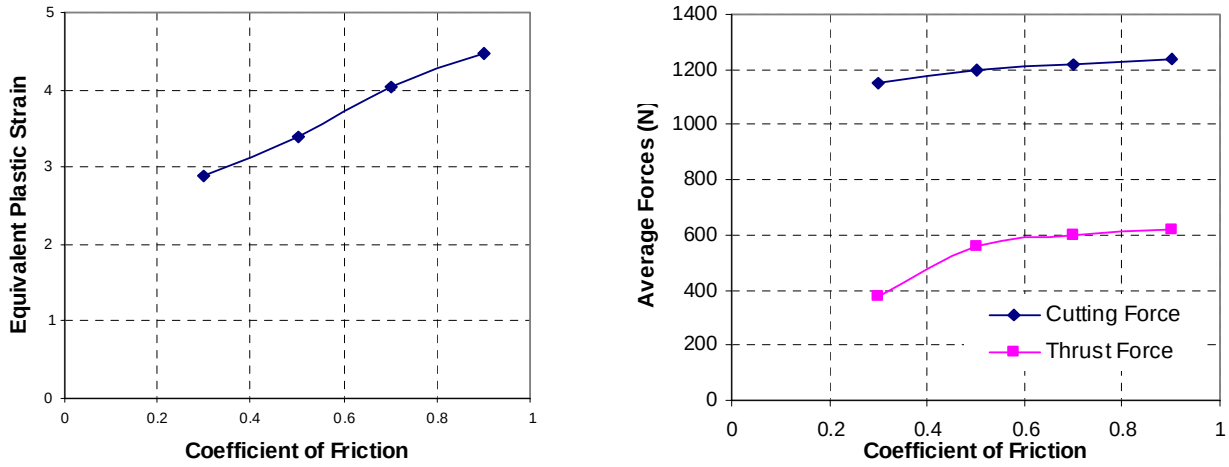

(a) (b)

Fig. 7.20 Effect of friction coefficient on (a) equivalent plastic strain and (b) average cutting forces for FEM simulations of Ti6Al4V at a cutting speed 30 m/min and a depth of cut of 0.5 mm.

7.8 Validation of Simulation Results

Orthogonal machining of Ti 6Al-4V alloy is simulated using 2D explicit AdvantEdge™ simulation software. However, the material model and failure criterion available in the software is not used because the failure criterion for chip segmentation used in the software is based on crack propagation while in the present investigation chip segmentation occurs due to adiabiatic shear failure. Therefore, Johnson-Cook material model and Recht's catastrophic shear failure criterion are incorporated into the software. Hence, it is necessary to validate the simulations with experimental results in order to verify the accuracy of the code developed and the reliability of the material model. In this investigation, only finite element simulations are conducted and as actual machining of Ti 6Al-4V is not done, the experimental data is taken from the literature review for validation.

As mentioned in the literature review, Klocke *et al.* [1] conducted cutting tests of Ti 6Al-4V to investigate the influence of cutting parameters on surface integrity properties with special regard to its transfer to real machining operations. They used a carbide tool (rake angle and clearance angle of the tool used was 0° and 11°, respectively) at a cutting velocity of 200 m/min for different feed rates of 0.02, 0.05, 0.075 and 0.1 mm/rev. They measured the average cutting force and average thrust force.

Finite element simulations are performed using these same cutting conditions and comparisons of the average cutting forces and thrust forces are made with the experimental results. The values of average cutting and thrust forces of both simulations and experiments are listed in Table. 7.6. It can be noted that the experimental values of average cutting and average thrust force are lower than that of the simulation values.

While the percentage deviation between simulation and experiment values is less for medium and high depths of cut, higher values are found for low depths of cut.

Table 7.6 Finite element simulation results and experimental data [1] of cutting and thrust force with percent deviation

Feed rate 0.02mm/rev			
	FEM	**Experiment**	**% Deviation**
Cutting force (Fx) in N	50	38	31.58
Thrust Force (Fy) in N	28	24	16.67
Feed rate 0.05mm/rev			
	FEM	**Experiment**	**% Deviation**
Cutting force (Fx) in N	124	118	5.08
Thrust Force (Fy) in N	49	47	4.25
Feed rate 0.075mm/rev			
	FEM	**Experiment**	**% Deviation**
Cutting force (Fx) in N	155	145	6.89
Thrust Force (Fy) in N	64	59	8.47
Feed rate 0.1mm/rev			
	FEM	**Experiment**	**% Deviation**
Cutting force (Fx) in N	188	178	5.61
Thrust Force (Fy) in N	90	88	2.27

The percentage deviation of both the forces lies within 10% for feed rates 0.05, 0.075 and 0.1mm/rev. For the smallest feed rate used within the test series, 0.02mm/rev, the percentage deviation rises to about 30% which demonstrates that for simulations related to small feed rates a new improved modeling approach is needed.

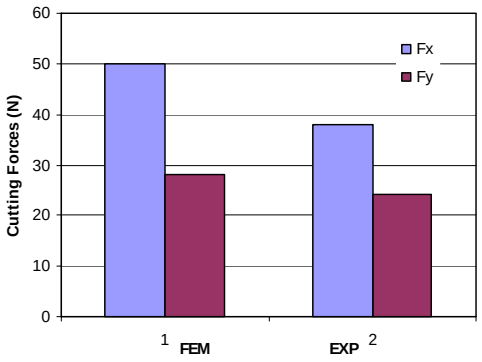

Feed rate 0.02 mm/rev

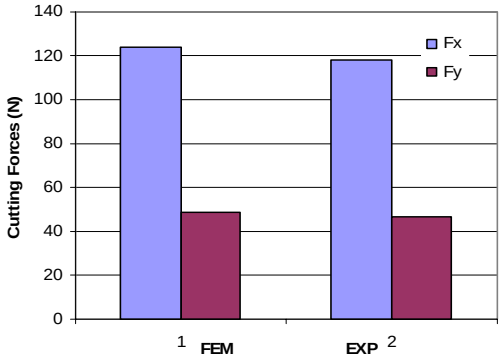

Feed rate 0.05 mm/rev

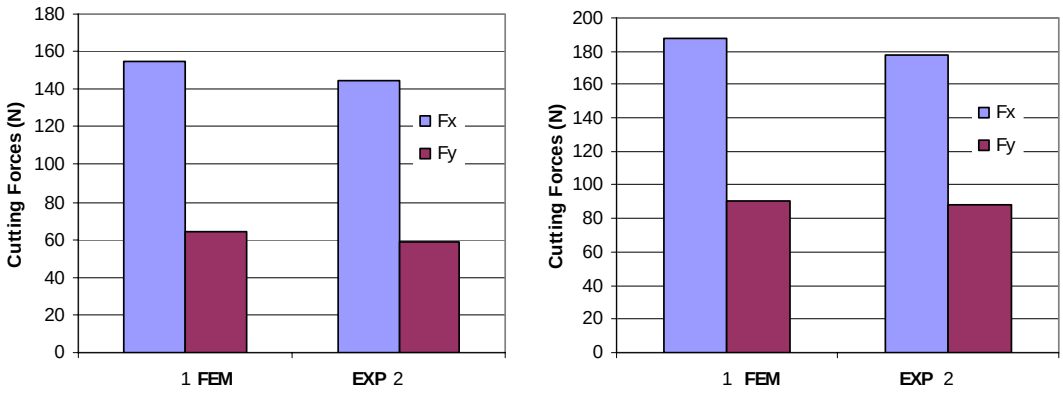

Feed rate 0.075 mm/rev Feed rate 0.1 mm/rev

Fig. 7.21 FEM and experimental results [1] of cutting and thrust force compared for feed rates 0.02, 0.05, 0.075, 0.1mm/rev

Fig.7.21 compares cutting forces F_x and F_y from finite element simulations and measured cutting forces for a range of feed rates from 0.02 to 0.1mm/rev.

As mentioned in the literature review, Shivpuri *et al.* [21] studied shear-localized chip formation in Ti 6Al-4V using finite element simulations and turning experiments. Finite element simulations were conducted using a commercial software, DEFORM 2D™ while turning experiments were conducted on a CNC turning center at cutting speeds of 60, 120 and 240 m/min, feeds of 0.127 and 0.35 mm/rev and a depth of cut of 2.54 mm. In this investigation, finite element simulations are performed for the above mentioned cutting conditions and a comparison of cutting forces was made with their experimental data. The values of the cutting forces are listed in Table.7.7 and a comparison with experimental data is shown in Fig.7.22. It is observed that the maximum percent deviation in force magnitudes between experimental data and simulated values is ~12.5%. This percent deviation is in the acceptable range providing a good validation for

the FEM model. Thus, it can be concluded that the above two validations of cutting forces with satisfactory accuracy validates the numerical model used in this study.

Table 7.7 Finite element results and experimental data [21] for cutting force with percent deviation

Feed rate 0.127mm/rev			
Cutting speed (m/min)	**Average Cutting force (N/mm)**		
	Experiment	**FEM**	**Percent Deviation**
60	240	270	12.50
120	230	255	10.86
240	----	250	-----
Feed rate 0.350mm/rev			
Cutting speed (m/min)	**Average Cutting force (N/mm)**		
	Experiment	**FEM**	**Percent Deviation**
60	610	660	8.19
120	600	640	6.67
240	590	625	5.93

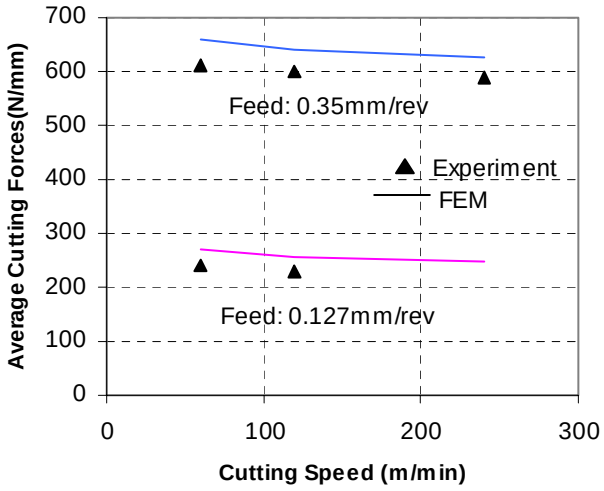

Fig. 7.22 Results of cutting forces obtained from FEM simulations compared with experimental data [21] for feed rates 0.127 and 0.35 mm/rev.

As mentioned in the literature review, Barry *et al.* [29] conducted orthogonal machining tests to investigate the mechanisms of shear-localized chip formation in the

machining of Ti 6Al-4V alloy at different cutting speeds (15, 30, 60, 120, 180 m/min) and feed rates (0.02, 0.04, 0.06, 0.08 and 0.1 mm/rev). The main feature in their study was the use of acoustic emission (AE) to elucidate the phenomena occurring within the chip formation zone(s). Finite element simulations are conducted in the present investigation with a cutting speed of 180 m/min and depths of cut of 0.04, 0.06, 0.08 and 0.1 mm with all other machining parameters the same as that used by Barry et al. [29] in their cutting tests. The chip morphology is compared as shown in the Fig.7.23. All the chips can be classified as either periodic or aperiodic shear-localized chips. With low values of depths of cut, such as 0.02 and 0.04 mm, aperiodic shear-localized chips are produced and an increase in this parameter results in a transition from aperiodic to periodic shear-localized chip formation. From Fig. 7.23 it can be seen that for a depth of cut of 0.04 mm shear-localized chip is not formed during the simulation unlike in machining tests. The reason behind this is for low feed rates of few microns, instability criterion is weak and strain is evenly distributed in the chip without getting localized in a narrow shear band.

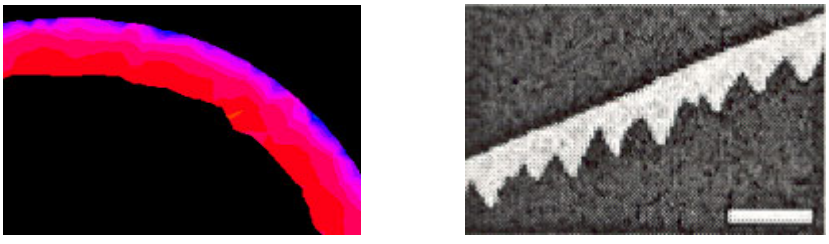

Depth of cut 0.04 mm

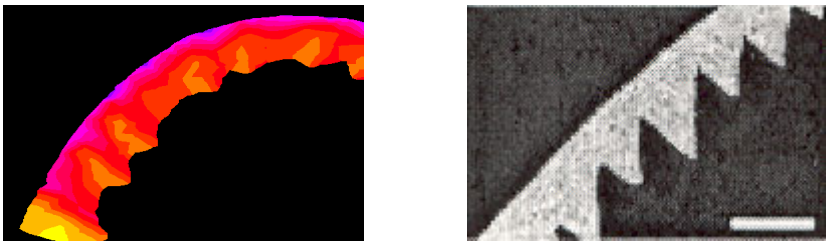

Depth of cut 0.06 mm

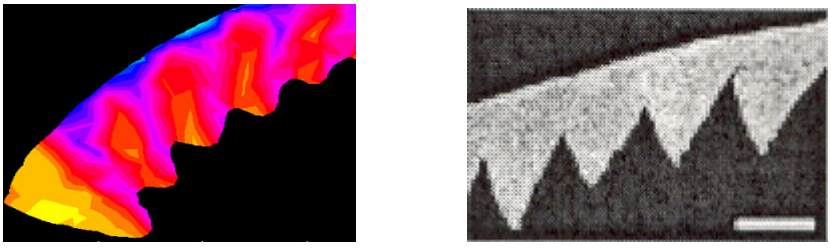

Depth of cut 0.08 mm

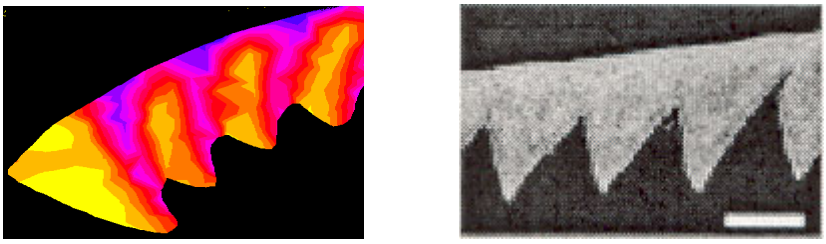

Depth of cut 0.1 mm

Fig. 7.23 Results of chip comparison from FEM simulations and experimental data [29] for 180 m/min cutting speed and depths of cut of 0.04, 0.06, 0.08, and 0.1mm.

Hence, a new improved modeling approach is needed for very low depth of cut simulations. It can also be noted from Fig.7.23 that the segments in the chip morphology obtained from the simulations are relatively not sharp and deep when compared with the experimental ones. This is because in the case of these simulations, when workpiece material flows around the cutting tool edge, at the tool vicinity elements get distorted and loose accuracy. In order to alleviate this element distortion, finite element mesh is updated periodically, refining large elements, remeshing distorted elements and

coarsening smaller elements. From a comparison from Fig.7.23, a reasonably good agreement can be seen between finite element simulated chips and the experimental ones.

As mentioned in the literature review, Molinari *et al.* [28] carried out experimental analysis of shear localization and chip segmentation in Ti 6Al-4V exploring cutting speeds in a range from 0.01 to 73 m/s. Chip morphology obtained for a cutting speed of 1.2 m/s and depth of cut of 0.5 mm from the experimental work of Molinari et al. [28] is compared with that of the simulation conducted in this study, as shown in Fig.7.24. It can be seen that the segments are relatively not sharp and deep in case of chip morphology obtained from the simulation and as mentioned previously, this could be due to adaptive remeshing and mesh refinement process.

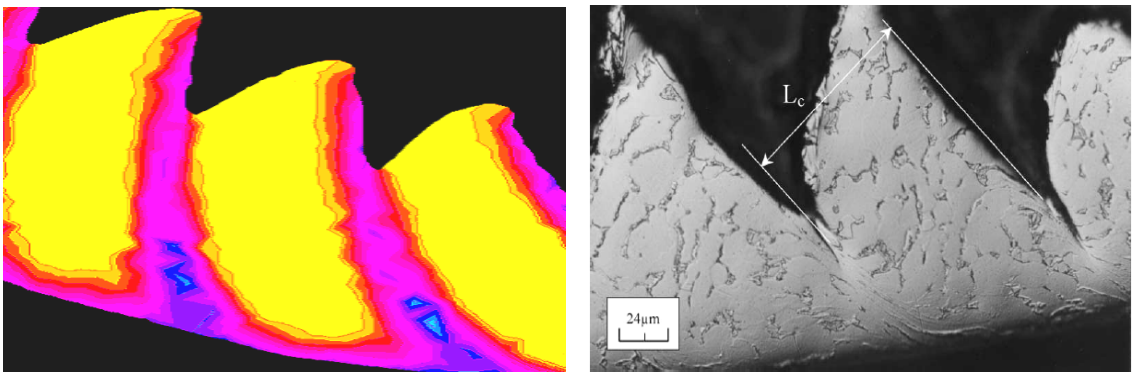

Fig. 7.24 Results of chip morphology from FEM simulation conducted at 1.2 m/s and 0.5 mm depth of cut compared with that of experimental data [28]

These validations thus show close agreement of the simulation results with the experimental data validating the user subroutine developed. Thus, accurate study of shear-localized chip formation in machining Ti 6Al-4V can be done using this commercial finite element software AdvantEdge™ along with the incorporated user-defined subroutine UMAT.

7.9 Discussion

In this investigation, it was found that shear-localized chips form at low cutting speeds starting from 10 m/min and below for a depth of cut of 0.25 mm and this type of chip continues over the conventional cutting speed range. Finite element simulations were conducted for cutting speeds below 10 m/min at depths of cut of 0.25 and 0.5 mm using a 0° rake angle tool. No shear localization is observed and continuous chip is formed in the case of 0.25 mm depth of cut whereas with 0.5 mm depth of cut, shear-localized chip formation is observed to form at a cutting speed of 5 m/min. However, using higher depths of cut (>0.5 mm) shear localization can be observed even below 5 m/min cutting speed. At higher cutting speeds, shear localization appears to be due to the occurrence of thermo-plastic shear instability within the primary shear zone. The nature of instability, frequently referred to as adiabatic shear, is one in which the rate of thermal softening exceeds the rate of strain hardening. While true adiabatic shear (no heat loss) is not possible, the term is frequently used in reference to thermally softened shear zones. While at very low cutting speeds, strain localization and thermally softened shear zones are not observed as the high temperatures generated in the primary shear zone have enough time to diffuse into the chip material. Hence, this instability criterion cannot explain the formation of shear-localized chip in Ti 6Al-4V for very low cutting speeds. Komanduri and Hou [25] employed Recht's basic model of thermo-plastic shear instability [12] to calculate the critical cutting speed for the onset of shear-localization in Ti 6Al-4V. They found that the onset of the critical cutting speed for shear localization is different for different depths of cut used and for Ti 6Al-4V it is extremely low

(~0.42m/min for a depth of cut of 0.2mm). However, at very low cutting speeds, crack initiation within the primary shear zone might play an important role in chip segmentation than thermo-plastic instability.

In this study, Recht's catastrophic shear instability criterion is incorporated into the user subroutine along with Johnson-Cook material model to simulate shear-localized chip formation in machining Ti 6Al-4V alloy. Validations of the simulations are done by comparing the cutting forces and chip morphology obtained from the simulations with that of the experimental data available in the literature. The chip morphology obtained from simulations show a close resemblance with the chip segments from the experimental data and the cutting forces also show a close match validating the code. The mechanism involved in the segmented chip formation is studied with the simulation results at different time steps and it is observed that two stages are involved, as originally proposed by Komanduri and von Turkovich [11]. In the first stage, plastic instability and strain localization occurs in a narrow band in the primary shear zone leading to catastrophic shear failure. The other stage involves gradual build up of the segment with negligible deformation by the flattening of the wedge-shaped work material ahead of the advancing tool.

The effect of cutting speed and feed rate on the chip segmentation is studied and it is observed that as the cutting speed increases, high strain localization occurs with large temperatures concentrated in narrow shear bands (due to poor thermal properties of the work material) leading to strong thermo-plastic instability and increase in the number of chip segments. Whereas with increase in depth of cut, the chip segments are found to be deep and sharp and the critical velocity for the onset of chip segmentation is less. By

varying the rake angles from -15° to 45° with constant speed and depth of cut, change in chip form from segmented to continuous is observed. And appreciable change in the chip segments is not observed and with the increase in the coefficient of friction, however the segments are found to go deep and sharp to certain extent.

Recht's catastrophic shear failure criterion along with Johnson-Cook material model was incorporated into user subroutine VUMAT of commercial FEM code ABAQUS/Explicit. Finite element simulations were carried out using different cutting speeds and 0.25mm depth of cut with a rigid tool. But these finite element simulations were not successful as these simulations used to hang without running. The reason might be the temperature increment which was not noticed in the result. Hence, this work is not discussed in detail in this study.

CHAPTER 8

CONCLUSIONS AND FUTURE WORK

8.1 Conclusions

In order to overcome the machinability issues associated with machining Ti6Al4V, an attempt has been made in this study to observe the effect of machining conditions on the chip formation, rake face and shear zone temperatures and cutting forces. The following are specific conclusions that may be drawn from this investigation:

1. An extensive literature review has been made to investigate finite element simulations of segmented chip formation in machining Ti 6Al-4V alloy. It is observed that most of the work reported lack proper experimental validations, reliable material model, accurate failure criterion to simulate the mechanism of chip segmentation and low speed machining simulations (<10 m/min). And the methodology used by many researchers using non-commercial FEM codes makes it difficult for end-users.

2. Finite element simulations of orthogonal machining of Ti 6Al-4V alloy are conducted in this study using a commercial FEM software, AdvantEdge™. This software uses 2-dimensional, explicit, Lagrangian formulation code with mesh adaptivity and

adaptive remeshing techniques. However, the material model and failure criterion used in this software is not applied to simulate shear-localized chip formation.

3. From the literature review, it is found that Johnson-Cook material model accurately represents the material deformation behavior for high strain rates and high temperatures and Recht's catastrophic shear failure criterion explains the proper mechanism of chip segmentation.
4. AdvantEdge™ has the facility to incorporate user-defined material subroutine (UMAT). Using this, Johnson-Cook material model and Recht's catastrophic shear failure criterion are incorporated into the UMAT subroutine code. This subroutine code is linked to the main code of the software.
5. Finite element simulations were conducted for a range of cutting speeds (from 10 m/min to 100 m/min) and two different depths of cut (0.25 and 0.5 mm) with constant coefficient of friction 0.3, depth of cut 1.0 mm and length of cut 3.0 mm. Effect of cutting speed and depth of cut on chip segmentation is studied. It is observed that as the cutting speed increases, rake face temperatures, shear zone temperatures, equivalent plastic strain in the shear zone, plastic strain rate, average cutting force, average thrust force, and power consumption increases. It is also observed that with increase in the cutting speed the number of chip segments for a given length of cut increases.
6. With the depth of cut doubled from 0.25 to 0.5 mm, the values of rake face temperatures, shear zone temperatures, equivalent plastic strain in shear zone, plastic strain rate, average cutting force, average thrust force and power consumption also

show an increase. The chip segments are relatively sharp and deep and the cutting speed for the onset of chip segmentation decreases with increase in feed rate.

7. Finite element simulations are also performed for 30 m/min cutting speed, 0.5 mm depth of cut, 0.3 coefficient of friction, 3 mm length of cut and varying rake angles from -15° to 45°. It is observed that by increasing the rake angle from -15° to 45° the chip form changes from segmented to continuous chip, the average cutting and thrust forces, the shear zone temperatures and strains decrease.

8. The coefficient of friction is varied from 0.3 to 0.9 and the simulations are carried out for 30 m/min cutting speed and 0.5 mm depth of cut. Rake face temperatures and cutting forces are observed to increase appreciably. Curvature of the chip is found to decrease with increase in coefficient of friction due to stagnation of the chip in the secondary deformation zone. Moreover, the contact between any two segments decreases to a certain extent.

9. In this investigation the mechanism of chip segmentation is studied by taking the snapshots of the chip at different time steps. It is observed that the mechanism is essentially the same as that described by Komanduri and von Turkovich [11] based on the experimental studies of machining Ti 6Al-4V.

10. The cutting speed for the onset of chip segmentation from this study is found to be 10 and 5 m/min for 0.25 and 0.5 mm depths of cut respectively with a 0° rake angle tool.

8.2 Future Work

1. A new ductile failure criterion has to be incorporated into the user subroutine (UMAT) to simulate the shear-localized chip formation in case of Ti 6Al-4V for cutting speeds less than 10 m/min. The crack which determines the shear-localized chip during cutting always occurs in the primary deformation zone on the free surface of the chip and propagates toward the tool tip where the maximum principal stress and shear stress are located. Shear stress in the shear plane and the tensile stress facilitate the initiation of the crack.
2. Conventional material models used in the finite element simulations, which represent material deformation behavior under stress, strain and temperature does not determine flow stress uniquely as they lack estimation of metallurgical phenomenon occurring in the workpiece material during the metal cutting process as well as previous deformation history. Yoshino et al. [41] proposed a new flow stress equation for Ti 6Al-4V alloy which involves a new index of deformation history. The equation is not only available to arbitrary deformation history but also provides metallurgical information through a forming process. This flow stress equation appears to be superior to conventional one as it estimates the effect of recovery in the calculation of deformation energy. Finite element simulations incorporating this material model may enable us to study accurately the chip formation process and machinability issues in machining Ti 6Al-4V alloy.

3. The main problems associated with the machining Ti 6Al-4V alloy are lower tool life and the permissible rates of material removal are low, inspite of the low tool forces. It is the high temperatures and unfavorable temperature distributions over the rake face and in the cutting tool that are responsible for this. A typical form of wear in the cutting tools used in machining titanium alloys is crater wear that forms on the rake face of the cutting tool at a short distance from the cutting edge. It is believed that dissolution-diffusion is the main cause for crater wear. Usui et al. [42] derived a characteristic equation of crater wear theoretically using Shaw's equation of adhesive wear. AdvantEdge™ has an inbuilt code to simulate tool wear using finite element analysis. As Usui's tool wear model accurately predicts the crater wear in the tools used for machining titanium alloys, this model can be incorporated into the user subroutine code and the wear constants of the model can be determined with the aid of predicted temperatures on the rake face, stresses on the tool face and measured tool wear by curve fitting to model the tool wear.

REFERENCES

1. Van Luttervelt, C.A., Childs, T.H.C., Jawahir, I.S., and Klocke, F., "Modeling of machining operations," Annals CIRP 47 (1998) 587-626.
2. Childs, T.H.C., Maekawa, K., Obikawa, T., and Yamane, Y., "Metal Machining Theory and Applications," Arnold, London, (2000).
3. Usui, E. and Shirakashi, T., "Mechanics of Machining from descriptive to predictive theory. In on the Art of Cutting Metals - 75 years later," ASME PED 7 (1982) 13-35.
4. Iwata, K., Osakada, K., and Terasaka, Y., "Process modeling of orthogonal cutting by the rigid-plastic finite element method," Journal of Engineering Materials Technology 106 (1984) 132-138.
5. Strenkowski, J. and Carroll, J., "A finite element model of orthogonal metal cutting," Journal of Engineering for Industry 107 (1985) 347-354.
6. Black, J.T., "On the fundamental mechanism of large deformation: Electron microscopy of metal cutting chips," Journal of Engineering for Industry (1971) 507-526.
7. Ezugwu, E.O. and Wang, Z.M., "Titanium alloys and their machinability-a review," Journal of Materials Processing Technology 68 (1997) 262-274.

8. Ezugwu, E., Bonney, J., and Yamane, Y., “An overview of machinability of aeroengine alloys,” Journal of Materials Processing Technology, 134 (2003) 233-253.

9. Leuser, D., “Experimental investigation of material models for Ti6Al4V and aluminium 2024-T3,” FAA Report DOT/FAA/AR-00/25, (2000).

10. Majorell, A., Srivatsa, S., and Picu, R.C., “Mechanical behavior of Ti6Al4V at moderate and high temperatures-Part I,” Materials Science and Engineering A326 (2002) 297-305.

11. Komanduri, R. and von Turkovich, B.F., “New observations on the mechanism of chip formation when machining titanium alloys,” Wear 69 (1981) 179-188.

12. Recht, R., “Catastrophic thermoplastic shear,” Transactions of ASME 31 (1964) 186.

13. Xie, J.Q., Bayoumi, A.U., and Zbib, H.M., “A study on shear banding in chip formation of orthogonal machining,” International Journal of Machine Tools and Manufacturing 36 (1996) 835-847.

14. Marusich, T. and Ortiz, M., “Modelling and simulation of high speed machining,” International Journal for Numerical Methods in Engineering 38 (1995) 3675-94.

15. Ceretti, E., Lucchi, M., and Altan, T., “FEM simulation of orthogonal cutting: serrated chip formation,” Journal of Materials Processing Technology 95 (1999) 17-26.

16. Cockroft, M.G. and Latham, D.J., “A simple criterion of fracture for ductile materials,” National Engineering Laboratory, UK, Report 216 (1966).

17. Hashemi, J., Tseng, A. A., and Chou, P.C., "Finite element modeling of segmental chip formation in high-speed orthogonal cutting," Journal of Material Science and Engineering 3 (1994) 712-721.

18. Obikawa, T. and Usui, E., "Computational machining of a titanium alloy-finite element modeling and few results, Journal of Manufacturing Science and Engineering 118 (1996) 208-215.

19. Rice, W.B., "The formation of continuous chips in metal cutting," Engineering Journal, Engineering Institute of Canada 44 (1961) 41.

20. Iwata, K., Osakada, K., and Terasaka, Y., "Process modeling of orthogonal cutting by the rigid-plastic finite element method," Journal of Engineering Materials Technology 106 (1984) 132-138.

21. Hua, J. and Shivpuri, R., "Prediction of chip morphology and segmentation during the machining of titanium alloys," Journal of Materials Processing Technology 150 (2004) 124-133.

22. Nakayama, K., "The formation of saw-tooth chips," Proceedings of the International Conference on Production Engineering, Tokyo (1974) 572-577.

23. Owen, D.R.J. and Vaz Jr., M., "Computational techniques applied to high-speed machining under adiabatic strain localization conditions," Computational Methods in Applied Mechanics and Engineering 171 (1999) 445-461.

24. Samiatin, L. and Rao, S., "Shear localization during metal cutting," Material Science and Engineering 61 (1983) 185-192.

25. Komanduri, R. and Hou, Z.B., “On the thermoplastic shear instability in the machining of a titanium alloy (Ti6Al4V),” Metallurgical and Materials Transactions 33A (2002) 2995-3010.

26. Komanduri, R., “Some clarifications on mechanics of chip formation when machining titanium alloys,” Wear 78 (1982) 15-34.

27. Komanduri, R. and Brown, R., “On mechanics of chip segmentation in machining,” Transactions of ASME, Journal of Engineering for Industry 103 (1981) 33-51.

28. Molinari, A., Musquar, C., and Sutter, G., “Adiabatic shear banding in high speed machining of Ti6Al4V: experiments and modeling,” International Journal of Plasticity 18 (2002) 443-459.

29. Barry, J., Byrne, G., and Lennon, D., “Observations on chip formation and acoustic emission in machining Ti6Al4V alloy,” International Journal of Machine tools and Manufacture 41 (2001) 1055-1070.

30. Ribeiro, M.V., Moriera, M.R.V., and Ferreira, J.R., “Optimization of titanium (6Al-4V) machining,” Journal of Materials Processing Technology 143-144 (2003) 458-463.

31. Lee, W.S. and Lin, C.F., “High-temperature deformation behavior of Ti6Al4V alloy evaluated by high-strain rate compression tests,” Journal of Materials Processing Technology 75 (1998) 125-136.

32. Reissig, L., Volkl, R., Mills, M.J., and Glatzel, U., “Investigation of near surface structure in order to determine process temperatures during different machining processes of Ti6Al4V,” Scripta Materialia 50 (2004) 121-126.

33. Lopez de Lacalle, L.N., Perez, J., Llorente, J. I., and Sanchez, J.A., "Advanced cutting conditions of milling aeronautical alloys," Journal of Materials Processing Technology 100 (2003) 1-11.

34. Maekawa, K., Shirakashi, T., and Obikawa, T., "Recent progress of computer aided simulation of chip flow and tool damage in metal machining," Journal of Engineering Manufacture (1995) 233-242.

35. Baker, M., Rosler, J., and Siemers, C., "A finite element model of high speed metal cutting with adiabatic shearing," Computers and Structures 80 (2002) 495-513.

36. Sandstrom, D.R. and Hodowany, J.N., "Modeling the physics of metal cutting in High Speed Machining," Machining Science and Technology 2 (1998) 343-353.

37. AdvantEdge Theory manual, Version 3.3, Third wave systems, Inc., USA, (1998).

38. Engelmann, B. and Hallquist, J.O., "A non-linear two-dimensional finite element code for solid mechanics-user manual," Lawrence Livermore National Laboratory (1991).

39. Bayoumi, A.E. and Xie, J.Q., "Some metallurgical aspects of chip formation in cutting Ti6Al4V," Materials Science and Engineering A190 (1995) 173-180.

40. ABAQUS/Explicit theory manual, Version 6.3, HKS Inc., USA, (2002).

41. Yoshino, M. and Shirakashi T., "New flow-stress equation of Ti-6Al-4V alloy," Journal of Materials Processing Technology 48 (1995) 179-186.

42. Usui, E., Shirakashi, T., and Kitagawa, P., "Analytical prediction of cutting tool wear," Wear 100 (1984) 129-151.

43. www.matweb.com/search/SpecificMaterial.asp?bassnum=MTP641

44. Larsson, M., Arcam, U., and Harrysson, A., "Rapid manufacturing with Electron Beam Melting (EBM)-A manufacturing revolution?," Solid Freeform Fabrication Proceedings (2003) 433-438.

45. Tay, A.O., Stevenson, M.G., and David, G.V., "Using the finite element method to determine temperature distributions in orthogonal machining," Proceedings of the Institution of Mechanical Engineers 188 (1974) 627-638.

46. Zienkiewicz, O.C., "The finite element method in engineering science," McGraw-Hill, London (1971).

47. Narutaki, N. and Murakoshi. A., "Study on machining of titanium alloys," Annals of the CIRP 32 (1983), 65.

48. Hoffmeister, H.W., Gente, A., and Weber, T.H., "Chip formation in titanium alloys under cutting speed of upto 100 m/s," 2nd International Conference on High Speed Machining, PTW Darmstadt University (1999) 21-28.

49. Diack, M.I., "Contribution à l'etude de l' usinage grande vitesse de l'alliage de Titane TA6V," Thesis Doctorat Universite de Nantes (1995).

50. Larbi, S., "Contribution à l'etude de l' usinage à grandes vitesses de materiaux metalliques par simulation sur un banc de essai à base de barris Hopkinson," Thesis Doctorat Universite de Nantes (1990).

APPENDIX

User subroutine code (UMAT) incorporating Johnson-Cook material model and Recht's catastrophic shear failure criterion with stress updated algorithm.

```
C
      SUBROUTINE MAT_USER(sig,dtime,temperature,ql,epsl,d,deps)
c
      !DEC$ ATTRIBUTES DLLEXPORT :: MAT_USER
      implicit real*8 (a-h,o-z)
c
c        Defomation tensor * dtime (strain increment)
c       deps(1,1) = Dxx*dtime, deps(1,2)=Dxy*dtime, deps(2,2)=Dyy*dtime
c
c                Material propeties are read from _wp.twm file
c
c                Researved parameters
c                d(2)           Densitiy (scaled)
c                d(5)           lambda (Lame's constant)
c                d(6)           mu (Lame's constant)
c                d(7)           SIGMA0 (Yield stress)
c                d(24)

c                User parameters
c                d(25)          E
c                d(26)          xnu
c                d(27)          sigma0
c                d(28)          epsl0
c                d(29)          A
c                d(30)          B
c                d(31)          C
c                d(32)          dn
c                d(33)          dm
c                d(34)          epsldot0 : reference plastic strain
rate
c                d(35)          epsldotcutoff :cutoff plastic strain
rate
c                d(36)          Tm : Melting Temperature
c                d(37)          Tr : Room Temperature
c                d(38)          f : feed rate in m
c                d(39)          thc : thermal conductivity
c                d(40)          cp : heat capacity
```

```
c                 d(41)          UMATPAR17
c                 d(42)          UMATPAR18
c                 d(43)          UMATPAR19
c                 d(44)          UMATPAR20
c                 d(45)          UMATPAR21
c                 d(46)          UMATPAR22
c                 d(47)          UMATPAR23
c                 d(48)          UMATPAR24
c                 d(49)          UMATPAR25
c                 d(50)          UMATPAR26
c

c
c                 Reserved parameters
c
c                 d(83)          DENSITY
c                 d(84)          HEAT CAPACITY
c                 d(98)          Conductivity
c                 d(100)         Density (thermal)
c
c

c                  How to compile dll ?
c                  df /dll mat_user.f
c
c                 Radial Return method  elastic perfect-plastic
material
c
      real*8 sig(3,3),dtime,epsl(3,3),d(100),ql(15),deps(3,3)

      real*8 temperature
      real*8 sigtr(3,3),sigdiv(3,3),q(3,3)

        parameter ( zero = 0.d0, one = 1.d0, two = 2.d0, three = 3.d0,
     *       third = one / three, half = 0.5d0, twothds = two / three,
     *       op5 = 1.5d0 )



            e           = d(25)
            xnu         = d(26)
            sigma0  = d(27)
            epsl0   = d(28)
            A           = d(29)
            B           = d(30)
            C           = d(31)
            dn          = d(32)
            dm          = d(33)
            epsldot0= d(34)
            epsldotcutoff = d(35)
            Tm          = d(36)
            Tr          = d(37)
            f           = d(38)
            thc         = d(39)
            cp          = d(40)
        d2mu  = e / ( one + xnu )
        d3mu = 1.5 * d2mu
```

```
        dLambda = d2mu * xnu / ( one - two * xnu )


c     Initialize plastic work (heat generation)
        ql(3)= 0.0d0

        deltaLamTotal = 0.0d0

        if (ql(1) .le. 0.000001)then
            ql(1)= 0.000001
        endif

            if (ql(4) .lt. 1) then
           ql(4) = 1.0d0
          end if

        if (temperature.le. Tr) then
            temperature= Tr + 1.0d0
        endif




          epsldotstar = ql(4) / epsldot0




c       if ( dtime .eq. zero )      goto 150

c     Elastic stress increment
        tm1 = dLambda*(deps(1,1)+deps(2,2)+deps(3,3))
        sigtr(1,1) = sig(1,1) + d2mu*deps(1,1)+tm1
        sigtr(2,2) = sig(2,2) + d2mu*deps(2,2)+tm1
        sigtr(3,3) = sig(3,3) + d2mu*deps(3,3)+tm1
        sigtr(1,2) = sig(1,2) + d2mu*deps(1,2)
        sigtr(2,1) = sigtr(1,2)

50    continue

c     Calculate Deviatoric stress
        call umat_div_stress(sigtr,sigdiv)
c     Calculate deviatroic stress norm
        sigma_e = umat_sigdiv_norm(sigdiv)

c       If plastic strain rate is below cut off, set approximation
c       to cut off no strain rate hardening will occur


      Tstar = (temperature - Tr)/(Tm - Tr)

c
c      Yield stress
       sigmaJC= (A+B*ql(1)**dn)*(1-Tstar**dm)*(1+C*dlog(epsldotstar))


       dH= (dn*B*ql(1)**(dn-1))*(1-Tstar**dm)*(1+C*dlog(epsldotstar))
```

```
c       Strain increment (Radial return method)
        denom = d2mu*(1.0d0+dH/(d3mu))
        deltaLam =(sigma_e-dsqrt(2.0d0/3.0d0)*sigmaJC)/denom

c
c       i=i+1
c       write(6,*),"sigma i",i,dsqrt(1.5d0)*sigma_e
c
      if (deltaLam.le.0.0d0 .or. deltaLam.lt.1.0e-12) goto 100
c     Case of plasticity
        factor = 1.0d0/sigma_e
c
        q(1,1)= factor*sigdiv(1,1)
        q(2,2)= factor*sigdiv(2,2)
        q(3,3)= factor*sigdiv(3,3)
        q(1,2)= factor*sigdiv(1,2)
        q(2,1)= factor*sigdiv(1,2)
c
        deltaLamTotal = deltaLamTotal + deltaLam
c
c       write(6,*),i,sigma_e,yield,deltaLam,deltaLamTotal
c
c        Updated  stress
c
        sig(1,1) = sigtr(1,1)-deltaLam*d2mu*q(1,1)
        sig(2,2) = sigtr(2,2)-deltaLam*d2mu*q(2,2)
        sig(3,3) = sigtr(3,3)-deltaLam*d2mu*q(3,3)
        sig(1,2) = sigtr(1,2)-deltaLam*d2mu*q(1,2)
        sig(2,1) = sig(1,2)
c
        sigtr(1,1)=sig(1,1)
        sigtr(2,2)=sig(2,2)
        sigtr(3,3)=sig(3,3)
        sigtr(1,2)=sig(1,2)
        sigtr(2,1)=sig(1,2)
c
        goto 50
c
100   continue
c        Plastic strain
        ql(1)=ql(1) +dsqrt(2.0d0/3.0d0)*deltaLamTotal
c
c       Plastic strain rate
        ql(4)= deltaLamTotal/dtime
c
c
c       Plastic work rate (heat generation)
        ql(3)= deltaLamTotal * sigmaJC/dtime

c        Updated  stress
        sig(1,1) = sigtr(1,1)
        sig(2,2) = sigtr(2,2)
        sig(3,3) = sigtr(3,3)
        sig(1,2) = sigtr(1,2)
        sig(2,1) = sigtr(1,2)
```

```
c
c*********************************************************************
*
c     For RECHT formulation

        tau = sigma0 / dsqrt(3.0d0)

c     common terms


      constant = 1 / (2 * 4.1868 * dsqrt(3.1428*d(83)*thc*cp))


      DNUM = (dn*B /3)*(ql(1)**(dn-1))*(1- Tstar**dm)


      DENOM1 = (1/dsqrt(3.0d0)) * (A + B * (ql(1)**dn))
     *                  *(- dm/ (temperature - Tr)) * (Tstar**dm)

      DENOM2 = constant * tau * f * dsqrt (ql(4)/(ql(1)- epsl0))


      R = -DNUM / ( DENOM1 * DENOM2 )

      if(R .gt. 0.0d0 .and. R .lt. 1.0d0) then
           sig(1,1) = 0.d0
           sig(2,2) = 0.d0
           sig(3,3) = 0.d0
           sig(1,2) = 0.d0
           sig(2,1) = 0.d0
      end if
c*********************************************************************
*
c    150   continue

       END SUBROUTINE
c
      double precision function umat_sigdiv_norm(sigdiv)
c
c     Calculate diviatoric stress norm
c
      real*8 sigdiv(3,3)
      real*8 sigma_norm
c
       sigma_norm = sigdiv(1,1)*sigdiv(1,1)
     1             +sigdiv(2,2)*sigdiv(2,2)
     1             +sigdiv(3,3)*sigdiv(3,3)
     1       +2.0d0*sigdiv(1,2)*sigdiv(1,2)

      umat_sigdiv_norm = dsqrt(sigma_norm)
      return
      end
c
      SUBROUTINE umat_div_stress(sig,sigdiv)
c
c     Calculate Deviatoric stress
c
```

```
  real*8 sigdiv(3,3),sig(3,3),pressure
  pressure = (sig(1,1)+sig(2,2)+sig(3,3))/3.0d0
  sigdiv(1,1) = sig(1,1)-pressure
  sigdiv(2,2) = sig(2,2)-pressure
  sigdiv(3,3) = sig(3,3)-pressure
  sigdiv(1,2) = sig(1,2)
  sigdiv(2,1) = sig(2,1)

return
end
```

VITA

Kareem Syed

Candidate for the Degree of

Master of Science

Thesis: FINITE ELEMENT SIMULATION OF CHIP SEGMENTATION IN MACHINING A Ti 6Al-4V ALLOY

Major Field: Mechanical Engineering

Biographical:

Education: Received Bachelor of Engineering degree in Mechanical Engineering (with specialization in Production) from Osmania University, Hyderabad, India in June 2001. Completed the requirements for the Master of Science degree with a major in Mechanical and Aerospace Engineering at Oklahoma State University in December 2004.

Experience: Student intern in Design section, Pulverizer Engineering Department, Bharat Heavy Electricals Limited, Hyderabad, India, January, 2001-December, 2001.

Graduate Research Assistant in Mechanical and Aerospace Engineering Department, Oklahoma State University, Stillwater, Oklahoma, January, 2002 - present.

Professional Membership: ISME, ASME.

Name: Kareem Syed Date of Degree: December, 2004

Institution: Oklahoma State University Location: Stillwater, Oklahoma

Title of Study: FINITE ELEMENT SIMULATION OF CHIP SEGMENTATION IN MACHINING A Ti 6Al-4V ALLOY

Pages in Study: 145 Candidate for the Degree of Master of Science

Major Field: Mechanical Engineering

Scope and Methodology of Study: Ti 6Al-4V, a titanium alloy introduced in 1954, is considered the workhorse amongst the titanium alloys and is available in all product forms. It is extensively used in aerospace industry because of its excellent strength-to-weight ratio maintained at elevated temperatures, fracture resistance characteristics and exceptional corrosion resistance. The machinability of this alloy is generally considered to be poor owing to its several inherent properties. It is very reactive chemically and therefore has a tendency to weld to the cutting tool during machining. Its low thermal conductivity increases the temperature at the tool/workpiece interface, which affects the tool life adversely. Additionally, its high strength maintained at elevated temperature, low modulus of elasticity further impairs its machinability. In order to overcome the machinability issues associated with machining Ti 6Al-4V, an attempt has been made in this study to observe the effect of machining conditions on the chip formation, rake face and shear zone temperatures and cutting forces. To simulate orthogonal metal cutting of Ti 6Al-4V a commercial, general-purpose FE code (AdvantEdge™) has been used. AdvantEdge™ has the facility to incorporate user-defined material subroutine (UMAT). Using this, Johnson-Cook material model and Recht's catastrophic shear failure criterion are incorporated into the UMAT subroutine code.

Findings and Conclusions: Finite element simulations are conducted for a range of cutting speeds from 10 m/min to 100 m/min using two different depths of cut of 0.25 and 0.5 mm, for different rake angles from -15° to 45° using depth of cut of 0.5 mm and cutting speed of 30 m/min and for different values of coefficient of friction ranging from 0.3 to 0.9 using depth of cut of 0.5 mm and cutting speed of 30 m/min. Results of the simulations are compared with the experimental data and are found to be in close agreement. Mechanism of chip formation studied from simulations closely matched with that proposed in the literature. Effect of cutting speed, depth of cut, rake angles and coefficient of friction on cutting forces, temperature, strains and chip morphology is studied. Finally, cutting speed for the onset on chip segmentation is found for two different depths of cut.

Adviser's Approval: Dr.Ranga Komanduri